STRUCTURAL ANALYSIS AND DESIGN OF A LONG SPAN COMBINED CABLE-STAYED SUSPENSION BRIDGE CROSSING THE IZMIT BAY

by

Esra Zengin

B.S. in Civil Engineering, Middle East Technical University, 2008

Submitted to the Institute for Graduate Studies in

Science and Engineering in partial fulfillment of

the requirements for the degree of

Master of Science

Graduate Program in Civil Engineering

Boğaziçi University

2010

STRUCTURAL ANALYSIS AND DESIGN OF A LONG SPAN COMBINED CABLE-STAYED SUSPENSION BRIDGE CROSSING THE IZMIT BAY

APPROVED BY:

Assist. Prof. Dr. Kutay Orakçal (Thesis Co-Supervisor)	.....
Prof. Dr. Semih Tezcan (Thesis Co-Supervisor)	.....
Prof. Dr. Gülten Gülay	.....
Assoc. Prof. Dr. Cem Yalçın	.....
Assist. Prof. Dr. Bilge Doran	.....

DATE OF APPROVAL: 17/06/2010

To my family

ACKNOWLEDGEMENTS

I would like to express my appreciation and gratitude to my thesis Co-Supervisors, Prof. Dr. Semih Tezcan and Assist. Prof. Dr. Kutay Orakçal, for their encouragements, valuable advices and continuous support throughout the preparation of this Thesis.

My sincere gratitude is also due to the members of my advisory committee Prof. Dr. Gülten Gülay, Assoc. Prof. Dr. Cem Yalçın and Assist. Prof. Dr. Bilge Doran, for their useful suggestions and comments.

I would also like to thank my family, who have been very supportive for all my years of education. I am grateful for their endless support, encouragement and love they have given me throughout my life.

ABSTRACT

STRUCTURAL ANALYSIS AND DESIGN OF A LONG SPAN COMBINED CABLE-STAYED SUSPENSION BRIDGE CROSSING THE IZMIT BAY

In designing long span cable supported bridges, geometrical nonlinearity of the structure, including the cable sags, large deflections, and P-Delta effects, is a primary consideration. Also, reaching the initial equilibrium configuration of a cable supported bridge, via a set of geometrically-nonlinear analyses under dead loads, is essential in obtaining the stiffness properties of the cable elements for further analyses. In order to determine the static and dynamic behaviour of the cable supported bridges accurately, static and dynamic analyses should be conducted by considering all sources of geometric nonlinearity.

In this thesis, a particular analytical model has been developed for a proposed long-span combined cable-stayed suspension bridge crossing the Izmit Bay. To evaluate the behavior and response of the cable supported bridge, a series of static and dynamic analyses have been conducted under code-compliant service loads as well as using extreme load effects. Bridge displacements and internal forces in the structural members as a result of the applied forces and earthquake effects were calculated in accordance with the load combinations specified by AASHTO-LRFD (2007). Member capacities and deformations were checked per the ASSHTO-LRFD specifications and the structural performance of the proposed bridge was evaluated. The Bosphorus suspension Bridge in Istanbul was also modeled and analyzed within the scope of this work, as a preliminary case study to assess the validity of the modeling and analysis methodologies used.

ÖZET

İZMİT KÖRFEZİ'NDE GERGİLİ VE ASMA KABLOLU UZUN AÇIKLIKLI KÖPRÜ TASARIMI

Uzun açıklıklı köprülerin tasarımında kablo sehimlerinden ve büyük şekil değiştirmelerinden doğan geometrik doğrusalsızlık göz önünde bulundurulmalıdır. Ayrıca, kablolu köprülerin kendi ağırlığı altında doğrusal olmayan statik analizi, köprü sisteminin ilk denge konumunun belirlenebilmesi ile kabloların daha sonraki analizlerde kullanılacak rijitliklerinin elde edilebilmesi açısından önemlidir. Kablolu köprülerin statik ve dinamik davranışını belirleyebilmek için geometrik doğrusalsızlığı göz önüne alan statik ve dinamik analizler yürütülmelidir.

Bu tezde, İzmit Körfezi'ni geçmek için düşünülen gergili ve asma kablolu uzun açıklıklı bir köprünün analitik modeli geliştirilmiştir. Bu karma kablolu köprünün davranışını değerlendirebilmek amacı ile, AASHTO-LRFD (2007) Yönetmeliğinin belirttiği servis yükleri ve diğer aşırı yüklemeler altında statik ve dinamik analizler yapılmıştır. Aynı Yönetmelikte belirtilen yük kombinasyonları etki ettirilerek, köprünün yapısal elemanlarındaki sehimler ve iç kuvvetler hesaplanmıştır. Köprü elemanlarının kapasiteleri ve deformasyonları AASHTO-LRFD Yönetmeliğine göre kontrol edilerek köprünün yapısal davranış performansı değerlendirilmiştir. Bu tezin kapsamında, İstanbul Boğaziçi Köprüsü'nün modellenmesi ve analizleri bir ön çalışma olarak ele alınmış, böylece, İzmit Körfezi Köprüsü için uygulanan modelleme ve analiz yöntemlerinin doğruluğu değerlendirilmiştir.

TABLE OF CONTENTS

ACKNOWLEDGEMENTS iv
ABSTRACT v
ÖZET vi
TABLE OF CONTENTS vii
LIST OF FIGURES xi
LIST OF TABLES xvii
LIST OF SYMBOLS / ABBREVIATIONS xx
1. INTRODUCTION 1
1.1. General 1
1.2. Cable-Supported Bridges in the World 3
1.3. Objectives 8
1.4. Scope 9
1.5. Research Significance 9
1.6. Thesis Outline 10
2. LITERATURE REVIEW 11
2.1. Overview and Historical Background 11
2.1.1. Historical Development of Suspension Bridges 12
2.1.2. Historical Development of Cable-Stayed Bridges 14
2.2. Analytical Studies on Cable-Supported Bridges 16
2.3. Sources of Nonlinearity and Computation of Structural Stiffness 19
2.4. Geometrically Nonlinear Analysis 22
2.5. Material Nonlinearity 23
2.6. Modeling of Elastic Cable Elements 24
2.7. Tangent Stiffness of an Elastic Catenary Cable Element 25
2.8. Nonlinear Analysis Solution Strategy 28
3. STRUCTURAL COMPONENTS AND DETAILS 32
3.1. General 32
3.2. Force Transfer Mechanism in Cable-Supported Bridges 34
3.3. Combined Cable-Stayed Suspension (CSS) Hybrid Bridges 35
3.4. Structural Components of a Cable-Supported Bridge 37

3.4.1. Stiffening Girder 37
3.4.2. Towers 41
3.4.3. Cables 42
3.4.4. Anchorage Blocks 44
3.4.5. Cable Anchorages 45
4. STRUCTURAL ANALYSIS METHODOLOGIES 47
4.1. Static Analysis under Dead Load and Initial Equilibrium Condition 47
4.2. Static Analysis under Vehicular Loads 48
4.3. Moving Load Analysis 51
4.4. Analysis for Temperature Effects 52
4.5. Analysis of Bridge Deck under Aerostatic Wind Forces 52
4.6. Analysis of Bridge Piers under Equivalent Static Wind Loads 56
4.7. Analysis for Dynamic Earthquake Effects 60
4.7.1. Free Vibration (Modal) Analysis 60
4.7.2. Response Spectrum (Modal Superposition) Analysis 61
4.7.3. Time History Analysis 63
4.8. Design Load Combinations, Limit States, and Design Capacities of Structural Components 65
4.8.1. Design Load Combinations and Limit States 65
4.8.2. Design Capacities of Structural Components 68
4.8.2.1. Compressive Resistance 68
4.8.2.2. Combined Axial Compression and Flexure 69
4.8.2.3. Tensile Resistance 69
4.8.2.4. Combined Tension and Flexure 70
5. PRELIMINARY CASE STUDY: THE BOSPHORUS BRIDGE 72
5.1. Overview 72
5.2. Description of the Bridge 73
5.3. Design Loading Conditions 77
5.4. Structural Modeling 78
5.4.1. Material Properties 78
5.4.2. Main Structural Components 78
5.4.3. Connection Constraints and Releases 81
5.5. Structural Analysis Cases 82

5.5.1. Geometrically-Nonlinear Static Analysis under Dead Load 82
5.5.2. Moving Load Analysis..... 84
5.5.3. Analysis under Temperature Effects..... 86
5.5.4. Wind Load Analysis 87
5.5.5. Free Vibration (Modal) Analysis..... 92
5.5.6. Time–History Response Analysis of Earthquake Effects..... 98
5.5.7. Earthquake Response Spectrum Analysis..... 102
5.5.8. Comparison of Nonlinear Time History and Response Spectrum Analysis Result..... 104
5.5.9. Load Combinations..... 106
5.5.10. Comparison of Analysis Results with Design Documents 107
6. CASE STUDY: A COMBINED CABLE-STAYED SUSPENSION (CSS) HYBRID BRIDGE CROSSING THE IZMIT BAY..... 109
6.1. Overview..... 109
6.2. Description of the Izmit Bay Bridge Configuration 110
6.3. Structural Modeling 117
6.3.1. Material Properties..... 118
6.3.2. Main Structural Components 118
6.3.3. Connection Constraints and Releases 121
6.4. Structural Analysis Cases 122
6.4.1. Geometrically-Nonlinear Static Analysis under Dead Load 122
6.4.2. Moving Load Analysis..... 124
6.4.3. Analysis under Temperature Effects..... 125
6.4.4. Wind Load Analysis 126
6.4.5. Free Vibration (Modal) Analysis..... 131
6.4.6. Time–History Response Analysis of Earthquake Effects..... 137
6.4.7. Earthquake Response Spectrum Analysis..... 140
6.4.8. Comparison of Nonlinear Time History and Response Spectrum 141
6.5. Design Load Combinations and Limit States 143
6.6. Design Capacity Checks for Bridge Components 145
6.6.1. Cable Stayed Deck Segments under Combined Axial Compression and Flexure 147

6.6.2. Suspended Deck Segments under Combined Axial Compression and Flexure 149
6.6.3. Bridge Tower Legs under Combined Axial Compression and Flexure 150
6.6.4. Cable Stayed Deck Segments under Combined Axial Tension and Flexure 151
6.6.5. Suspended Deck Segments under Combined Axial Tension and Flexure 152
6.6.6. Suspension Cables under Axial Tension 153
6.6.7. Stay Cables under Axial Tension..... 153
6.7. Deflection Calculations for the Serviceability Limit State 154
7. SUMMARY AND CONCLUSIONS..... 155
7.1. Overview..... 155
7.2. Conclusions..... 155
APPENDIX A: AASHTO LRFD BRIDGE DESIGN SPECIFICATIONS..... 157
REFERENCES 164

LIST OF FIGURES

Figure 1.1. Span length versus year of completion of major suspension and cable-stayed bridges in the world, along with record breaking bridges designed for the near future 3

Figure 1.2. The Akashi-Kaikyo Bridge in Japan, center span 1991 meters 5

Figure 1.3. The Xihoumen Bridge in China, center span 1650 meters 6

Figure 1.5. The Sutong Bridge in China, center span of 1088 meters 6

Figure 1.6. The Stonecutters Bridge in China, center span of 1018 meters 7

Figure 1.7. The Tatara Bridge in Japan center span of 890 meters 7

Figure 1.8. Tower height versus year of completion of major suspension and cable-stayed bridges in the world 8

Figure 2.1. Configuration of a Suspension Bridge 11

Figure 2.2. Configuration of a Cable-Stayed Bridge 12

Figure 2.3. The difference between the behavior of cable structures and non-cable structures and accuracy results from different analysis procedures 21

Figure 2.4. Illustrations of geometrically nonlinear behavior 22

Figure 2.5. Tangent stiffness derivation for a catenary cable element 26

Figure 2.6. The Newton-Raphson solution strategy 29

Figure 3.1. Suspension system with vertical hangers 32

Figure 3.2. Suspension system with inclined hangers 32

Figure 3.3. Stay cable configurations for cable-stayed bridges 33

Figure 3.4. Cable force transfer mechanism for an externally-anchored suspension bridge 34

Figure 3.5. Cable force transfer mechanism for a self-anchored suspension bridge 34

Figure 3.6. Cable force transfer mechanism for a cable-stayed bridge 34

Figure 3.7. Combined cabled stayed suspension (CSS) bridge configuration 35

Figure 3.9. Conventional girder cross-sections 38

Figure 3.10. Aerodynamic (streamlined) closed-box deck cross-section 40

Figure 3.11. Bridge tower configurations 41

Figure 3.12. Wire strand types and cable construction 42

Figure 3.13. Wire stay cable and strand stay cable cross sections 44

Figure 3.14. Anchorage block 45

Figure 3.15. Tower–cable anchorage configurations 45

Figure 3.16. Freyssinet stay cable – deck anchorage 46

Figure 4.1. Characteristics of the design truck 49

Figure 4.2. HL-93 Loading in AASHTO-LRFD for truck and lane load 50

Figure 4.3. HL-93 Loading in AASHTO-LRFD for tandem and lane load 50

Figure 4.4. HL-93 Loading in AASHTO-LRFD for alternative load for negative bending moment between points of contraflexure and reaction at interior piers 50

Figure 4.5. Motion of bridge deck and three components of wind loads in different axes 55

Figure 4.6. Deck cross-sections of the Pont de Normandie and the Hoga Kusten Bridge and the Messina Straits Bridge (dimensions in meters)..... 56

Figure 4.7. Mean wind load and dynamic wind load profiles predicted by the code methods..... 60

Figure 4.8. Dependence of damping ratio on modal natural frequency for Rayleigh damping 65

Figure 5.1. General configuration of the Bosphorus Bridge..... 74

Figure 5.2. Streamlined cross section of the bridge deck..... 75

Figure 5.3. Bridge tower layout and bridge tower leg cross section at the base..... 76

Figure 5.4. Configuration of of uncompacted suspension cables 77

Figure 5.5. Three dimensional view of the structural model 79

Figure 5.6. Two- dimensional view in *xz* plane 79

Figure 5.7. Two- dimensional view in y*z* plane..... 80

Figure 5.8. Bending moment distributions in the bridge deck..... 84

Figure 5.9. Deflection measurements for the Bosphorus Bridge..... 86

Figure 5.10. Wind load profiles on the bridge tower legs in the longitudinal bridge direction 88

Figure 5.11. Wind load profiles on the bridge tower legs in the transverse bridge direction 89

Figure 5.12. Mode shape for the first mode of vibration (T=14.71 sec) 93

Figure 5.13. Mode shape for the second mode of vibration (T=9.28 sec) 94

Figure 5.14. Mode shape for the third mode of vibration (T=6.53 sec)..... 94

Figure 5.15. Mode shape for the fourth mode of vibration (T=6.37 sec)..... 95

Figure 5.16. Mode shape for the fifth mode of vibration (T=5.18 sec)..... 95

Figure 5.17. Mode shape for the sixth mode of vibration (T=4.74 sec) 95

Figure 5.18. Increase in cumulative mass participation factor with the number of modes 98

Figure 5.19. El Centro North-South ground acceleration time history recorded during the 1940 Imperial Valley earthquake 99

Figure 5.20. Variation of the damping ratio with natural cyclic frequency in the structural model 100

Figure 5.21. Nonlinear time-history analysis results: deck midspan displacement in longitudinal bridge direction..... 100

Figure 5.22. Nonlinear time-history analysis results: tower top displacement in longitudinal bridge direction..... 101

Figure 5.23. Nonlinear time history analysis results: deck midspan displacement in transverse bridge direction..... 101

Figure 5.24. Nonlinear time history analysis results: tower top displacement in transverse bridge direction..... 101

Figure 5.25. Pseudo acceleration response spectrum for the El Centro ground motion record (for 2% damping) and the AASHTO 2006 design spectrum 103

Figure 6.1. Hydrographic layout of the Izmit Bay Bridge location 111

Figure 6.2. Topographic layout of the Izmit Bay Bridge location 112

Figure 6.3. General configuration of the Izmit Bay Bridge 114

Figure 6.4. Streamlined cross section of the bridge deck..... 115

Figure 6.5. Cross section of the trapezoidal rib..... 115

Figure 6.6. General tower layout of the Izmit Bay Bridge..... 116

Figure 6.7. Cross section of the tower leg and tower cross beam 117

Figure 6.8. Three dimensional view of the structural model for the Izmit Bay Bridge 119

Figure 6.9. Two dimensional view of the structural model 119

Figure 6.10. Perspective view of the structural model..... 120

Figure 6.11. Bending moment distributions in the bridge deck..... 124

Figure 6.12. Wind load profiles on the bridge tower legs in the longitudinal bridge direction 127

Figure 6.13. Wind load profiles on the bridge tower legs in the transverse bridge direction 128

Figure 6.14. Mode shapes for the first mode of vibration (T=27.14 sec) 132

Figure 6.15. Mode shapes for the second mode of vibration (T=12.63 sec) 132

Figure 6.16. Mode shapes for the third mode of vibration (T=10.60 sec) 133

Figure 6.17. Mode shapes for the fourth mode of vibration (T=10.32sec) 133

Figure 6.18. Mode shapes for the fifth mode of vibration (T=10.31 sec)..... 134

Figure 6.19. Mode shapes for the sixth mode of vibration (T=9.97 sec) 134

Figure 6.20. Increase in cumulative mass participation factor with the number of vibration modes..... 136

Figure 6.21. Variation of the damping ratio with natural cyclic frequency in the structural model 138

Figure 6.22. Nonlinear time-history analysis results: deck midspan displacement in longitudinal bridge direction..... 139

Figure 6.23. Nonlinear time-history analysis results: tower top displacement in longitudinal bridge direction..... 139

Figure 6.24. Nonlinear time history analysis results: deck midspan displacement in transverse bridge direction..... 139

Figure 6.25. Nonlinear time history analysis results: tower top displacement in transverse bridge direction..... 140

LIST OF TABLES

Table 1.1. The Leading 10 Long-Span Suspension Bridges in the World 4

Table 1.2. The Leading 10 Long-Span Cable Stayed Bridges in the World 5

Table 3.1. Descriptions of stay cable configurations for cable-stayed bridges 33

Table 4.1. Multiple Presence Factors (m) in AASHTO-LRFD 51

Table 4.2. Wind effects on a cable-supported bridge structure 53

Table 4.3. C_y, C_z and C_m coefficients for the Messina Straits, Pont de Normandie, and Hoga Kusten Bridges, for 0° wind incidence 56

Table 4.4. Selected load combination limit states and load factors in AASHTO-LRFD 67

Table 4.5. Load factors for permanent loads (γ_p) in AASHTO-LRFD 67

Table 5.1. Material properties 78

Table 5.2. Cross sectional properties of the tower legs and tower cross beams 80

Table 5.3. Cross sectional properties of the deck 81

Table 5.4. Cross sectional areas of the cable elements 81

Table 5.5. Dead load analysis case results 84

Table 5.6. Moving live load analysis case results 85

Table 5.7. Comparison of calculated and measured live load deflections of the deck ... 86

Table 5.8. Temperature load analysis case results 87

Table 5.9. Aerostatic coefficients used for calculating wind loads on the deck 90

Table 5.10. Aerostatic wind loads acting on the deck 90

Table 5.11. Deck midspan displacements under wind loads on deck..... 90

Table 5.12. Deck quarter-span displacements under wind loads on deck 91

Table 5.13. Tower displacements under wind loads on towers 91

Table 5.14. Wind load analysis case results 91

Table 5.15. Calculated modal cyclic frequencies of the bridge 93

Table 5.16. Vibration modes with the highest 19 mass participation ratios 97

Table 5.17. Acceleration coefficients defined in AASHTO-LRFD 104

Table 5.18. Site coefficients defined in AASHTO-LRFD..... 104

Table 5.19. Comparison of nonlinear time history and response spectrum analysis results 104

Table 5.20. Load combinations used in the analysis of the Bosphorus Bridge 106

Table 5.21. Analysis results and reported values for the maximum tensile force on the suspension cables 107

Table 5.22. Analysis results and reported values for the internal forces at the base of the tower legs..... 108

Table 6.1. Material properties used in the structural model 118

Table 6.2. Cross sectional properties of the tower legs and tower cross beams 120

Table 6.3. Cross sectional properties of the deck 121

Table 6.4. Cross sectional properties of the cable elements 121

Table 6.5. Dead load analysis case results..... 124

Table 6.6. Moving live load analysis case results 125

Table 6.7. Temperature load analysis case results 126

Table 6.8. Aerostatic coefficients used for calculating wind loads on the deck 129

Table 6.9. Aerostatic wind loads acting on the deck 129

Table 6.10. Deck midspan displacements under wind loads on deck 129

Table 6.11. Deck quarter-span displacements under wind loads on deck 130

Table 6.12. Tower displacements under wind loads on towers 130

Table 6.13. Wind load analysis case results 130

Table 6.14. Calculated periods and cyclic frequencies of the bridge for the first 10 vibration modes 131

Table 6.15. Vibration modes with the highest 15 mass participation ratios 136

Table 6.16. Comparison of nonlinear time history and response spectrum analysis results 141

Table 6.17. Design load combinations used in the analysis of the Izmit Bay Bridge .. 143

Table 6.18. Envelope internal force resultant values at critical sections 144

Table 6.19. Maximum displacements and rotations at critical locations 154

LIST OF SYMBOLS / ABBREVIATIONS

A	Area enclosed within the centerlines of the plates comprising the box
A	Acceleration coefficient
A_g	Gross cross sectional area of the member
A_o	Cross-sectional area of the cable
A_s	Gross cross sectional area of structural components
b	Clear distance between plates
B	Deck width
C	Damping coefficient
$[C]$	Damping matrix
C_d	Drag coefficient
C_y	Aerostatic coefficients for calculating wind drag force in local bridge axes
C_M	Aerostatic coefficients for calculating pitch moment in local bridge axes
C_z	Aerostatic coefficients for calculating lift force in local bridge axes
d_z	Width of the tower cross section at height z
d_{max}	Maximum displacement
D	Vertical projected area of the deck
E	Modulus of elasticity
E_e	Effective modulus of elasticity of the sagging cable
E_c	Elastic modulus of the cable which is taut and loaded vertically
f	Cylic frequency
F	Nodal force
$[F]$	Flexibility matrix
$\{F_i\}$	External load vector for the i'th load step
$\{\delta F_i^j\}$	Unbalanced force vector for the i'th load step and j'th iteration cycle
F_y	Yield strength
$F_y(\alpha)$	Drag force at the effective wind angle of attack

$F_z(\alpha)$	Lift force at the effective wind angle of attack
g	Acceleration of gravity
G_o	Gust factor
h	Height of the tower
I_y	Moment of inertia about an axis perpendicular to the axis of bending
$[K]$	Tangent stiffness matrix
K	Geometric stiffness
K	Effective length factor
$[K^{s0}{}_1]$	Initial cable stiffness matrix for the first step of loading
$\left[K^s_{ini}\right]$	Initial cable stiffness matrix in the initial undeformed configuration
l	Horizontal projection of the cable length
l	Unbraced length
l_x	Deformed directional lengths of the cable in the x coordinate system
l_{x0}	Undeformed directional length in the x coordinate system
L_0	Unstretched length of the cable
m	Multiple Presence Factor
$[M]$	Mass matrix
$M(\alpha)$	Pitch moment at the effective wind angle of attack
M_n	Nominal flexural resistance for box shaped members
M_{mz}	Mean base moment at height z on the tower
M_o	Design moment at the base of the tower
M_{mo}	Mean moment at the base of the tower
M_{rx}	Factored flexural resistance about the x-axis
M_{ry}	Factored flexural resistance about the y-axis
M_{ux}	Factored flexural moment about the x-axis
M_{uy}	Factored flexural moment about the y-axis
M_W	Moment magnitude of the earthquake
M_z	Design moment acting at height z on the tower

p_z	Mean wind pressure
$\{p\}$	Dynamic load vector
P_n	Nominal compressive resistance
P_{ny}	Nominal tensile resistance for yielding in gross section
P_u	Axial compressive load acting on components
P_r	Factored resistance of components in compression/tension
$R_{\max}$	Peak response
R_i	Peak response of the *i*-th mode
r_s	Radius of gyration about the plane of buckling
r	Natural frequency ratio of the *i*-th mode to *j*-th mode
R_X	Rotations about the longitudinal bridge axis
S	Section modulus about the flexural axis
S	Site coefficient
t	Thickness of plates
T_1	Fundamental period of the tower in the direction of wind loading
T	Natural period
U	Displacement of deformation
$\{U\}$	Nodal displacement vector
$\left\{\delta U_i^j\right\}$	Incremental nodal displacements for the *i*'th load step & *j*'th iteration cycle
$\{u\}$	Relative displacement vector
$\{\dot{u}\}$	Relative velocity vector
$\{\ddot{u}\}$	Total acceleration vector
U_X	Mass participation ratio in the longitudinal direction
U_Y	Mass participation ratio in the transverse direction
U_Z	Mass participation ratio in the vertical direction
V	*M*ean wind velocity
V_R	Basic wind speed
v_z	Mean wind speed with height *z*
w, w_0	Unit weight of the cable

w_z	Design wind load at height z on the tower
w_{mz}	Mean wind load at height z on the tower
w_{dz}	Dynamic load at height z on the tower
α	Effective wind angle of attack
α_0	Angle of incidence
α	Mass matrix coefficient
β	Stiffness matrix coefficient
γ_p	Permanent load factor
Δ	Nodal displacement
ξ	Damping ratio
ϕ_c	Resistance factor for compression
ϕ_f	Resistance factor for flexure
ϕ_y	Resistance factor for yielding of tension members
θ	Torsional angle of twist of the deck
$\{\Phi_n\}$	Eigen vector at n^{th} mode
λ	Normalized column slenderness factor
ρ_a	Density of air
σ	Prevailing cable tensile stress
ω	Natural (angular) frequency
ω_n^2	Eigen value at n^{th} mode
ACI	American Concrete Institute
AR	Analysis Result
ASSHTO	American Association of State Highway and Transportation Officials
ASTM	American Society for Testing and Materials
BS	British Standards
CICIN	Comite International Des Chimnees Industrielle
CQC	Complete Quadratic Combination
CSS	Cable-Stayed Suspension

DC	Dead Load of Components and Attachments
DL	Dead Load
DIN	Deutsches Institut für Normung
EQ	Earthquake Load
EUDL	Equivalent Uniformly Distributed Loads
GUTS	Guaranteed Ultimate Tensile Stress
HDPE	High-Density Polyethylene
KE	Knife Edge Loads
LC	Load Combination
LL	Live Load
LRFD	Load and Resistance Factor Design
MDOF	Multi-Degree-Of-Freedom System
MPR	Modal Mass Participation Ratio
NBCC	National Research Council of Canada
NGA	Next Generation Attenuation
PEER	Pacific Earthquake Engineering Research Center
RV	Reported Value
SAP	Structural Analysis Program
SDOF	Single-Degree-Of-Freedom
SRSS	Square Root of the Sum of the Squares
Temp	Temperature Load
TU	Uniform Temperature Change
TG	Temperature Gradient
UV	Ultraviolet
WS	Wind Load on Structure

1. INTRODUCTION

1.1. General

Long span cable-supported bridges, that is, suspension bridges and cable-stayed bridges are elegant, economical and efficient structures, and are becoming increasingly popular worldwide for crossing ultra-long spans. In order to meet the economic, social, and technical needs of the community for efficient and convenient transportation systems, they have been built throughout the world since the 1980's. With rapid progress in analytical tools and construction technologies, cable-supported bridges with increasing span lenghts have been constructed in recent years.

Today, the longest suspension bridge – the Akashi-Kaikyo Bridge in Kobe, Japan – reaches a main (center) span length of almost 2000 meters, while its cable-stayed counterpart crosses a span of 1000 meters. The Sutong Bridge over the Yangtze River in China has the largest span for any cable-stayed bridge, with a main span of 1088 meters, although it is to be outranked in 2012 by the Russky Island Bridge in Vladivostok, Russia, with a 1104-meter main span. Such long-span cable-supported bridges play an important role in overcoming of barriers and bridging gaps that had previously split communities, nations and even continents. Cable-supported bridges offer the possibility to cross very large distances without the necessity for intermediate supports; therefore, it is only since their development, people have considered crossing, without intermediate supports, very large spans including the Bosphorus (two suspension bridges in Istanbul joining the European and Asian mainlands completed in 1973 and 1988), the Öresund River (cable-stayed bridge joining Denmark and Sweden completed in 2000), the Strait of Messina (proposed suspension bridge joining the mainland Italy and Sicily), the Strait of Gibraltar (proposed suspension bridge between Spain and Morocco), and the Berring Strait (proposed suspension bridge between Alaska and Russia).

Although a cable-supported bridge is subjected to high stresses under predominant gravity load effects, its response is also sensitive to dynamic loadings

resulting from earthquake and wind effects, as well as the influence of moving vehicles and temperature changes. Under such conditions, the performance of a large-span cable-supported bridge must be assessed to ensure smooth operation and safety during its life span. One way to assess the existing dynamic attributes of a bridge is to monitor changes in its vibration characteristics including natural frequencies, damping ratios and mode shapes. Those changes, if properly identified and classified (e.g., Roebling *et al*., 1996; Ren *et al*., 2005; Wang *et al*., 2007), can provide a viable means for damage detection on the bridge structural system. With ever increasing span lengths, the dynamic behavior of cable-stayed bridges and suspension bridges is further complicated, and fundamental characteristics including stiffness of the structural members, variation of cable forces, and stability of the structural system, play a more critical role in the safety and serviceability evaluation of such bridges.

To evaluate the static and dynamic responses of long-span bridges, the critical structural modeling aspects include:

(i) Three-dimensional modeling of the bridge structural system using a suitable computational structural analysis platform, which considers coupling of different modes of deformation. For example, in the case of cable-supported (suspension or cable-stayed) bridges, torsional vibration of the deck is typically coupled with its lateral vibration. A sufficiently detailed analytical model that considers such coupling is required for a reliable response prediction.

(ii) For flexible long-span bridges such as suspension and cable-stayed bridges, due to the flexibility characteristics of the cables when loaded in transverse direction, it is crucial to consider geometric nonlinearity effects resulting from large displacements and rotations. Since the superimposed loads (live loads as well as wind, earthquake, and temperature effects) are applied to the dead- load-deformed configuration, a nonlinear static (incremental) analysis is required to establish the bridge (cable) geometry under dead loads in order to obtain realistic stiffness characteristics for the structural system for analysis under superimposed loads.

1.2. Cable-Supported Bridges in the World

For cable-supported bridges, the term "span" typically indicates the main (center) span length of the bridge; that is, the distance between the center lines of the bridge towers (or pylons or piers). It must be emphasized that the span does not refer to the total or overall length, which would be defined as the sum of the span lengths for a multi-span bridge. As shown in Figure 1.1, there are some 30 bridges in the world with a span longer than 1000 meters, and almost half of these bridges are located in China. All of these bridges are cable-supported (suspension or cable-stayed) bridges. The record span for suspension bridges is close to the 2 km limit, whereas the limit is 1 km for cable-stayed bridges.

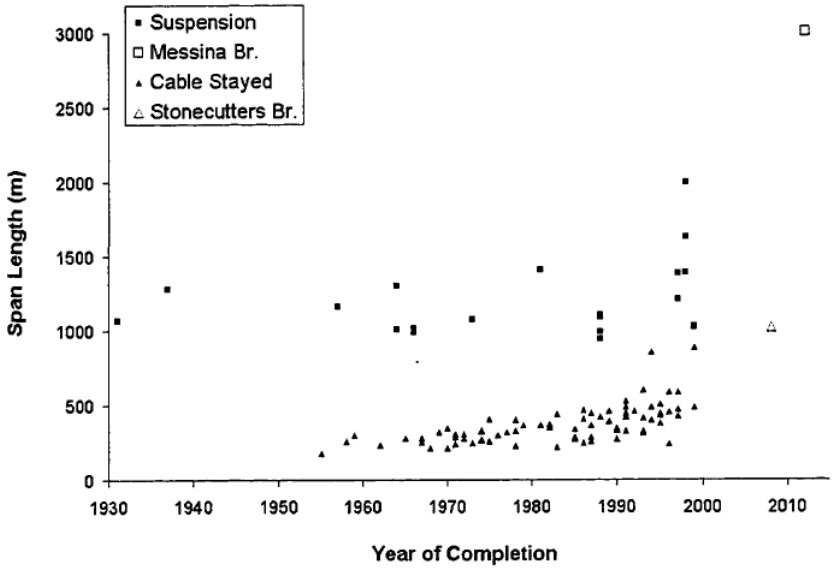

Figure 1.1. Span length versus year of completion of major suspension and cable-stayed bridges in the world, along with record breaking bridges designed for the near future (Karoumi, 1999)

Table 1.1 lists the leading 10 long-span suspension bridges in the world, whereas the leading 10 cable-stayed bridges are presented in Table 1.2. Among suspension bridges, the one with the longest span is the mighty Akashi-Kaikyo Bridge, with a main span of 1991 meters. Located near Kobe in Japan, along the Kobe-Naruto Route, between Honshu and Shikoku Islands, the bridge was completed in 1998 and shown in Figure 1.2 (Virola, 2002).

The second longest-span suspension bridge is the Xihoumen Bridge in China, south of Shanghai (Figure 1.3), and the third is the Great Belt East Bridge in Denmark, 100 km west of Copenhagen (Figure 1.4). Among cable-stayed bridges, the one with the longest span is the Sutong Bridge near Shanghai in China (Figure 1.5), and the second-longest is the Stonecutters Bridge in Hong Kong, also in China (Figure 1.6). These two are currently the world's only two cable-stayed bridges having a main span longer than 1 km. The previous world record belonged during the years 1999 to 2008 to the Tatara Bridge in Japan (Figure 1.7).

Table 1.1. The Leading 10 Long-Span Suspension Bridges in the World

Rank	Name	Location	Main Span (meters)	Completed
1	Akashi Kaikyō Bridge (the longest from 1998 to the present)	Kobe-Awaji Route, Japan	1,991	1998
2	Xihoumen Bridge	Zhoushan Archipelago, China	1,650	2009
3	Great Belt Bridge	Halskov-Sprogø, Denmark	1,624	1998
4	Runyang Bridge	Yangtze River, China	1,490	2005
5	Humber Bridge (the longest from 1981 until 1998)	Barton-upon-Humber - Kingston upon Hull, England, UK	1,410	1981
6	Jiangyin Suspension Bridge	Yangtze River, China	1,385	1999
7	Tsing Ma Bridge (the longest carrying road and rail traffic)	Tsing Yi-Ma Wan, Hong Kong	1,377	1997
8	Verrazano-Narrows Bridge (the longest from 1964 until 1981)	New York City (Brooklyn–Staten Island), USA	1,298	1964
9	Golden Gate Bridge (The longest from 1937 until 1964)	San Francisco-Marin County, CA, USA	1,280	1937
10	Yangluo Bridge	Yangtze River, China	1,280	2007

Table 1.2. The Leading 10 Long-Span Cable Stayed Bridges in the World

Rank	Name	Location	Main Span (meters)	Completed
1	Sutong Bridge	Suzhou, Nantong, China	1,088 m	2008
2	Stonecutters Bridge	Rambler Channel, Hong Kong	1,018 m	2009
3	Tatara Bridge	Seto Inland Sea, Japan	890 m	1999
4	Pont de Normandie	Le Havre, France	856 m	1995
5	Incheon Bridge	Incheon, South Korea	800 m	2009
6	Shanghai Yangtze River Bridge	Shanghai, China	730 m	2009
7	Third Nanjing Yangtze Bridge	Nanjing, China	648 m	2005
8	Second Nanjing Yangtze Bridge	Nanjing, Jiangsu, China	628 m	2001
9	Jintang Bridge	Zhoushan Archipelago, China	620 m	2009
10	Baishazhou Bridge	Wuhan, China	618 m	2000



Figure 1.2. The Akashi-Kaikyo Bridge in Japan, center span 1991 meters (Virola, 2009)



Figure 1.3. The Xihoumen Bridge in China, center span 1650 meters (Virola, 2009)



Figure 1.4. The Great Belt East Bridge in Denmark, center span 1624 meters (Virola, 2009)



Figure 1.5. The Sutong Bridge in China, center span of 1088 meters (Virola, 2009)



Figure 1.6. The Stonecutters Bridge in China, center span of 1018 meters (Virola, 2009)



Figure 1.7. The Tatara Bridge in Japan center span of 890 meters (Virola, 2009)

For conceptual design of suspension bridges, the height of the bridge towers above the deck depend on the sag-to-span ratio which can vary from about 1:8 to 1:12. To this value must be added the structural depth of the deck and the clearance to the foundations to obtain the approximate total tower height. For cable stayed bridges, number of cables and cable arrangements are affected the type and height of the tower. The cable forces and the required quantity of cable steel decrease with the height of the tower above the road level. The height of the tower also defines the angle of inclination of the longest cables. This angle should not be smaller than about 25 degrees because otherwise the deflections will

become too large (Leonhardt, 1987). It is seen from Figure 1.8., that the tower heights for both the cable stayed and suspension bridges, have increased considerably over the years from 1930 to 2010, as the technological progress in steel manufacturing likewise increased significantly. It can be said that tower height to main span ratio range for suspension bridges changes from 0.10 to 0.20 and for cable stayed bridges, the range changes from 0.20 to 0.40.

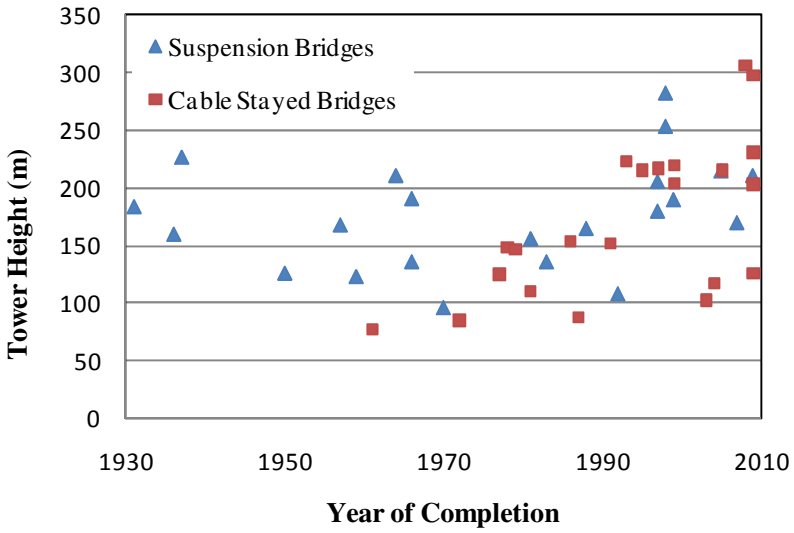

Figure 1.8. Tower height versus year of completion of major suspension and cable-stayed bridges in the world

1.3. Objectives

The main objectives of this study are as follows:

(i) Development of a three-dimensional analytical model for a proposed long-span combined cable-stayed suspension (CSS) hybrid bridge with a main span of 2400 meters,

(ii) Implementation of appropriate static and dynamic analyses for evaluating the behavior and response of the proposed bridge under code-compliant service loads as well as extreme load effects,

(iii) Determination of internal force demands in critical members including the bridge deck, towers, and cables. Comparison with code-compliant member design capacities for evaluation of appropriate strength limit state conditions,

(iv) Assessment of displacements under static and dynamic loading effects, for the evaluation of serviceability conditions.

1.4. Scope

In order to reach the objectives listed above, the analytical studies were conducted for a proposed long-span combined cable-stayed suspension (CSS) hybrid bridge crossing the Izmit Bay. For this purpose, a three-dimensional structural model of the proposed bridge (as well as for the Bosphorus Bridge as a preliminary case study) was created using the general purpose commercial structural analysis software SAP2000.

Sources of geometric nonlinearity, including the cable sags, large deflections, and P-Delta effects, were incorporated in the structural model of the bridge. The model was calibrated geometrically to maintain its proposed configuration when subjected to dead loads. Modal analyses were performed to determine the vibration characteristics of the bridge model.

Code-compliant live loads, wind loads, and temperature changes were then imposed on the model. For earthquake response assessment, the response spectrum analysis and time-history analysis methods were both used. Bridge displacements and internal forces in the structural members as a result of the applied forces and earthquake effects were calculated in accordance with the load combinations specified by AASHTO-LRFD (2007). Member capacities and deformations were checked per the ASSHTO-LRFD specifications and the structural performance of the proposed bridge was evaluated.

1.5. Research Significance

In this thesis, a three-dimensional structural model was developed for the analysis and design of a possible combined cable-stayed suspension (CSS) hybrid bridge

configuration spanning across the Izmit Bay. To evaluate the behavior and response of the cable supported bridge, the static and dynamic analyses have been conducted under code-compliant service loads as well as using extreme load effects. The research significance of this study in particular is that the Bosphorus Bridge in Istanbul was also modeled and analyzed as a preliminary case study to assess the validity of the modeling and analysis methodologies used. It shows that the analysis results obtained using the model created for the Bosphorus Bridge are consistent with previous experimental and analytical studies conducted on the bridge, as well as the analysis results reported in the design documents; validating the structural modeling approach, loading types, and the analysis methods used in this study.

1.6. Thesis Outline

The scope and findings of the analytical studies are summarized in this thesis. In the first Chapter, an introduction, as well as the objectives and scope of this study were provided. Chapter 2 presents a literature review including the historical development of the cable-supported bridges and description of the theory for cable-stayed and suspension bridge analysis including geometric and material nonlinearity aspects. Chapter 3 presents information on structural components and details of cable-supported bridges. Chapter 4 describes details of the load calculations, as well as the static and dynamic analysis methodologies that were used for the cable-supported bridges analyzed. Modeling and analysis of the Bosphorus Bridge in Istanbul is presented in Chapter 5 as a preliminary case study. The natural frequencies of the Bosphorus bridge and the mode shapes are also compared in this chapter with previous modal analysis studies and field measurements. Chapter 6 includes structural modeling and analysis of the proposed combined cable-stayed suspension (CSS) hybrid bridge crossing the Izmit Bay. Analysis results for the proposed bridge are evaluated and internal forces in structural members are compared with AASHTO-LRFD member capacities for assessment of the bridge performance considering both strength and serviceability limit states. Chapter 7 presents a summary of findings and recommendations for further research in this area.

2. LITERATURE REVIEW

2.1. Overview and Historical Background

In this section, a brief historical review is presented on the development of analysis, design and construction techniques for the cable-supported bridges worldwide.

Modern cable-supported bridges, in which the bridge deck superstructure is supported by cable elements, can be classified into two types as suspension bridges and cable-stayed bridges. Suspension bridges differ from cable-stayed bridges in terms of the cable force transfer mechanism and presence of cable end anchorages. In suspension bridges, the cables carry the deck via hangers (or suspenders), which connect the deck superstructure to main catenary cables The main cables transfer the vertical loads from the hangers to bridge towers and end anchorages, in the form of tensile forces acting along their profile. On the other hand, in cable-stayed bridges, the deck is supported by inclined stay cables connected directly to the bridge towers on both sides. Horizontal components of the tension forces in the stay cables are transferred to the deck superstructure as compression forces, and are mostly balanced on each side of the tower, not requiring the use of external end anchorages. Figures 2.1 and 2.2 show the schematic sketches of typical suspension and cable-stayed bridge configurations, illustrating their main components.

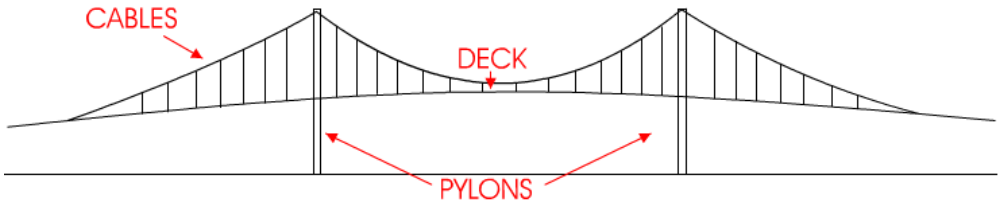

Figure 2.1. Configuration of a Suspension Bridge

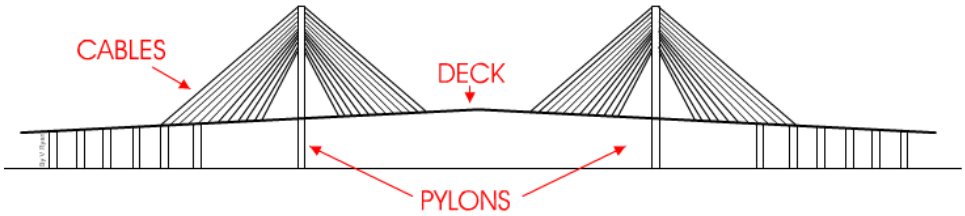

Figure 2.2. Configuration of a Cable-Stayed Bridge

2.1.1. Historical Development of Suspension Bridges

Until the 19th century, the theory on suspension bridge analysis and design was primitive. Basic issues related to the real behavior of bridge components, including second-order moments or geometric nonlinearity effects in cable stiffness, were not properly appreciated. Due to limitations on the existing theory, the Clifton Bridge (constructed in 1864) for example, oscillated severely under wind load and required substantial structural retrofit for stabilization.

During the 19th century, French engineers worked on developing new technologies for the construction of suspension bridges. Using of wire rope to fabricate cables instead of links and chains was the most significant development. A new methodolgy to spin wire cables on-site was used by Vicat (Al-Asaf, 2006). The cables of the Fribourg Bridge were constructed using this method and the bridge remained as the longest suspension bridge in Europe until the year 1900.

The Americans began building their first long-span bridges using French methodologies. Charles Ellet (1810-1862) considered the geometric stiffness effects, due to gravitational loading, in cable-supported bridge analysis. He designed the Wheeling Bridge with main span of 308 meters, which later failed under wind effects due to its low torsional stiffness. The bridge was later rebuilt by John Roebling (1806-1869). Roebling paid attention to the need of torsional stiffness in the deck truss, although the concept of torsional stiffness was not clearly comprehended, until Rankine's theory was developed, which emphasized the importance of torsional stiffness in the design of a suspension bridge superstructure (deck). Roebling designed his bridges based on his intuitive

engineering sense, before Rankine's theory, and his last accomplishment was the Brooklyn Bridge constructed in 1883, with a main span of 425 meters.

Other fundamental theories were later developed and adopted in the design of suspension bridges. Leon Moisseiff adopted the large deflection theory in designing the Manhattan Bridge in 1909 (Al-Asaf, 2006). The use of the large deflection theory allowed him to design relatively long-span bridges. Moisseiff claimed that cables stretched under the gravity loads provide the adequate stiffness for long span bridges having a relatively slender superstructure. He implemented his thought in designing the first Tacoma Narrows Bridge with a main span of 853 meters. His judgment was right regarding to the vertical stiffness of the bridge; however, it ignored the necessity for torsional stiffness of the superstructure. Moreover, the H-shape used for the cross-section of the superstructure (deck) of the bridge was quite unsuitable from an aerodynamic perspective, an issue which was not understood at that time. The bridge collapsed due to flutter under wind effects in November 1940.

Although the first Tacoma-Narrows was not the first suspension bridge to fail under wind effects, its collapse invoked the need of understanding dynamic wind effects on long-span bridges. The collapse of the first Tacoma Narrows Bridge initiated evolution of aerodynamics research in the area and emerging of aeronautical engineering science as well as wind tunnel testing, both of which were newly-applied technologies in designing aircrafts during the Second World War. These technologies were adopted for bridge engineering and were used after the 1950's as a standard requirement for designing long-span bridges.

After the 1970's the theory of suspension bridges and bridge aeroelasticity became more established. Construction techniques of casting caissons and steel fabrication of cables and tower elements improved significantly. For example, improvement of the yield capacity of structural steel made the Akashi-Kaikyo Bridge, built in Japan with a 1999 meter main span, possible. The steel used for construction of the bridge cables had higher tensile yield strength (1860 MPa) compared to that of the conventional steel for bridge cables.

2.1.2. Historical Development of Cable-Stayed Bridges

In Europe, the interest in bridges with stays was initiated in 1617, when Faustus Verantius, a Croatian engineer, proposed a bridge supported by several chain stays but it was not until the late 18th Century that such bridges were actually built (Bessas, 2006). Further development took place in 1817, with the English engineers, Redpath and Brown, who designed the Kings Meadow footbridge with a span of 33.6m. In 1821, French architects suggested a very steep fan-type (radial) steel bar-stayed bridge for a prestigious French project, and these bridges were the first signs of a cable-stayed revolution.

This revolution in cable-stayed bridges would have continued but for the collapse of two bridges in 1818 and in 1824. The first one, the 79m pedestrian Tweed River bridge near Dryburgh-Abbey, England, collapsed six months after completion due to fatigue failure of the chain stays subjected to severe wind oscillations (Troitsky, 1988), The second, 78m Saale River bridge in Nienburg, Germany, collapsed in 1824. This collapse was reported to have been caused by an unusual crowd loading during a festival. The lack of technical knowledge in the theoretical analysis of the internal forces in the stays, the inappropriate materials and the inability of the engineers to understand the behavior of this type of bridges, lead the structures to fail miserably.

High stiffness materials, unavailable in those early constructions, were later introduced and, finally, made it feasible to construct a safe cable-stayed system. 20th century was time for the technological evolution and the advancement of analytical theories for statically indeterminate structures to overcome the problems associated with cable-stayed bridges and to make this type of bridges a viable alternative for bridge design. At the early part of the twentieth century, French engineers proposed a new system consisting of inclined and horizontal cables. The system represented a three-hinged arch, having the diagonals made of cable trusses. In 1925, French engineers further developed the Gisclard system and proposed the Lezardrieux Bridge, which has stays from both towers overlapping. This system proved to be very economical and also gave only small deflections (Troitsky, 1988). This bridge became the prototype of the contemporary cable-stayed bridges, which have a fan (radial) system of cables.

The plane steel-deck cellular cross-section, promoted by Leonhardt in 1936, was also a major factor which made the re-introduction of cable-stayed bridge possible. These steel plates acted as an upper chord of the transverse girders and also of the longitudinal main girders. With these plates, the entire deck would act as one continuous unit, including the towers supports. The continuous deck became a requirement for cable-stayed bridge (Leonhardt, 1991).

In 1938, German engineers discovered that the incorporation of stay-cables significantly reduce the bridge deflection under railroad loading. They also pointed out that cables made of high-stiffness steel wire must be prestressed in order to minimize the softening effect of the sag in long cables. These findings marked a significant step toward the modern era for cable-stayed bridges. After the Second World War, 15,000 bridges in Germany had been destroyed. The need to rebuild these crossings provided the opportunity for engineers and builders to apply new concepts of design and construction. The cable-stayed bridge system was the most economical type of structure available, because of its lighter weight and the quick construction. Therefore, cable-stayed bridges became the favorite type of structure chosen for crossing spans, especially in Germany. In 1952, Leonhardt designed the world's first modern cable-stayed bridge across the Rhine River in Dusseldorf, but this bridge was not constructed until 1958. In 1955, the German firm Demag, in collaboration with Dischinger, ultimately erected the first contemporary cable-stayed bridge in the world, the Stromsund Bridge, which has a main span of 183m. At present, cable-stayed bridges can be found in every country in Europe.

In Japan, the engineers began to take cable-stayed bridges seriously in 1960s (Amornvivat, 1996). The first Japanese attempt at modern cable-stayed bridge was the Kutsuse Bridge, which has a single span of 128m. The Kutsuse Bridge, completed in 1960, was the first contemporary cable-stayed bridge constructed outside of the sphere of the pioneering German technology. The number of cable-stayed bridge constructions in Japan has increased tremendously since the 1970s. As of 1991, Japan has one third of the total number of the world cable-stayed bridges (Ito, 1991).

In North America, the first contemporary vehicular cable-stayed bridge constructued was the Sitka Harbor Bridge, completed in 1972 in Alaska. The number of cable-stayed

bridge constructions in North America has increased greatly in the past three decades (Tang, 1991).

2.2. Analytical Studies on Cable-Supported Bridges

Nonlinear behavior and analysis of cable-stayed bridges, due to geometric nonlinearity effects, have extensively been studied since the 1970s. In 1971, Tang (1971) adopted a reduction method to carry out the linear and nonlinear analysis of cable stayed bridges. In his methodology, the nonlinear analysis was carried out iteratively by treating the nonlinear terms as imaginary external loads.

Lazar (1972) adopted the stiffness method for nonlinear analysis of cable-stayed bridges. In this method, nonlinearity due to large displacements, axial force – bending moment interactions (P-Delta effects), and geometric nonlinearity of cable stiffness were all taken into account. Baron and Lien (1973) proposed a nonlinear theory, in which the finite element method was used to determine the static load effects on a bridge, in 1973. Nonlinear force–deformation relationships for the cable elements and nonlinearity in the tangent stiffness of the structure were employed in the analytical model. In 1979, Fleming (1979) conducted nonlinear static analysis of a plane cable-stayed bridge model by using a combined incremental and iterative approach. The nonlinearity in cable force–deformation behavior and stiffness was considered by using an equivalent modulus of elasticity for the cables. The nonlinearities in the behavior of deck or tower members were considered by introducing the concept of stability functions.

The elasto–plastic and finite displacement behavior of cable-stayed bridges were investigated by Nakai *et al*. (1985) in 1985. In this analysis, a cable-stayed bridge was modeled as a three-dimensional frame structure with cable elements, for which elasto–plastic and finite displacement behaviors were formulated using a finite element method on the basis of the updated Lagrangian configuration. An improved finite strip method using two types of longitudinal shape functions for the nonlinear analysis of long-span cable-stayed bridges was proposed in the early 1990s. The angle change of the cables and the sag effect were taken into account by means of the catenary theory. The modified Newton-Raphson iteration method was used as the nonlinear analysis solution strategy.

The dynamic behavior of three-dimensional (3-D) long-span cable-stayed bridges under seismic loadings was studied by Abdel-Ghaffar *et al.* (1991). Numerical examples were presented in which comparisons were made between the results of a linear earthquake response analysis (based on the utilization of the tangent stiffness matrix of the bridge at the dead-load deformed state) and results of nonlinear earthquake response analysis using the step-by-step integration procedure. The results showed that the nonlinear analysis is essential not only for evaluating the stress and deformation induced by wind and earthquakes, but also for ensuring safety during construction. For the the range of center spans up to 450m, however, Fleming and Egeseli (1980) had previously stated that linear dynamic analysis is adequate as long as nonlinear static analysis under dead load is still essential to start the linear dynamic analysis from the dead-load deformed state.

The elasto-plastic seismic behavior of long span cable-stayed steel bridges using a planar finite element model formulation was investigated by Ren and Obata (1999). Geometric nonlinearities and the material nonlinearity were both considered in this analysis. To evaluate the residual elasto-plastic seismic response, a new kind of seismic damage index called the maximum equivalent plastic strain ratio was proposed. The results showed that the elasto-plastic effect tends to reduce the seismic response of long span cable-stayed steel bridges. The elastic and elasto-plastic seismic response behavior attributes were found to depend highly on the characteristics of input earthquake records, where the earthquake record with the largest peak ground acceleration value did not necessarily induce the largest plastic deformation and seismic damage.

Shu and Yang (2001) investigated the stability characteristics of box-girder cable-stayed bridges using three-dimensional finite-element analysis. A typical two-lane, three-span, steel box-girder cable-stayed bridge superstructure was selected for this study. The numerical results indicated that if the ratio of the main span length with respect to the total span length, was small, the deck superstructure usually had a higher critical buckling load. The critical load was found to decrease when the ratio of the moment of inertia of the pylon to the moment of inertia of the bridge deck was increased. Considering cable configurations, bridges with harp-type cable arrangement were found to be a better design alternative compared to bridges with fan-type cable arrangements, based on buckling

analysis. The numerical results also indicated that use of either A-type or H-type pylons did not significantly affect the critical buckling load.

Xu *et al.* (1997) established a three-dimensional dynamic finite element model for the tower-cable system of the Tsing Ma suspension bridge in China. The bridge towers, made up of reinforced concrete columns and deep prestressed concrete beams, were modeled by three-dimensional Timoshenko beam elements with rigid arms at the connections between columns and beams. The main span and side span cables were modeled by three-node cable elements accounting for geometric nonlinearity and large elastic deflection. Modal analyses were then performed to determine the dynamic characteristics and dynamic interaction between the towers and cables. The results show that at lower natural frequencies, the modes of vibration of the system may be reasonably separated into in-plane modes and out-of-plane modes. Dynamic interactions between the towers and cables were found to be significant at global natural frequencies in either in-plane or out-of-plane vibration. The finite element model and the analytical results were verified via in-situ measurements on the dynamic properties of the system.

Zhang and Sun (2004b) conducted parametric analyses on the aerodynamic stability of the Runyang Suspension Bridge over the Yangtze River in China, using the method of three-dimensional nonlinear aerodynamic stability analysis. In this study, the influence of important design parameters, including the structural system, the cable sag, the side span length, the depth, dead load and the supporting system of the deck, on the aerodynamic stability of the bridge was investigated. Analysis results indicated that as far as the aerodynamic stability is concerned, three-span systems and the continuous deck systems were favorable configurations for the bridge. Short side spans were also found to be advantageous in terms of aerodynamic stability. The cable sag and the deck depth were both found to have important influence on the aerodynamic stability, and it was stated the aerodynamic stability could be greatly improved by increasing the cable sag and the deck depth.

A suspension bridge model with pre-tensioned reverse profiled cables was studied by Huang *et al.* (2005), to investigate free vibration characteristics of shallow suspension bridges. Effects of structural parameters including cable sag, cross sectional area, mass,

and pre-tensions in the profile cables were investigated. The results showed that for cable supported bridges with shallow sag, the lowest frequencies correspond to lateral and torsional vibration modes, which are always combined together and become two types of coupled modes: coupled lateral–torsional modes, and coupled torsional–lateral modes. It was found that the natural frequencies can be altered by introducing different pre-tensions in the reverse profiled cables.

A three-dimensional finite element model for the the first triple-tower long-span suspension bridge, the Taizhou Yangtze River Bridge in China, was established using the nonlinear finite element software ABAQUS, by Wang *et al*. (2010). The study focused on the effects of the vertical, lateral and torsional stiffness of the steel box girder comprising the deck superstructure, and results showed that the vertical, lateral and torsional stiffnesses of the steel box girder have different effects on the dynamic characteristics of triple-tower suspension bridges.

A three-dimensional nonlinear aerodynamic stability analysis of a combined cable-stayed-suspension (CSS) hybrid bridge, with main span of 1400 meters was studied by Zhang *et al.* (2005). The effects of important design parameters (including the cable sag, the length of the suspension portion, cable plane arrangement, subsidiary piers in side spans) on the aerodynamic stability of the bridge were analytically investigated. It was confirmed that CSS hybrid bridges exhibit better performance compared to suspension bridges with similar span lengths. Increasing the cable sag was found to be helpful for improving the aerodynamic stability of a CSS hybrid bridge, and existence of subsidiary piers in the side spans were found to be aerodynamically favorable.

2.3. Sources of Nonlinearity and Computation of Structural Stiffness

Nonlinearities in the behavior of cable-stayed and suspension bridges can be broadly divided into geometrical and material nonlinearities. Under service loads, geometrical nonlinearity becomes an important feature of cable-supported bridge behavior. Foremost, the structural model of the bridge needs to be analyzed under dead loads considering geometric nonlinearity, in order to obtain its deflected shape under dead loads. Geometric nonlinearity is associated with:

- The cable sag which governs the axial elongation and the axial tension in the cable,
- The effect of relatively large deflections of the whole structure due to its flexibility (large deformations),
- The action of compressive loads in the deck and in the towers (P-Delta effects).

It is well known that a cable, supported at both ends and subjected to its self weight and an externally applied axial tension force (e.g., due to a prestressing force or a temperature change), will sag into the shape of a catenary. Increasing the axial tension force not only results in an increase in the axial strain of the cable but also in a reduction of the sag which evidently leads to a nonlinear stress – displacement relationship. The influence of the cable sag on its axial stiffness has first been analytically expressed by Ernst (1965). If an inclined cable under its self weight is considered, an equivalent elastic modulus can be calculated as follows:

$$E_e = \frac{E}{1 + \frac{(wl)^2 E}{12\sigma^3}} \tag{2.1}$$

where: E_e : effective modulus of elasticity of the sagging cable
E_c : elastic modulus of the cable which is taut and loaded vertically
w : unit weight of the cable
l : horizontal projection of the cable length
σ : prevailing cable tensile stress

This relationship can be easily implemented in nonlinear computer codes. Ren (1999) included the effects of large displacements while modeling the cable sag effect using Ernst's tangent modulus. The seismic results were compared to a linear analysis and the differences were very small. The conclusion was that consideration of large displacements was not required and linear analysis remained appropriate, as long as an equivalent elastic modulus is used in the analysis for the cable elements. In addition, Ren (1999) observed that Fleming (1979) and Nazmy (1990) also reached the same conclusion

for cable-stayed bridges. This is the case while the cables are in a high state of tension and while there is no significant variation in the state of tension.

It is interesting to note that the cable behaviour described above leads to an increase in the bridge stiffness if the forces (stresses) are increased. This is depicted in Figure 2.3 and clearly distinguishes the force-displacement behavior of cable-supported structures from standard structures. Cable-supported structures can be classified as being of the geometric-hardening type.

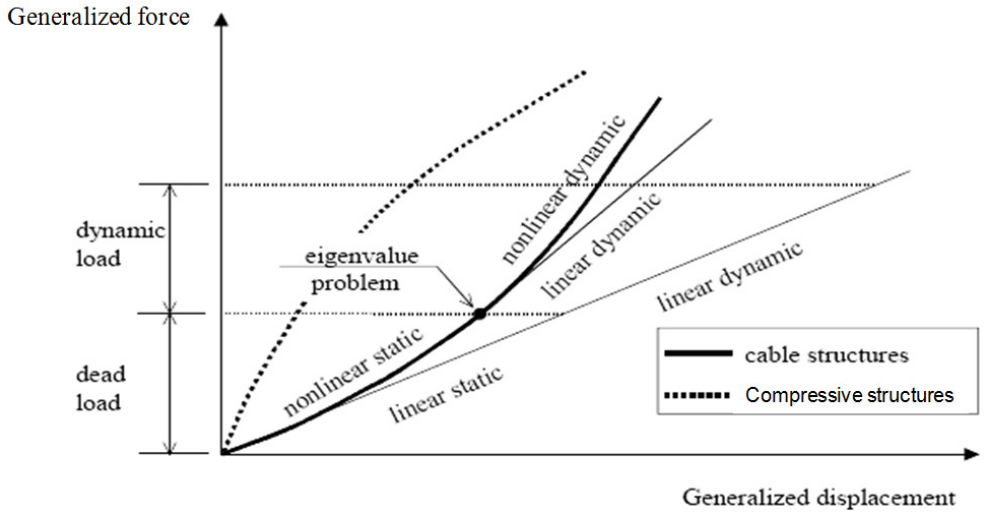

Figure 2.3. The difference between the behavior of cable structures and non-cable structures and accuracy results from different analysis procedures (Karoumi, 1999)

The nonlinear behaviour of the tower and girder (deck) elements due to axial force-bending moment interaction (P-Delta effects) is usually accounted for by calculating updated bending and axial stiffness of the elements under increasing deformations.

As a third source of nonlinearity, the total change in the bridge geometry can be accounted for by updating the geometry by adding the incremental nodal displacements to the previous nodal coordinates before recomputing the stiffness of the bridge in the deformed configuration.

2.4. Geometrically Nonlinear Analysis

As a more refined alternative to using the modified stiffness procedure mentioned above, a geometrically nonlinear analysis can be carried out when a structure undergoes large displacements and the change of its geometric shape renders a nonlinear displacement-strain relationship. The geometric nonlinearity may exist even in the state of linear elastic material behavior. Cable-supported structures such as suspension bridges and cable-stayed bridges are typically analyzed considering geometric nonlinearity. The geometrically nonlinear analysis must be carried out incrementally if a structure exhibits significant change of its shape under applied loads such that the resulting large displacements change the coordinates of the structure or additional loads like second-order moments (P-Delta effects) are induced (Figure 2.4).

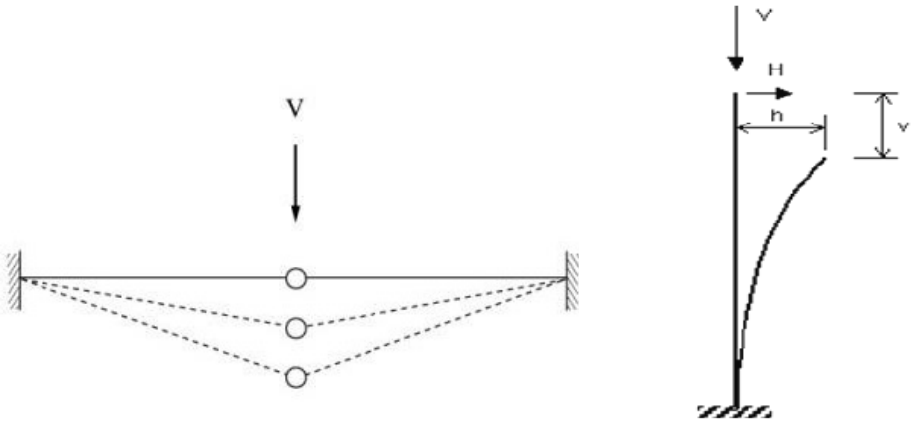

Figure 2.4. Illustrations of geometrically nonlinear behavior

The essence of geometrically nonlinear large-displacement analysis is to update the nodal coordinates after every load step. Additional loading is applied to the deformed geometry configuration of the structural model. On the other hand, in linear analysis, the calculations are based on loads applied to the original, undeformed geometry. If the deformations are not significantly large, both analysis schemes converge to the same result.

Geometric nonlinearity is accounted for using four basic formulations: total Lagrangian, updated Lagrangian, Eulerian, and co-rotational. In the Lagrangian formulations all variables are referred to a reference configuration. This will be the

undeformed configuration in what is termed total Lagrangian, or the configuration at the last converged solution in what is termed updated Lagrangian. A Lagrangian approach tends to be preferred in structural problems where it is required to monitor the path of a particular particle through space. It is thus termed a referential or material description. The derivation which follows applies to both total and updated versions except where the differences are highlighted. The limits of integration are carried out over the undeformed configuration for the Total approach and the configuration at the last converged solution for the Updated approach.

In the Eulerian formulation, all variables are referred to the deformed configuration. In the past this has been preferred for fluid problems where it is required to monitor the path of fluid through a particular control volume and not the path of one particle in its entirety. It is thus termed a spatial description. For structural problems its use has been limited as the deformed configuration is unknown. In the co-rotational formulation all strains are computed in a local frame which follows the element as it deforms. This approach is generally applicable, but is especially useful when used to formulate elements with rotational degrees of freedom.

The program SAP2000, which was used in this study for the geometrically nonlinear analysis studies, tracks the position of the element using an updated Lagrangian formulation. For frame, shell, and link/support elements, rotational degrees of freedom are updated assuming that the change in rotational displacements between steps is small.

2.5. Material Nonlinearity

Material nonlinearities arise when one or more bridge elements exceed their elastic limits due to member forces (axial forces or combined axial forces and bending moments). In analysis of cable-supported bridges, some researchers disregarded all sources of nonlinearities (e.g., Krishna et al., 1985), whereas others (e.g., Adeli and Zhang, 1995) also included material nonlinearity in the analysis. Although most nonlinear analyses of cable-supported bridges have focused on plane (Fleming, 1979) or space (Kanok-Nukulchai and Guan, 1993; Boonyapinyo et al., 1994) geometric nonlinear behavior, some studies (Nakai et al., 1985; Seif and Dilger, 1990), involving both geometric and material nonlinearities,

revealed that the material nonlinearities may be important in the ultimate load-carrying capacity of concrete-deck cable-stayed bridges. In the studies by Ren (1999) for example, material nonlinearities become relevant for the ductility capacity and energy absorption capacity of the bridge under strong seismic ground motions. In that study, however, the problem was reduced to two dimensions in order to achieve depth with respect to the material nonlinearities. Material nonlinearities were also not considered within the scope of the present study, since only the geometrically-nonlinear response of cable-supported bridges was investigated, and ductility and energy-absorption capacities were not evaluated.

2.6. Modeling of Elastic Cable Elements

As popularity of cable-supported structures has increased throughout the world, the search for more efficient modeling methods has intensified, and various cable modeling techniques can presently be found in the literature. In the study of Baron and Lien (1973), a 2-node curved finite element was developed, using cubic polynomial interpolation functions, and was used for the static and dynamic analysis of 3-D prestressed cable nets. In the study of Ozdemir (1979), another 2-node curved finite element model was developed using Lagrangian functions, for interpolation of element geometry. In the studies of Box et al, (1994) derivations of isoparametric cable elements, which include the element curvature, are presented; and in later studies, a four-node isoparametric cable element was presented and used for modeling of cables in cable-stayed bridges.

An iterative analysis procedure for cables, based on using “exact” analytical expressions for the elastic catenary, was suggested by Chang and Park (1989). This approach was later adopted by other investigators, and used for the analysis of very simple cable structures and power transmission lines.

The software SAP2000 (2007) used in the present analytical study follows the elastic catenary tangent stiffness formulation described in the following section. The formulation can be used for large-sag cables such as suspension bridge main cables, cables in long span cable-stayed bridges, and cables in large cable roofs, where straight elements are not strictly applicable.

2.7. Tangent Stiffness of an Elastic Catenary Cable Element

Calculation of the tangent stiffness for an elastic catenary cable element, which can be applied for geometrically nonlinear analysis, is described in this section. The cable element shown in Figure 2.5 is defined with an unstretched length of L_0, and two end nodes *i* and *j*, with three translational degrees of freedom at each node, defined in the x, y, z coordinate system. The cross-sectional area of the cable is denoted by A_o. The translational displacements along the six nodal degrees of freedom are defined by the six nodal displacements Δ_1 to Δ_6. The equilibrium conditions between the nodal forces can be expressed as:

$$F_4 = -F_1 \tag{2.2}$$

$$F_5 = -F_2 \tag{2.3}$$

$$F_6 = -F_3 - w_0 L_0 \tag{2.4}$$

where w_0 is the weight of the cable per unit length. Deformed dimensions (directional lengths) of the cable can be related to its undeformed directional lengths and appropriate nodal displacements, using the following expressions (Midas Civil, 2009):

$$l_x = l_{x0} - \Delta_1 + \Delta_4 = f\left(F_1, F_2, F_3\right) \tag{2.5}$$

$$l_y = l_{y0} - \Delta_2 + \Delta_5 = g\left(F_1, F_2, F_3\right) \tag{2.6}$$

$$l_z = l_{z0} - \Delta_3 + \Delta_6 = h\left(F_1, F_2, F_3\right) \tag{2.7}$$

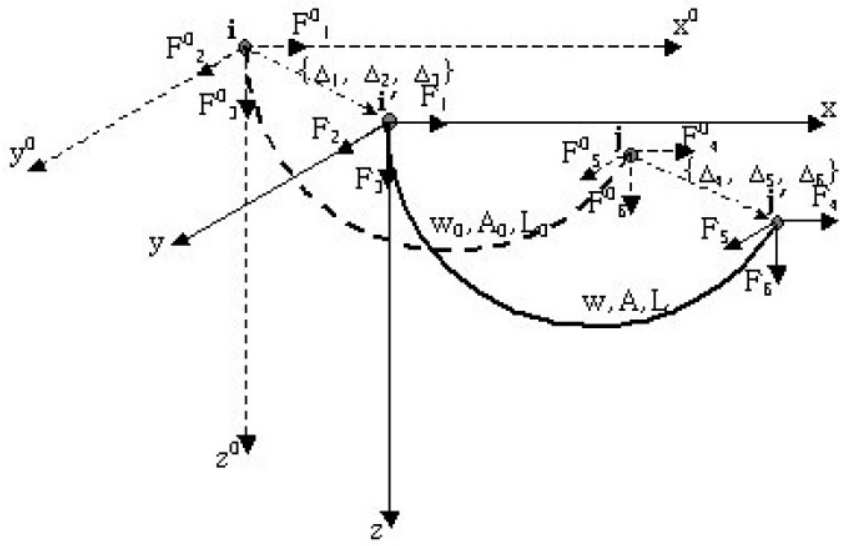

Figure 2.5. Tangent stiffness derivation for a catenary cable element (Midas Civil, 2009)

The differential equations for each directional length of the cable in the Global Coordinate System are given below. When the load-displacement relations are rearranged, the flexibility matrix $[F]$ of the cable can be obtained. The tangent stiffness matrix $[K]$ can then be obtained by inverting the flexibility matrix. The stiffness of the cable cannot be obtained immediately; rather, repeated analyses are carried out until an equilibrium state is reached.

$$dl_x = \frac{\partial f}{\partial F_1} dF_1 + \frac{\partial f}{\partial F_2} dF_2 + \frac{\partial f}{\partial F_3} dF_3 \tag{2.8}$$

$$dl_y = \frac{\partial g}{\partial F_1} dF_1 + \frac{\partial g}{\partial F_2} dF_2 + \frac{\partial g}{\partial F_3} dF_3 \tag{2.9}$$

$$dl_z = \frac{\partial h}{\partial F_1} dF_1 + \frac{\partial h}{\partial F_2} dF_2 + \frac{\partial h}{\partial F_3} dF_3 \tag{2.10}$$

$$\begin{Bmatrix} dl_x \\ dl_y \\ dl_z \end{Bmatrix} = [F] \begin{Bmatrix} dF_1 \\ dF_2 \\ dF_3 \end{Bmatrix}, \text{ where } [F] = \begin{bmatrix} \frac{\partial f}{\partial F_1} & \frac{\partial f}{\partial F_2} & \frac{\partial f}{\partial F_3} \\ \frac{\partial g}{\partial F_1} & \frac{\partial g}{\partial F_2} & \frac{\partial g}{\partial F_3} \\ \frac{\partial h}{\partial F_1} & \frac{\partial h}{\partial F_2} & \frac{\partial h}{\partial F_3} \end{bmatrix} = \begin{bmatrix} f_{11} & f_{12} & f_{13} \\ f_{21} & f_{22} & f_{23} \\ f_{31} & f_{32} & f_{33} \end{bmatrix} \tag{2.11}$$

$$\begin{Bmatrix} dF_1 \\ dF_2 \\ dF_3 \end{Bmatrix} = [K] \begin{Bmatrix} dl_x \\ dl_y \\ dl_z \end{Bmatrix} \text{ where } [K] = [F]^{-1} \tag{2.12}$$

The components of the flexibility matrix are expressed in the following equations:

$$\begin{aligned} f_{11} = \frac{\partial f}{\partial F_1} = &-\frac{L_0}{EA_0} - \frac{1}{w}\left[\ln\left(F_3 + wL_0 + B\right) - \ln\left(F_3 + A\right)\right] \\ &-\frac{F_1^2}{w}\left[\frac{1}{B^2 + \left(F_3 + wL_0\right)B} - \frac{1}{A^2 + F_3 A}\right] \end{aligned} \tag{2.13}$$

$$f_{12} = \frac{\partial f}{\partial F_2} = -\frac{F_1 F_2}{w}\left[\frac{1}{B^2 + \left(F_3 + wL_0\right)B} - \frac{1}{A^2 + F_3 A}\right] \tag{2.14}$$

$$f_{13} = \frac{\partial f}{\partial F_3} = -\frac{F_1}{w}\left[\frac{F_3 + wL_0 + B}{B^2 + \left(F_3 + wL_0\right)B} - \frac{F_3 + A}{A^2 + F_3 A}\right] \tag{2.15}$$

$$f_{21} = \frac{\partial g}{\partial F_1} = f_{12} \tag{2.16}$$

$$f_{22} = \frac{\partial g}{\partial F_2} = -\frac{L_0}{EA_0} - \frac{1}{w}\left[\ln\left(F_3 + wL_0 + B\right) - \ln\left(F_3 + A\right)\right] - \frac{F_2^2}{w}\left[\frac{1}{B^2 + \left(F_3 + wL_0\right)B} - \frac{1}{A^2 + F_3 A}\right] \tag{2.17}$$

$$f_{23} = \frac{\partial g}{\partial F_3} = \frac{F_2}{F_1} f_{13} \tag{2.18}$$

$$f_{31} = \frac{\partial h}{\partial F_1} = -\frac{F_1}{w}\left[\frac{1}{B} - \frac{1}{A}\right] \tag{2.19}$$

$$f_{32} = \frac{\partial h}{\partial F_2} = \frac{F_2}{F_1} f_{31} \tag{2.20}$$

$$f_{33} = \frac{\partial h}{\partial F_3} = -\frac{L_0}{EA_0} - \frac{1}{w}\left[\frac{F_3 + wL_0}{B} - \frac{F_3}{A}\right] \tag{2.21}$$

$$\text{where, } A = \left(F_1^2 + F_2^2 + F_3^2\right)^{1/2}, \quad B = \left(F_1^2 + F_2^2 + \left(F_3 + wL_0\right)^2\right)^{1/2} \tag{2.22}$$

2.8. Nonlinear Analysis Solution Strategy

For the geometrically nonlinear analysis of a cable-supported bridge structure subjected to external loads, the geometric stiffness (K) is expressed as a function of the displacement of deformation (U), which in-turn is affected by the geometric stiffness itself to satisfy equilibrium. The process requires an incremental iterative analysis solution strategy, such as the Newton-Raphson method. The Newton-Raphson solution strategy illustrated in Figure 2.6 is a widely used nonlinear analysis solution strategy used for calculating displacements which create the internal forces that are in equilibrium with the given external loads. For the analysis, the tangent stiffness matrix [K], which is a nonlinear functional of the nodal displacement vector {U}, is rearranged in each cycle of repetitive calculations to satisfy equilibrium between internal forces and externally applied loads. A

solution within the allowable tolerance is obtained using the stiffness matrices through the process of iteration.

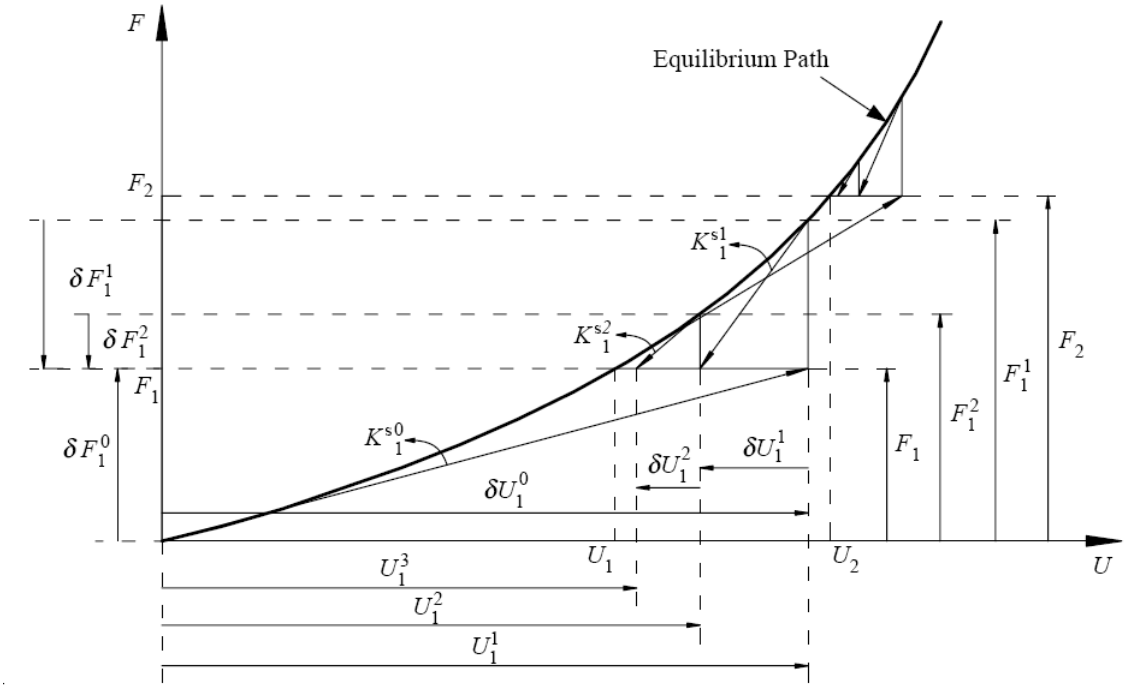

Figure 2.6. The Newton-Raphson solution strategy

The Newton-Raphson-based iterative procedure shown in the figure can be used to determine the deformed equilibrium configuration of a cable element or cable system. The procedure is initiated by calculation of the initial cable stiffness matrix for the first step of loading, $[K^{s0}{}_1]$. At the beginning of the first loading step, the nodal displacement vector $\{U\}$ consists of zero terms and the initial cable stiffness matrix is obtained for zero nodal displacement values.

$$\left\{U_1{}^0\right\} = \{0\} \tag{2.23}$$

$$\left[K^{s0}{}_1\right] = \left[K^s_{ini}\right] \tag{2.24}$$

where $\left[K^s_{ini}\right]$ is the initial cable stiffness matrix in the initial undeformed configuration.

Next, the nonlinear relationship between the nodal force vector and the nodal displacement vector can be linearized to solve for incremental nodal displacements for the *i*'th load step and *j*'th iteration cycle, using:

$$\left\{\delta U_i^j\right\} = \left[K_i^{sj}\right]^{-1}\left\{\delta F_i^j\right\} \tag{2.25}$$

where $\left\{\delta F_i^j\right\}$ is equal to the external load vector $\left\{F_i\right\}$ for the first iteration (*j=1*).

The nodal displacement vector can be updated after each iteration cycle using:

$$\left\{U_i^{j+1}\right\} = \left\{U_i^j\right\} + \left\{\delta U_i^j\right\} \tag{2.26}$$

The updated cable stiffness matrix $\left[K_i^{sj+1}\right]$ is then calculated for the updated nodal displacement vector $\left\{U_i^{j+1}\right\}$, and the internal force vector $\left\{F_i^j\right\}$ is updated using:

$$\left\{F_i^{j+1}\right\} = \left[K_i^{sj+1}\right]\left\{U_i^{j+1}\right\} \tag{2.27}$$

The unbalanced force vector $\left\{\delta F_i^{j+1}\right\}$ between the external load vector $\left\{F_i\right\}$ and the internal force vector $\left\{F_i^{j+1}\right\}$ can then be calculated as:

$$\left\{\delta F_i^{j+1}\right\} = \left\{F_i\right\} - \left\{F_i^{j+1}\right\} \tag{2.28}$$

Solving for $\left\{\delta U_i^j\right\}$ within successive iterations, convergence is achieved by minimizing the vector of residual forces to a specified value of tolerance:

$$\frac{\left|\left\{\delta F_i^{j+1}\right\}\right|}{\left|\left\{F_i\right\}\right|} \leq \text{ tolerance} \tag{2.29}$$

and the analysis can proceed to the next load step. The procedure is generally expected to give quadratic convergence.

The program SAP2000 (2007), which was used in this study for geometrically nonlinear analysis, uses an incremental-iterative analysis procedure using the Newton-Raphson solution strategy.

3. STRUCTURAL COMPONENTS AND DETAILS

3.1. General

For the vast majority of existing long-span cable-supported bridges, the structural system can be divided into four main components, as illustrated in Figure 3.1:

(i) The stiffening girder (truss or box system) constituting the deck superstructure,
(ii) The cable system supporting the deck superstructure,
(iii) The towers (or pylons) supporting the cable system,
(iv) The anchor blocks (or anchor piers) supporting the cable system in vertical and horizontal directions.

The suspension system comprises main catenary cables and vertical or slightly inclined hanger cables connecting the stiffening girder to the main cable, as illustrated in Figures 3.1 and 3.2.



Figure 3.1. Suspension system with vertical hangers (Gimsing, 1998)

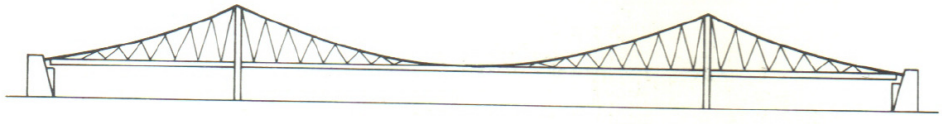

Figure 3.2. Suspension system with inclined hangers (Gimsing, 1998)

The cable-stayed system contains straight cables connecting the stiffening girder to the pylons. There are four types of cable configurations for cable stayed bridges, namely

the fan arrangement, the harp arrangement, the half-fan arrangement, and the star arrangement, as illustrated in Figure 3.3 and listed in Table 3.1.

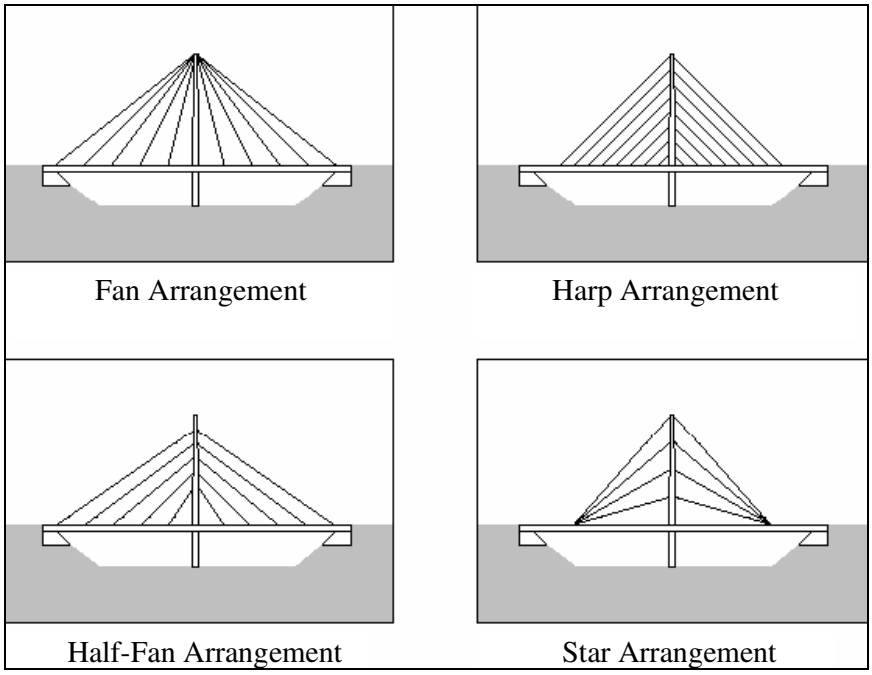

Figure 3.3. Stay cable configurations for cable-stayed bridges

Table 3.1. Descriptions of stay cable configurations for cable-stayed bridges

Cable Configuration	**Description**
Fan (often called radiating)	Cables run radiating from one point at pylon.
Harp	Cables run parallel from equal spacing at pylon.
Half-Fan (Modified fan)	Combination of fan and harp arrangement.
Star	Cables run from several points at pylon to one location at deck.

3.2. Force Transfer Mechanism in Cable-Supported Bridges

Cable-stayed bridges differ from suspension bridges in terms of the cable force transfer mechanism supporting the deck superstructure. In suspension bridges, the deck is supported by loosely-hung main cables with vertical suspenders (hangers), which predominantly behave as straight two-force members under tension forces. The main cables of a suspension bridge may be either externally-anchored (Figure 3.4), or can be anchored to the side-span boundaries of the deck for obtaining a self-anchored configuration (Figure 3.5). However, in cable-stayed bridges, the deck is supported directly by stay cables connected to the bridge towers (Figure 3.6), and no external anchorage is used.

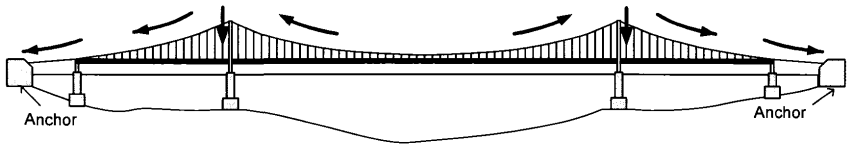

Figure 3.4. Cable force transfer mechanism for an externally-anchored suspension bridge (Son, 2008)

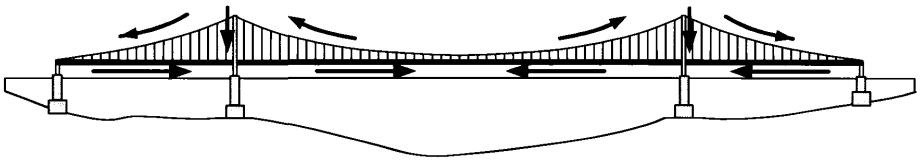

Figure 3.5. Cable force transfer mechanism for a self-anchored suspension bridge (Son, 2008)

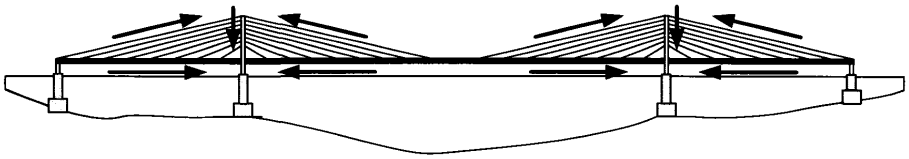

Figure 3.6. Cable force transfer mechanism for a cable-stayed bridge (Son, 2008)

3.3. Combined Cable-Stayed Suspension (CSS) Hybrid Bridges

Realization of ultra-long-span bridges, with a main span length ranging from 2000 meters to 3000 meters, is subject to proper consideration of aerodynamic stability issues. Accordingly, for the construction of next generation bridges following the Akashi-Kaikyo Bridge, research on new cable-supported bridges with high economic efficiency and high torsional rigidity have attracted much attention. Combined-type (Dischinger-type) cable-stayed suspension (CSS) hybrid bridges (Figure 3.7) were proposed to replace the conventional cable-stayed bridges (whose maximum possible span length does not typically exceed 1500 meters) they were predicted to be feasible for crossing ultra-long spans ranging from 2000 to 4000 meters. A combined cable-stayed suspension bridge constructed with a streamlined stiffening box-girder for the deck would combine the torsional stiffness of the cable-stayed counterpart with the aerodynamic effectiveness of the deck in order to provide the necessary torsional stability under wind effects.



Figure 3.7. Combined cabled stayed suspension (CSS) bridge configuration (Gimsing,1998)

Combined (CSS) hybrid systems comprising both the suspension and the cable-stayed components have been used as a type of cable-supported bridge as early as in the 19th century. One well-known example is the latest Brooklyn Bridge in New York, which has its main cable and vertical hangers supplemented by stay cables in fan configuration (Figure 3.8). Although few CSS hybrid bridges were built before the 1920's, after that time, this system was used in rehabilitation of some existing suspension bridges such as the aforementioned Brooklyn Bridge, the Tancarville Bridge in France, and the Salazar Bridge in Portugal (Gimsing, 1998). The CSS hybrid system was also proposed for design of numerous strait-crossing bridges around the world including the Great Belt East Bridge in Denmark, the Gibraltar Bridge, the Messina Strait Bridge, the Izmit Bay Bridge in Turkey, the Tagus River Bridge in Portugal and some strait-crossing bridges in Japan.



Figure 3.8. The Brooklyn Bridge in New York, U.S.A.
(Commercial Office Space News, 2010)

The combined cable-stayed-suspension (CSS) hybrid bridge, which is a combination of the traditional cable-stayed and the suspension bridge systems, has the following basic advantages over the two constitutive systems (Zhang and Sun, 2004a):

(i) Cost effective:

Compared with the suspension bridge of the same span length, the suspension portion is greatly shortened, so the tension forces in the main cables are greatly decreased, which helps reduce the construction costs of the main cables and the anchors, and the difficulty of constructing massive anchors in soft soil. In addition, different structural materials can be used in the suspension and cable-stayed portions. For example, a prestressed concrete girder can be used for the cable-stayed portion and a light steel box girder can be used in the suspension portion, therefore reducing in material cost. Torsional stability of the deck is also improved compared to the flexible suspension system.

(ii) Erection effective:

Compared with cable-stayed bridges of the same span length, the cable-stayed portion is greatly shortened, the height of towers can be significantly decreased,

and the axial compressive forces in the deck are also greatly reduced. The cantilevers in erection are also shortened, and the wind stability of the bridge during erection is therefore improved.

Therefore, CSS hybrid systems can make up for the deficiencies in the structural behavior, construction, economy and the wind stability of the traditional suspension and cable-stayed bridges, and therefore present a feasible alternative in design of ultra long-span bridges.

3.4. Structural Components of a Cable-Supported Bridge

3.4.1. Stiffening Girder

The role of the stiffening girder, constituting the deck superstructure, is to transfer mainly the vertical loads, including the self weight and the traffic loads, to the cable system. The girder can be constructed either of concrete or steel. For short spans, concrete girders are usually used because of their high capacity under compression. However, as the span length increases, the dead load crated by the self weight of the deck becomes critical, favoring the use of steel girders.

There are three types of stiffening girder cross sections commonly used for cable-supported bridges, as illustrated in Figure 3.9:

(i) Longitudinal edge beams
(ii) Box girders
(iii) Truss systems

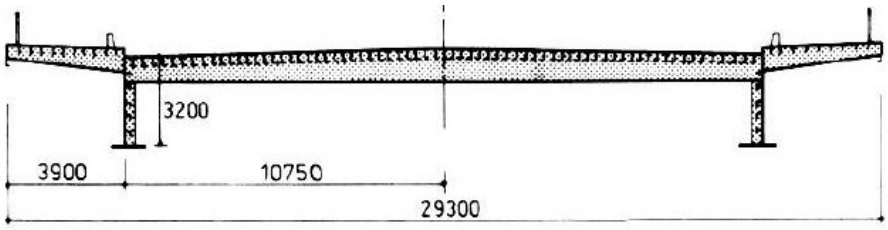

(i) Girder with longitudinal edge beams (Knie Bridge, Germany)

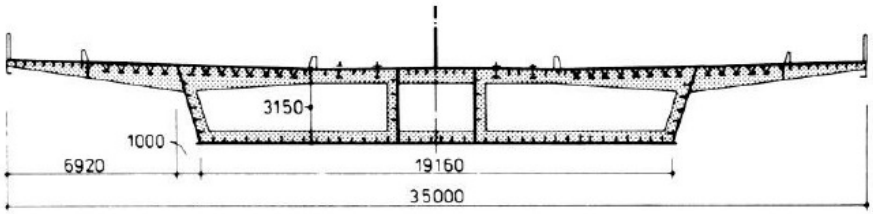

(ii) Box section (Oberkasseler Bridge, Germany)

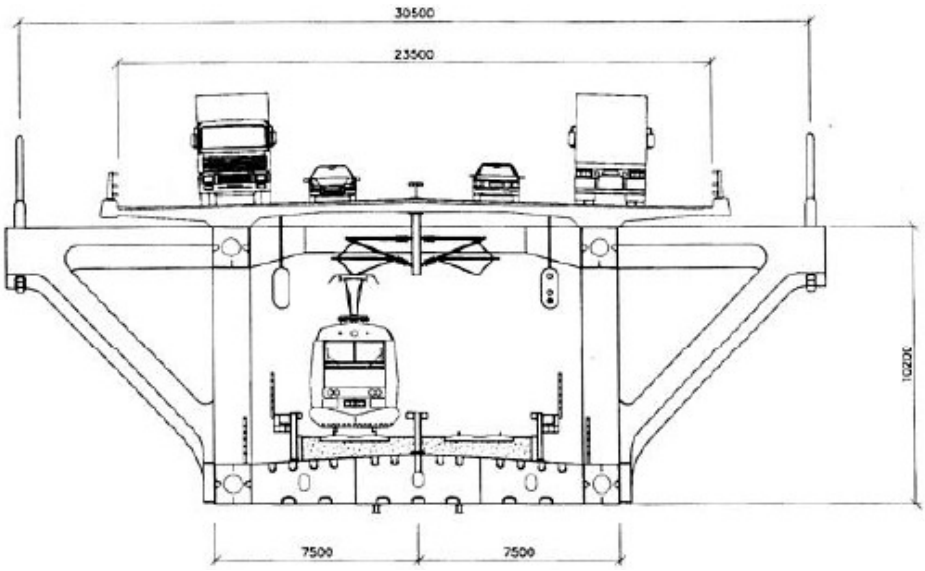

(iii) Steel truss section (Öresund Bridge, Sweden)

Figure 3.9. Conventional girder cross-sections (Gimsing, 1998)

To achieve longer spans and to maintain economy in material cost at the same time, it becomes apparent that cable-supported bridge deck design should consider the following:

(i) Dead load due to self weight must be kept to a minimum by introducing lighter deck cross-sections,

(ii) Wind effects in the form of drag, buffeting and vortex shedding must be kept to a minimum, by introducing aerodynamic shapes to the deck cross-section and abandoning the use of deep and heavy stiffening truss girders,

(iii) Flutter sensitivity must be kept to a minimum, by introducing a deck configuration, which, together with the cable geometry, provides a high overall torsional stiffness.

In cable-supported bridge design, a new concept was recently introduced, which involves using a single closed-box deck cross-section composed of stiffened steel panels (Figure 3.10). The self-weight of such a deck configuration is significantly low, and via assigning an aerodynamic shape to the deck cross-section, the system is subjected to low drag forces, as well as low buffeting and vortex shedding effects. In addition, the closed-box cross-section, when used together with a suitable cable configuration, provides an adequate level of torsional stiffness, resulting in lower flutter sensitivity associated with high critical wind speeds.

To achieve longer spans, deeper box cross-sections of the deck are required to provide adequate bending stiffness, which conflicts with the requirement to keep the self-weight and the wind effects low. True "streamlined" deck cross sections are characterized by a wind nose with a sharp edge to divide the air flow, and by plates with a modest inclination in relation to the direction of the wind (Figure 3.10). This further decreases the drag coefficient, and at the same time the tendency of the deck to be subjected to vortex shedding. The application of streamlined cross sections has therefore proved to be an efficient way to avoid the development of wind excited oscillations. The principle of streamlining the deck cross-section was first applied in the Severn Bridge built in the mid-1960s. Similar cross sections have later been used in the Bosphorus Bridge (1973) in Istanbul, Turkey, and the Humber Bridge (1981) in East Yorkshire, England.

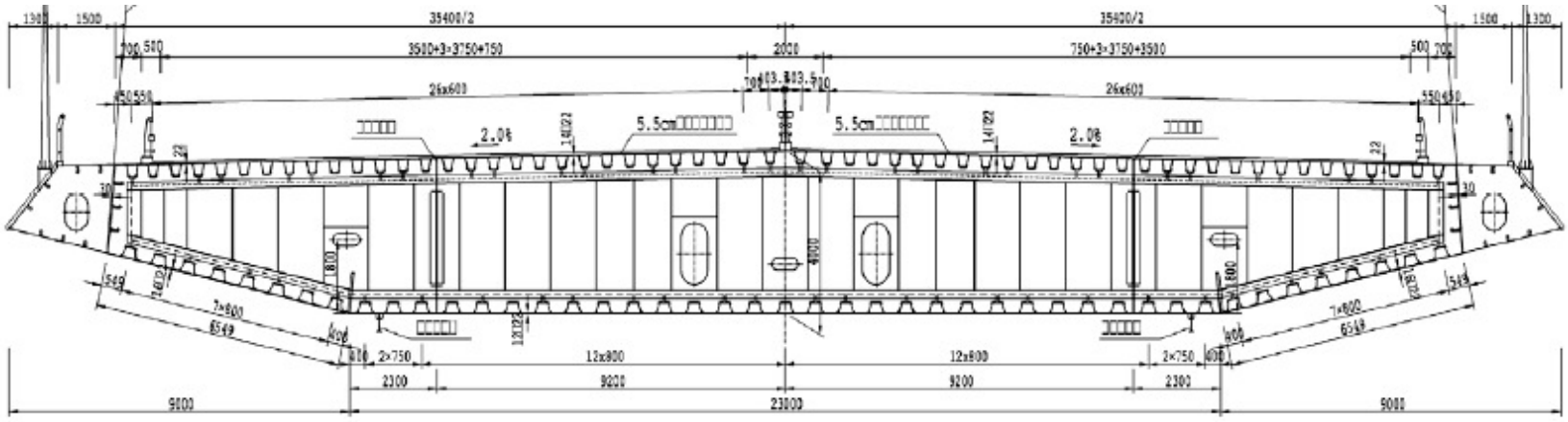

Figure 3.10. Aerodynamic (streamlined) closed-box deck cross-section (Vejrum, 2008)

3.4.2. Towers

The function of the towers (or pylons) is to support the cable system and to transfer the forces to the foundations. They are composed of columns or tower legs that are occasionally braced using struts (sway bracing) or cross-girders (portal bracing) to provide lateral stiffness and stability. Portal and sway bracings are also necessary to brace the tower columns against buckling, and to transmit wind forces and earthquake-induced loads to the foundations.

Typical configurations of cable-supported bridge towers are H shapes, A shapes, and λ shapes, as illustrated in Figure 3.11. Tower legs are generally tapered at the top for architectural purposes as well as to provide improved resistance to the transverse forces. Straight towers legs are designed as column members subjected to combined axial load and bending, where the axial loads are due to the vertical force resultant of the connecting cables and bending moments are induced by the unbalanced horizontal force resultant of the cables, as well as wind and earthquake effects.

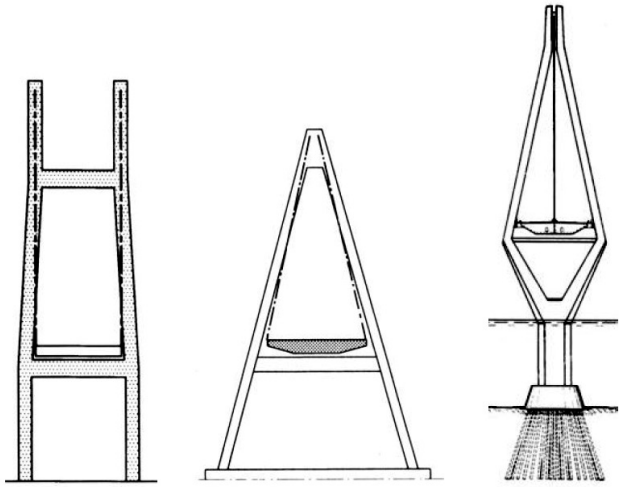

(i) H-shape (ii) A-shape (iii) λ-shape

Figure 3.11. Bridge tower configurations (Gimsing, 1998)

Towers may be hinged or fixed at the base, and can also take the form of a portal frame. Base fixity induces considerable bending moments in the tower, but this disadvantage is offset by the increased rigidity of the structure as a system. In addition, a

fixed base is practical for erection purposes, and may cost less than a heavy pinned bearing. Towers can be constructed of steel or reinforced concrete. Reinforced concrete towers are more economical than equivalent steel towers in terms of material cost, and also exhibit higher lateral stiffness. However, weight of reinforced concrete towers is considerably larger and therefore the selection also depends on the soil conditions present. Furthermore, construction time is significantly less for steel towers.

3.4.3. Cables

The basic element for all cables used in modern cable-supported bridge construction is steel wire, which has considerably larger tensile strength (both yield and ultimate) than ordinary structural steel. In most cases, a single steel wire is of cylindrical shape with a diameter between 3 mm and 7 mm. Typically, 5 mm wires are used in the main cable of suspension bridges and 7 mm wires in parallel wire strands are used for cable-stayed bridges. A cable may be composed of helically wound strands, parallel wire strands, or locked coil strands, as shown in Figure 3.12.



(i) Multi-wire spiral strand

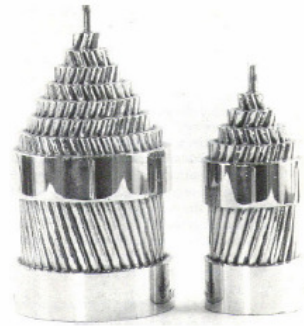

(ii) Multi-wire helical strand

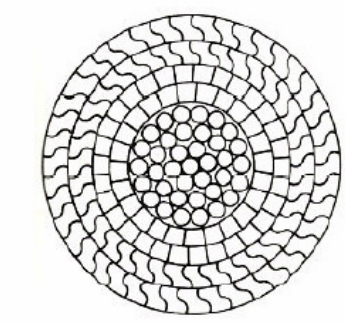

(iii) Locked coil strands

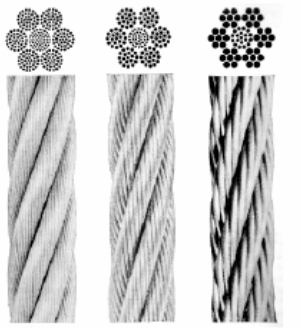

(iv) Twisted strand-type cables

Figure 3.12. Wire strand types and cable construction (Gimsing, 1998)

In particular, locked coil strands consist of three or more layers of twisted wire. The core is a normal spiral strand, and it is surrounded by several layers of wedge or keystone-shaped wires, and finally by several layers of Z-shaped or S-shaped wires. The advantages of this type of cable include a more effective protection against corrosion, and more favorable properties compared with the other arrangements. Their density is 30% higher than normal spiral strands, thus enabling slimmer cables which are less sensitive to wind effects. As well, their modulus of elasticity is 50% higher compared with normal strands of the same diameter. In addition, they are largely insensitive to bearing pressures in radial direction because of better interaction between the individual wires.

The vast majority of existing cable-stayed and suspension bridges use galvanized locked-coil wire strands, which are assembled into the large diameter cables, which are usually of the parallel-strand type. Modern wire stay cables are made up of a predetermined number of parallel or semi-parallel wires enclosed in an ultraviolet (UV) resistant high-density polyethylene (HDPE) pipe or sleeve of circular cross-section (Figure 3.13). The individual wires generally have a diameter of 7 mm, are individually galvanized and are of low relaxation grade steel, with nominal cross-sectional area of 38 mm^2 and a minimum guaranteed ultimate tensile stress (GUTS) of 1670 N/mm^2 or 1770 N/mm^2. For comparison, the ultimate stress of regular St37 structural steel is only 370 N/mm^2. The voids between the individual wires and the HDPE sheathing are filled with a corrosion inhibitor.

Strand stay cable configurations are traditionally anchored by means of wedges, which bite into the strand and transfer the load into an anchor head and the supporting bearing plate. Epoxy and bond type anchorages have also been used in the past. Modern cables are generally made up of a predetermined number of parallel arranged strands enclosed in an UV resistant HDPE stay pipe of circular cross-section. The individual strands have generally a diameter of 15.7 mm and are of low relaxation grade, with nominal cross-sectional area of 150 mm^2 and a “minimum guaranteed ultimate tensile stress” (GUTS) of 1770 N/mm^2 to 1860 N/mm^2. The strands are galvanized, greased or waxed and individually sheathed with a continuous and wear resistant HDPE coating, providing each strand with a triple protection system.

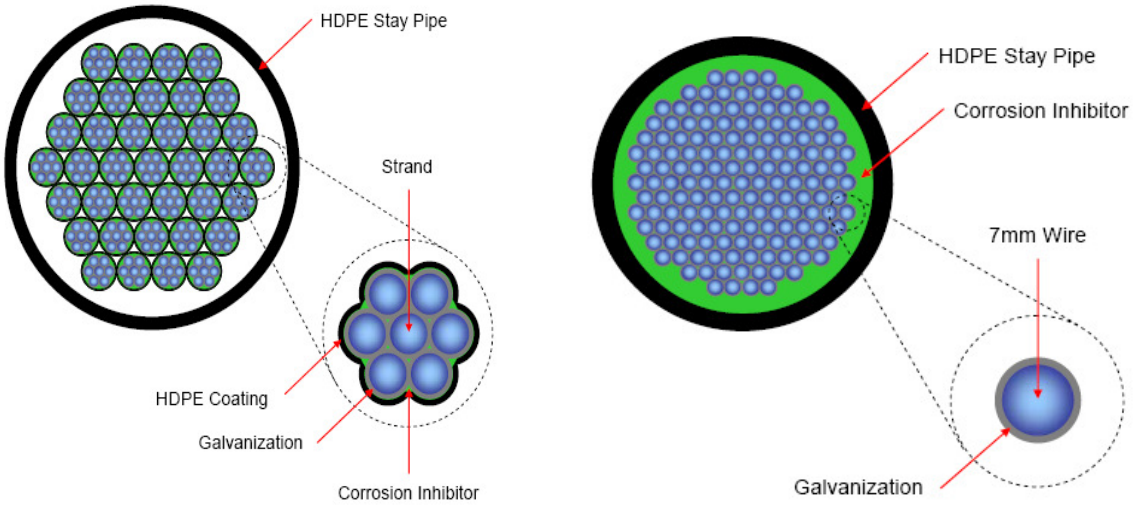

(i) Wire cable (ii) Strand cable

Figure 3.13. Wire stay cable and strand stay cable cross sections (Poser, 2002)

3.4.4. Anchorage Blocks

As mentioned in Section 3.2, the cable-supported bridges can be characterized by not only the cable configuration, but also with respect to the cable anchorage system. In earth-anchored systems, both the vertical and horizontal components of cable forces are transferred to anchor-blocks. This system can be applied for anchored suspension bridges (Figure 3.4), where the large tension forces in the main catenary cables are transferred into the ground, through anchorage blocks located on the ground beyond the towers. For such systems, it is crucial that the anchorage blocks are situated at locations where the ground possesses favorable geotechnical characteristics. On the other hand, in self-anchored suspension systems (Figure 3.5), the cable forces are transferred to the bridge deck side-spans, with the horizontal force components transmitted to the stiffening girders as axial compression. Figure 3.14 shows an anchorage block in construction stage, for an earth-anchored suspension bridge.

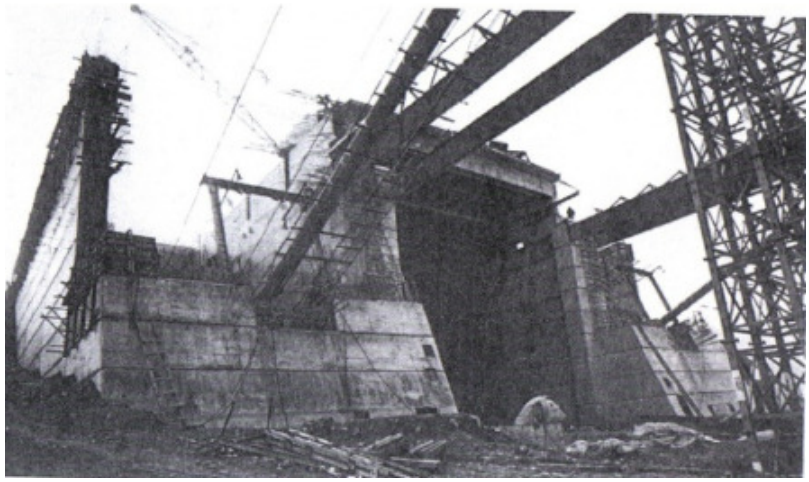

Figure 3.14. Anchorage block (Smith, 2009)

3.4.5. Cable Anchorages

Cable anchorages constitute the connections between the suspension or stay cables of a bridge to the bridge towers and the bridge deck (stiffening girder). Numerous techniques and devices are available for these connections, depending on the configuration of the bridge towers, the bridge deck and, the cables.

Cable anchorages on the bridge towers may be either fixed or movable. The connections may be located either at the top of each tower, or at intermediate locations, depending mainly on the number of cables used. While fixed connections can be created either by means of pins or sockets, movable anchorages incorporate either roller or rocker devices (Figure 3.15).

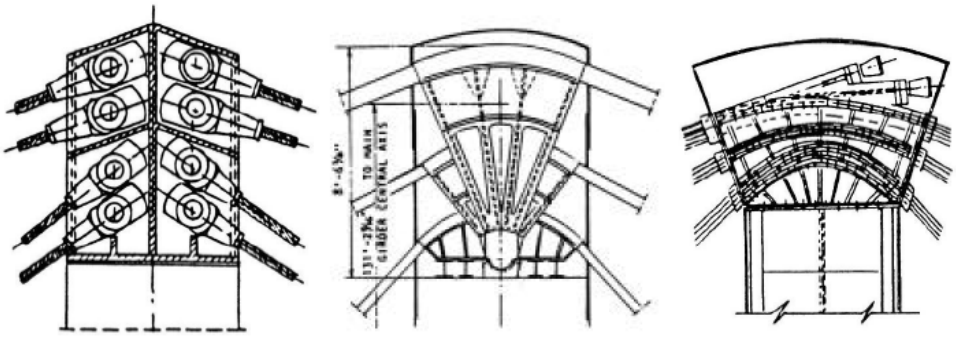

(i) Pin-connected anchorage (ii) Rocker-type anchorage (iii) Socket-type anchorage

Figure 3.15. Tower–cable anchorage configurations (Troitsky, 1988)

Special anchorages (e.g., Figure 3.16) are used for connecting the suspension or stay cables to the bridge deck (stiffening girder). These anchorages include an anchorage block for connecting the cable end to the stiffening girder component. The anchorage block incorporates anchor heads and hollow tubes, extending in registry with anchor head passages at one end and terminating at the opposite end of the anchorage block. Such cable anchorages facilitate pretensioning of the cables and adjustment of cable lengths (prestraining) during construction for the cable-stayed or suspension system to reach its intended geometric configuration under its own self weight.



Figure 3.16. Freyssinet stay cable – deck anchorage (PTI, 2001)

4. STRUCTURAL ANALYSIS METHODOLOGIES

4.1. Static Analysis under Dead Load and Initial Equilibrium Condition

In design of cable-supported bridges, the dead load (self weight) not only comprises the majority of the design load on the bridge, but also has a significant influence on the bridge stiffness. Before analysis of the bridge under live loads, wind loads, or dynamic effects, a geometrically-nonlinear static analysis should be conducted for the structural system under dead loads only. The objective of this initial geometrically-nonlinear static analysis is to achieve the initial equilibrium configuration of the bridge under dead loads; that is, to determine the "prestressed" state of the structural components that will, together with the dead loads, will produce a deformed geometry that will be identical with (or close to) the intended geometrical configuration of the bridge.

Adjusting the initial strain (prestraining) in suspension or stay cables is the key factor to attain the initial (deformed) equilibrium configuration under dead. It is important to point out that the prestrains applied on the bridge model are not the actual mechanical (stress-compatible) strains in the cable elements, but rather the required change in the cable lengths (typically shortening) that will allow the deformed geometry of the bridge under dead loads to resemble the intended geometrical configuration.

It is also important to reach the initial equilibrium state of the bridge (via prestraining of bridge cables and geometrically nonlinear structural analysis under combined prestrain and dead load effects) to obtain the stiffness properties of the cable elements for further analysis. Once the initial equilibrium state of the bridge is reached at the end of the geometrically nonlinear analysis under combined prestrain and dead load effects, the bridge model will have attained its overall stiffness for further linear on nonlinear analysis under superimposed loads and dynamic actions.

The pretension forces in the cable elements at the initial equilibrium state determine the contribution of the cable elements to the overall stiffness of a long-span cable-supported bridge. Catenary cable elements derive practically all their lateral stiffness from

their state of deformation rather than their physical properties, making it necessary to determine the geometric stiffness of cable elements based on their state of deformation. As described in the previous chapter, the geometric stiffness of a structural element differs from the mechanical stiffness, in that it is a function of the element deformation, while the 'mechanical' stiffness is only based on the physical properties (area, moment of inertia, elastic modulus, etc.) of the element, and it becomes important to consider the geometric stiffness properties of cable elements for an accurate analysis of cable-supported bridges. For example, Ren (1999) conducted analytical studies on cable-stayed bridge model, with and without the contribution of the geometric stiffness in the analysis, and concluded that the contribution of the geometric stiffness of the cables is essential to obtain accurate results.

4.2. Static Analysis under Vehicular Loads

Vehicle loading is also one of the most influential load effects on long-span cable-supported bridge structures. For a reliable determination of traffic live loads for analysis of long-span bridges, it becomes necessary to review the specifications in current design codes. In this study, the traffic live load specifications in the American Association of State Highway and Transportation Officials Load and Resistance Factor Design (AASHTO-LRFD) code for highway bridges were implemented. AASHTO-LRFD specifications define various parameters, including design vehicle weight, axle loads, axle configuration, span length, position of the vehicle on the bridge (transverse and longitudinal), number of vehicles on the bridge (multiple presence), for efficient and reliable prediction of design traffic loads. The bridge model was analyzed under for the AASHTO-LRFD vehicular live load category "HL-93". HL-93 vehicular loading is the general loading type for the design of highway bridges, and consists of a combination of the design truck load, design tandem load, and design lane load. The definitions given in the AASHTO-LRFD for design tandem, design lane load, and design truck are provided below:

- The design tandem consists of a pair of 110000-N axles spaced 1200 mm apart. The transverse spacing of wheels is taken as 1800 mm.

- The design lane load consists of a load of 9.34 kN/m, distributed uniformly in the longitudinal direction. Transversely, the design lane load is assumed to be uniformly distributed over a 3000 mm width. The force effects from the design lane load are not subject to a dynamic load allowance.

- The weights and spacings of axles and wheels for the design truck are specified in Figure 4.1. The spacing between the two 145 000-N axles are varied between 4300 mm and 9000 mm to produce extreme force effects.

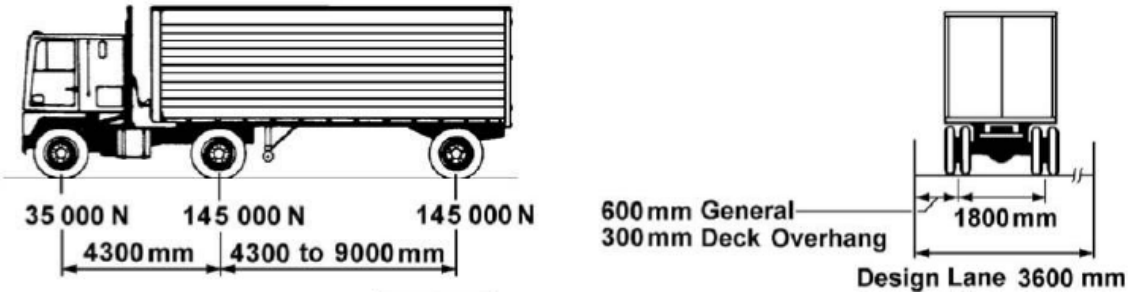

Figure 4.1. Characteristics of the design truck (AASHTO, 2007)

The AASHTO-LRFD Specifications for Highway Bridges define HL-93 live load as the extreme force effect taken as the larger of following (Lutomirska, 2009):

(i) The AASHTO-LRFD 3-axle design truck, and uniformly distributed design lane load of 9.34 kN/m (Figure 4.2).

(ii) The AASHTO-LRFD Design Tandem, and uniformly distributed design lane load of 9.34 kN/m (Figure 4.3).

(iii) For negative moment between points of contraflexure and reaction at interior piers, combination of two design trucks spaced at minimum of 15.5 m, and uniformly distributed design lane load of 9.34 kN/m, should be considered. All of the forces reduced to 90 % (Figure 4.4).

(For unit conversion 1 kip = 4.45 kN and 1 foot = 0.3048 meters)

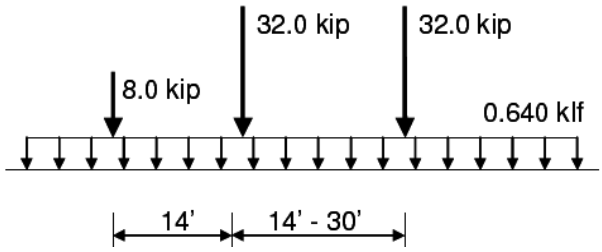

Figure 4.2. HL-93 Loading in AASHTO-LRFD for truck and lane load

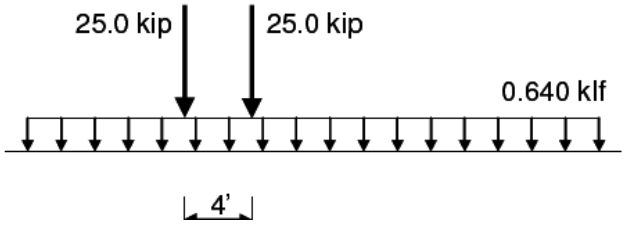

Figure 4.3. HL-93 Loading in AASHTO-LRFD for tandem and lane load

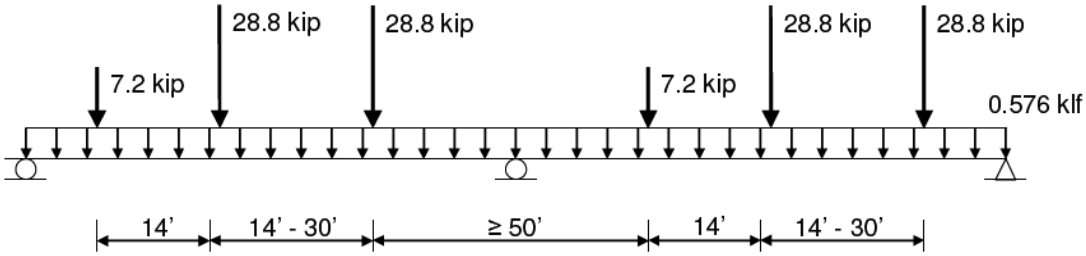

Figure 4.4. HL-93 Loading in AASHTO-LRFD for alternative load for negative bending moment between points of contraflexure and reaction at interior piers

For multilane bridges, multiple lane reduction factors are specified in most highway design codes. However, multilane factors defined in different codes vary significantly. In AASHTO-LRFD 2007, Section 3, Article 3.6.1.1.2, the extreme traffic load force effect is determined by considering each possible combination of the number of loaded lanes multiplied by a corresponding multiple presence factor to account for the probability of simultaneous lane occupation by the full HL-93 design live load. The values are shown in Table 4.1.

Table 4.1. Multiple Presence Factors (*m*) in AASHTO-LRFD

Number of Loaded Lanes	Multiple Presence Factor, *m*
1	1.20
2	1.00
3	0.85
>3	0.65

4.3. Moving Load Analysis

Advanced bridge analysis and design methods have been simplified with the aid of modern bridge software. Automated loading methods use influence surfaces which are a powerful tool for generating vehicle load patterns in accordance with the provisions of the various bridge codes. Complex load patterns can be generated to a high level of accuracy for any desired load effect in both two and three dimensional bridge models.

In the SAP2000 program, which was used for analysis purposes in this study, the "Bridge Analysis" tools were used to determine the response of the bridge model to the moving vehicle loads. The program possesses considerable capability and flexibility in determining the maximum and minimum displacements, forces, and stresses due to multiple and moving lane loads on the complex structure. Moving vehicle load effects can be combined with the static loads, the dynamic affects, and the temperature effects in order to obtain the envelopes of the individual response components.

In moving load analysis, the SAP2000 program considers all of the assignments within a "Moving Load" case, and tries every possible combination of loading along the traffic lanes, which are compatible with the vehicle classes created for the moving load cases. The maximum and minimum response quantities for a moving load case refer to the maximum and minimum values obtained for any combination of loading. In this study, the main scope of the moving load analysis was to obtain the maximum and minimum response of the bridge to extreme (maximum and minimum) loading configurations created

by moving load analysis of the system for design vehicle classes, rather than to investigate the effect of individual vehicles. The maximum and minimum internal force and displacement response quantities for the design vehicle classes defined for the HL-93 loading (defined in the previous section) were calculated as a result of the moving load analysis. HL- 93K and HL- 93M type vehicles were used in the moving load analysis, as specified in AASHTO-LRFD for the HL-93 loading type. Multiple presence factors defined in the previous section were also incorporated in the analysis.

4.4. Analysis for Temperature Effects

Temperature loading has a fundamental influence on the behavior of large-scale structures such as long-span cable-supported bridges. Generally, these types of structures are subjected to continuous temperature variations, primarily due to solar radiation and ambient air temperature. The temperature variations cause the bridge deck to expand and contract in the longitudinal direction, and to undergo bending deformation in the vertical plane, due to end restraints. Although deformations of the bridge may be accommodated by the bearings and expansion joints, large forces may develop in the bridge structure if any component of the movement is restrained. These forces sometimes may cause damage to the bridge structure.

In design of long-span bridges, temperature loading is generally characterized by the average temperature change applied along the longitudinal direction of a structural component, together with a transverse temperature gradient. In this study, for the temperature loading case, a uniform temperature change of ± 30°C was applied to the bridge deck and towers, as well as the tower cross beams and cable elements. Additionally, temperature gradients were considered in the two transverse directions for the deck, tower, and tower cross beams elements.

4.5. Analysis of Bridge Deck under Aerostatic Wind Forces

It has been commonly recognized that long-span bridges, cable-supported bridges in particular, are susceptible to significant wind effects. Wind actions to be considered in

design can be classified as design static wind forces and dynamic wind effects, as described in Table 4.2.

Table 4.2. Wind effects on a cable-supported bridge structure

Wind Effect	**Structural Property**	**Response**	**Effect**
Static Force	Shape Stiffness	Deflection	Stability Strength
Dynamic Action	Shape Stiffness Mass } Frequency Damping	Vibration	Stability Strength Occupant disturbance

The aerostatic and aerodynamic stability under the wind actions is a major concern for the design and construction of long-span cable-supported bridges. Aerodynamic and aerostatic wind effects on a cable-supported bridge are described briefly in the following.

For the aerodynamic case, flutter and buffeting are two of the most critical mechanism that could adversely affect the bridge performance. In the flutter mechanism, the bridge deck extracts energy from the flow that may result in a continuously growing response if this energy exceeds the energy dissipated by mechanical damping (Scanlan, 1998). This type of mechanism eventually lead to destructive forces at a critical wind speed (commonly referred to as negative damping) on the bridge, as was the case in the Tacoma Narrows Bridge in 1940. Flutter is highly dependent on the cross sectional shape of the deck and an efficient way to improve the flutter behavior of a bridge is proper determination of the cross-sectional shape of the deck. Other prevention methods rely on providing additional damping sources to bridge by using external damping devices.

Buffeting is the random oscillatory response of the structure due to turbulence. The common causes of buffeting are the inherent turbulence in the oncoming wind. Buffeting generally does not cause catastrophic failure, but it plays an important role in the serviceability of the bridge.

Other important bridge aerodynamic wind response mechanisms are vortex shedding, galloping and oscillations caused by cable-deck interactions. Vortex shedding occurs as a result of an orderly array of vortices that form in the wake of a bridge deck, which cause pressure fluctuations and may produce oscillations of the bridge deck. Vortex shedding is generally observed at much lower wind speeds than flutter or buffeting, which makes it an important consideration for serviceability and occupant discomfort issues. Galloping is the instability of very slender structures (Scanlan, 1998), which occurs due to changing angle of attack of wind to the structure and depends on the across wind velocity of the cross section. It creates oscillations at much lower frequencies and wind speeds than those observed in vortex shedding. Finally, cable-deck interaction is observed when a particular mode of vibration of the deck is at a same time frequency as the mode of vibration of individual stay cables. Ongoing research is oriented towards fully understanding this behavior.

On the other hand, aerostatic wind effects, which are more directly considered in design applications, is defined as the combined action of three components of the so-called equivalent aerostatic wind force on the bridge, namely the drag force, lift force and twist moment as illustrated in Figure 4.5 for a bridge deck (Xiao and Cheng, 2004). The aerostatic forces changes with the deformation of bridge component, and can be therefore be characterized as the function of the effective attack angle between the wind flow and deformed bridge deck. Defining the wind effect with a mean wind velocity of V and an angle of incidence of α_0, and assuming the torsional angle of twist of the deck is θ, then the effective wind angle of attack is calculated as $\alpha = \alpha_0 + \theta$.

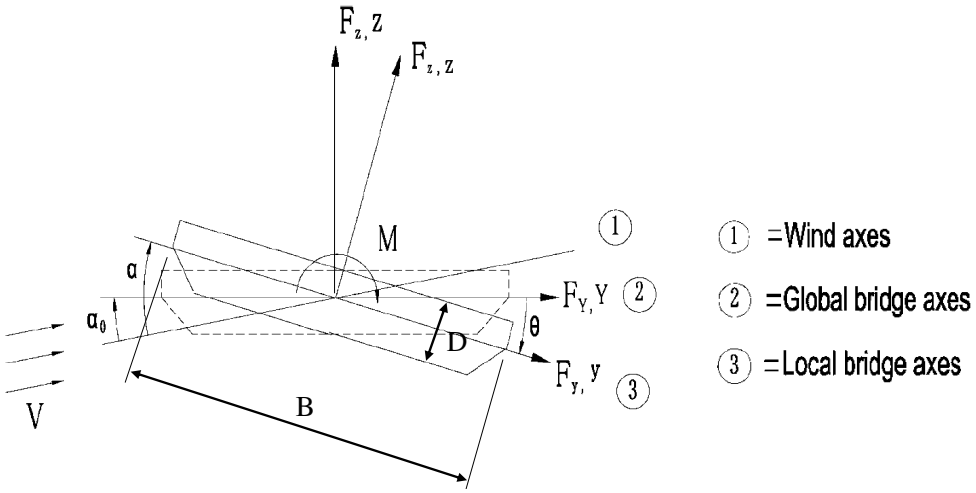

Figure 4.5. Motion of bridge deck and three components of wind loads in different axes (Xiao and Cheng, 2004)

Accordingly, the aerostatic forces acting per unit length of the bridge deck can be expressed as:

Drag force: $$F_y(\alpha) = \frac{1}{2}\rho V^2 C_y(\alpha) D \tag{4.1}$$

Lift force: $$F_z(\alpha) = \frac{1}{2}\rho V^2 C_z(\alpha) B \tag{4.2}$$

Pitch moment: $$M(\alpha) = \frac{1}{2}\rho V^2 C_M(\alpha) B^2 \tag{4.3}$$

where $C_y(\alpha)$, $C_z(\alpha)$, and $C_M(\alpha)$ are the aerostatic coefficients for calculating wind drag force, lift force, and pitch moment in local bridge axes, respectively; B is the deck width; D is vertical projected area of the deck, and ρ is the unit weight of air.

In this study, the aerostatic coefficients used were selected on the basis of comparison and evaluation of the analytical studies performed previously (Selberg, 1976) for three different bridge decks, namely the Pont de Normandie Bridge (Normandy, France), the Höga Kusten Bridge (in Angermanland, Sweden), and the Messina Straits Bridge (Italy). Deck cross-sections for the three bridges are shown in Figure 4.6.

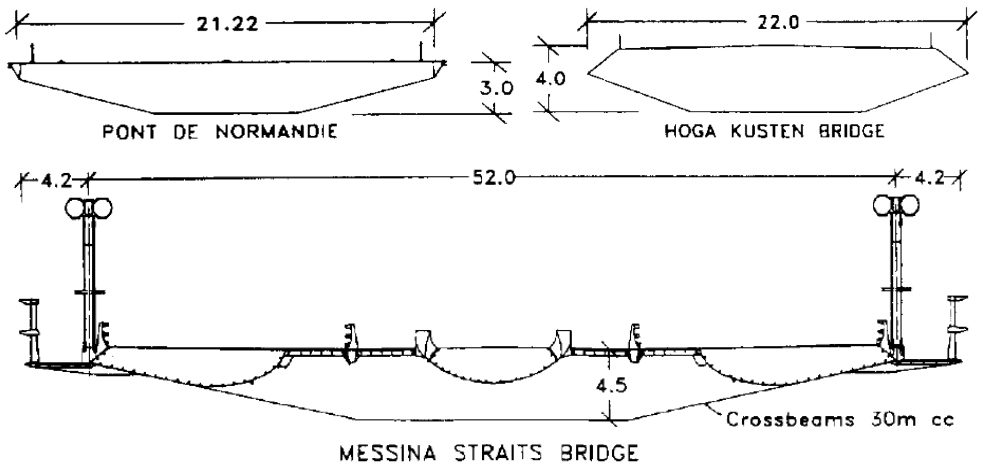

Figure 4.6. Deck cross-sections of the Pont de Normandie and the Hoga Kusten Bridge and the Messina Straits Bridge (dimensions in meters) (Larose and Livesey, 1997)

C_y, C_z and C_m coefficients obtained for the three bridge decks, for the case of horizontal (0°) wind incidence, are presented in Table 4.3, and compared to those obtained for a plat plate. The subscripts *y*, *z*, and *m* denote, respectively, the lateral, vertical and torsional degrees of freedom of the deck.

Table 4.3. C_y, C_z and C_m coefficients for the Messina Straits, Pont de Normandie, and Hoga Kusten Bridges, for 0° wind incidence (Larose and Livesey, 1997)

	Messina	**Normandie**	**Hoga-Kusten**	**Flat Plate**
C_y	0.09	0.05	0.10	0.06
C_z	-0.07	-0.41	-0.36	0.0
C_m	0.017	0.014	0.013	0.0

4.6. Analysis of Bridge Piers under Equivalent Static Wind Loads

Wind actions are also an important source of design load acting on tall bridge towers. The wind effect on a bridge tower can be divided into two components, namely the “along-wind effect” and the “across-wind effect”.

Along-wind loads are caused by the “drag” component of the aerostatic wind force on the tower, whereas the across-wind loads are caused by the corresponding “lift” component. The former is accompanied by “gust buffeting” causing a dynamic response in the direction of the mean flow, whereas the latter is associated with the phenomenon of “vortex shedding”, which causes the tower to oscillate in a direction perpendicular to the direction of wind flow. Most codes use an equivalent static procedure known as the gust factor method. This method is immensely popular and involves the determining of the wind pressure that acts on the tower due to the bearing on the face of the tower, a static wind load. This is then amplified using the gust factor to take care of the dynamic effects (Menon and Rao, 1997).

The following four code-based methods are widely used in international practice for design wind load calculations.

- Method 1 (ACI 307): the 1988 version of the ACI Chimney Code 7,
- Method 2 (Pinfold/NBCC): Pinfold's “RC Chimneys and Towers”, which employs the Canadian (NBCC-1980) wind load code recommendations,
- Method 3 (DIN 1056): the 1984 version of the German code for chimney design,
- Method 4 (CICIND): the 1984 version of the model concrete chimney code.

In these methods, the variation of mean wind speed with height z is generally described by the power law model proposed by Davenport (1961). The following form of the power law profile has been commonly adopted by Methods 1, 2 and 4 for the standard open terrain condition. The basic wind speed V_R is defined the mean hourly wind speed at 10m above the ground level in open flat country without having any obstructions.

$$v_z = V_R (z/10)^{0.14} \tag{4.4}$$

The mean wind pressure p_z (in Pascals) may be derived from the mean wind speed v_z (in m/s) thus:

$$p_z = \frac{1}{2}\rho_a v_z^{\,2} \tag{4.5}$$

where ρ_a is the density of air (1.34 kg/m^3). The design wind load w_z, and hence moment M_z, acting at height z on the tower is obtained as the sum of a mean (static) component and a dynamic component, reduced to an equivalent static form. The mean wind load w_{mz} (in N/m) at height z is obtained as;

$$w_{mz} = C_d d_z p_z \tag{4.6}$$

where d_z is the width of the tower cross section at height z, and C_d is the drag coefficient, specified as follows:

$$C_d = 0.65 \quad \text{for} \quad z < h - 1.5\,d_z \tag{4.7}$$

$$C_d = 1.0 \quad \text{for} \quad z \geq h - 1.5\,d_z \tag{4.8}$$

where h denotes the total height of the tower and $z = 0.75\,h$.

Since the tower structure is assumed to be free-standing, the mean bending moment M_{mz} at height z can be determined as:

$$M_{mz} = \int_z^h w_{m\xi}(\xi - z)\,d\xi \tag{4.9}$$

In the ACI 307 and the CICIND methods, a "gust factor" applies only to the bending moment at the base, and dynamic components need to be computed separately. The "dynamic" (equivalent static) load w_{dz} is assumed to vary linearly along the height of the tower (with a zero value at the base); this triangular distribution is scaled in such a way that the resulting moment at the base, when combined with the mean base moment, becomes equal to the product of the gust factor and the mean base moment M_{mz}. Hence, if

a common definition of gust factor is to be applied to all the methods under consideration, it must be defined as the ratio of the design moment M_o to the mean moment M_{mo} at the base of the tower (z = 0). The gust factor is accordingly denoted as G_o. The formulations for the determination of the design moment M_z, dynamic wind load w_{dz}, and the gust factor G_o are:

$$M_z = M_{mz} + \int_z^h w_{d\xi}(\xi - z)d\xi \tag{4.10}$$

$$w_{dz} = \left\{ \frac{3(G_o - 1)M_{mo}}{h^3} \right\} z \tag{4.11}$$

$$G_o = 1.30 + \frac{11.0\left[T_1 V_R / 0.3048\right]^{0.47}}{(h/0.3048 + 16)^{0.86}} \tag{4.12}$$

where T_1 denotes the fundamental period of vibration of the tower in the direction of wind loading, V_R is reference wind speed, and h is the height of the tower.

In this study, all wind load calculations for the bridge towers were performed according to ACI 307 specifications described above. However, to compare the various codal estimates (methods 1 to 4 above) for along-wind moments, a previous analytical study (Menon and Rao, 1996) on a chimney structure was reviewed. Results of this study showed that the discrepancies between various code methods were particularly prominent with regard to the dynamic (equivalent static) wind load profiles, as indicated in Figure 4.7 for the case of the chimney structure. The distribution of w_{dz} in the case of Methods 1 and 4 is triangular and unrelated to the corresponding distribution of mean loads w_{mz}. On the contrary, in Methods 2 and 3, the distribution of w_{dz} is similar to, and directly obtained from the distribution of w_{mz}. Since dynamic (inertial) forces are directly related to corresponding displacements, it follows from the boundary conditions that w_{dz} must necessarily be zero at the base and maximum at the top of the free-standing chimney. In this respect, the assumption of the triangular profile adopted by the ACI and CICIND,

which was also used in the present study for calculating wind loads on the bridge towers, is decidedly superior to the profiles assumed by the other two codal methods.

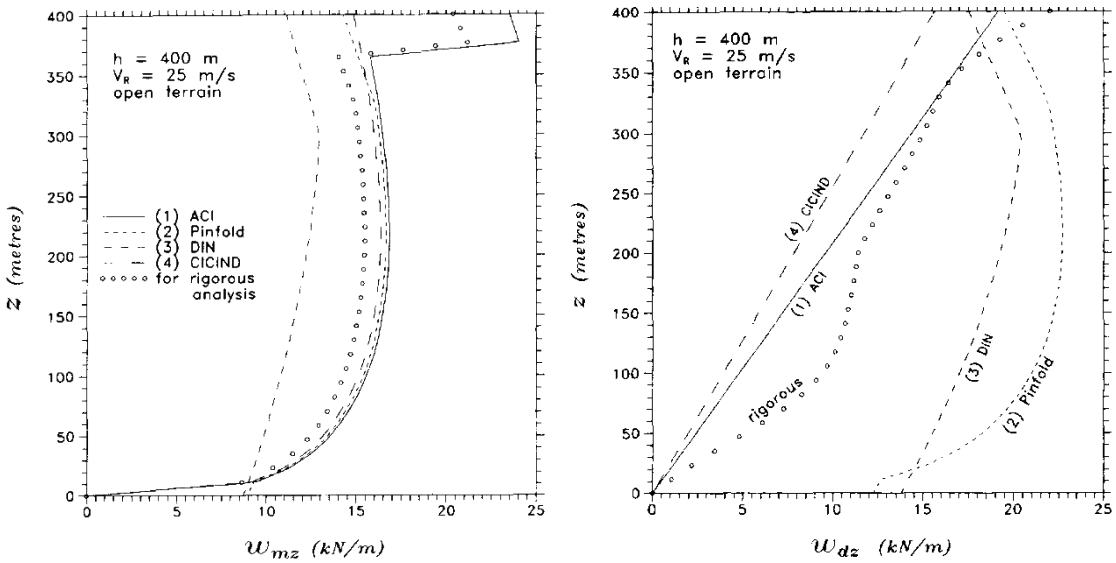

Figure 4.7. Mean wind load and dynamic wind load profiles predicted by the code methods

4.7. Analysis for Dynamic Earthquake Effects

4.7.1. Free Vibration (Modal) Analysis

Cable-supported bridge structures are more flexible than other structures, due to their structural configuration and large span length. One important aspect of cable-supported bridge response is the large displacement of the deck superstructure when subjected to dynamic actions. Therefore, proper determination of the dynamic and vibration characteristics of cable-supported bridge structures is essential for their earthquake response analysis.

The dynamic characteristics of a structure can be effectively analyzed in terms of natural frequencies and mode shapes. Free vibration (eigenvalue) analysis is required for determining dynamic (vibration) characteristics structure. The dynamic characteristics obtained by an eigenvalue analysis include vibration modes (mode shapes), natural frequencies (and periods) of vibration, and modal participation factors, which can be obtained using the mass and stiffness matrices of the structure.

Mode shapes and natural periods of an undamped free vibration are obtained from the characteristic equation below:

$$[K]\{\Phi_n\} = \omega_n^2 [M]\{\Phi_n\} \tag{4.13}$$

where, $[K]$: stiffness matrix

$[M]$: mass matrix

ω_n^2 : n^{th} mode eigen value (natural frequency squared)

$\{\Phi_n\}$: n^{th} mode eigen vector (mode shape)

Vibration modes take the form of natural shapes in which the structure freely vibrates or deforms. The first mode shape or natural vibration shape is identified by a shape that can be deformed with the least energy or force. The shapes formed with increases in energy define the subsequent higher modes. The natural period of vibration is the time required for the structure to complete one full cycle of the free vibration motion in the corresponding natural mode. The cylic frequency *f* and the natural period *T* of each mode are related to the natural (angular) frequency ω by:

$$T = \frac{1}{f} \quad \text{and} \quad f = \frac{\omega}{2\pi} \tag{4.14}$$

For the cable-supported bridge models analyzed in this study, extensive modal analyses were conducted to determine dynamic characteristics associated with their first 200 modes of vibration.

4.7.2. Response Spectrum (Modal Superposition) Analysis

Response spectrum analysis assumes the response of a multi-degree-of-freedom (MDOF) system as a combination of multiple single-degree-of-freedom (SDOF) systems. A response spectrum defines the peak values of responses corresponding to and varying with natural periods (or frequencies) of vibration that have been prepared through a

numerical integration process. Displacements, velocities and accelerations form the basis of a spectrum. Response spectrum analyses are generally carried out for seismic designs using the design spectra defined in design standards. To predict the peak design response values, the maximum response for each mode is obtained first and then combined by an appropriate statistical method.

Response spectrum analyses can be conducted in longitudinal, transverse, and vertical directions of the structure to determine, via modal superposition, the spectral (peak) response quantities of the structure when subjected to a design response spectrum or a response spectrum obtained from a particular earthquake ground acceleration time history.

An appropriate statistical method can be used for combination of modal results, such as the Complete Quadratic Combination (CQC) method or the Square Root of the Sum of the Squares (SRSS) method. The following equations describe the two methods of modal combination:

SRSS Method: $$R_{\max} = \left[R_1^{\,2} + R_2^{\,2} + ... R_n^{\,2} \right]^{1/2} \tag{4.15}$$

CQC Method: $$R_{\max} = \left[\sum_{i=1}^{N} \sum_{j=1}^{N} R_i \rho_{ij} R_j \right]^{1/2} \tag{4.16}$$

where, $$\rho_{ij} = \frac{8\xi^2 (1+r) r^{3/2}}{(1-r^2)^2 + 4\xi^2 r (1+r)^2}, \quad r = \frac{\omega_j}{\omega i} \tag{4.17}$$

$R_{\max}$: Peak response

R_i : Peak response of the *i*-th mode

r : Natural frequency ratio of the *i*-th mode to *j*-th mode

ξ : Damping ratio

The SRSS method has been widely used for modal superposition, but it tends to overestimate or underestimate the combination results in the cases where the values of natural frequencies are close to one another. As a result, the use of the CQC method has recently increased, as it accounts for probabilistic interrelations between the modes. The CQC method takes into account the statistical coupling between closely-spaced modes, caused by modal damping. Increasing the modal damping increases the coupling between closely-spaced modes, and if the damping is zero for all modes of vibration, the CQC method degenerates to the SRSS method.

For the cable-supported bridge models analyzed in this study, response spectrum analysis results using the CQC modal superposition method were compared with results of time history analyses, to evaluate the effectiveness of the modal superposition analysis method for long-span cable-supported bridge structures for which the modes are typically closely spaced.

4.7.3. Time History Analysis

The dynamic equilibrium equation for a structure subjected to a dynamic load (e.g., induced by ground acceleration) can be expressed as:

$$[M]\ddot{u} + [C]\dot{u} + [K]u = \{p\} \tag{4.18}$$

where, $[M]$: mass matrix

$[C]$: damping matrix

$[K]$: stiffness matrix

$\{p\}$: dynamic load vector

$\{u\}$: relative displacement vector

$\{\dot{u}\}$: relative velocity vector

$\{\ddot{u}\}$: total acceleration vector

Time history analysis seeks out a solution for the dynamic equilibrium equation when the structure is subjected to dynamic loads induced by earthquake ground accelerations. It calculates a time-variant structural response including displacements and member forces, within a given period of time, based on the dynamic characteristics of the structure and properties of the ground motion. There are several options that determine the type of time-history analysis to be performed:

- Linear versus nonlinear: Nonlinear time history analysis allows incorporating incorporates the geometrical and/or material nonlinearities in the dynamic response of the structure.

- Modal versus direct integration: These are two different numerical integration methods for solving the equation of motion, each with advantages and disadvantages. For nonlinear problems, direct integration time history analysis allows consideration of more types of nonlinearity that does modal superposition. Direct integration results are much more sensitive to time-step size compared with modal superposition results.

- Transient versus periodic: Transient analysis considers the applied load as a one-time event, with a beginning and an end. Periodic analysis considers the load to repeat indefinitely, with all transient response damped out. Periodic analysis is only available for linear modal time-history analysis.

In direct integration time history analysis, the damping in the structure is modeled using a full damping matrix. Unlike modal damping, this allows coupling between the modes to be considered. In the analysis, the structural damping matrix can be obtained via specifying a mass and stiffness proportional damping matrix (Rayleigh Damping), which may be defined as:

$$C = \alpha M + \beta K \tag{4.19}$$

where α and β are mass matrix and stiffness matrix coefficients, respectively. These two coefficients are computed by specifying two modal damping ratios corresponding to two natural frequencies of the structure. The modal damping ratios for other modes will thus be dependent on these two coefficients, and each mode will possess a different damping ratio (Figure 4.8).

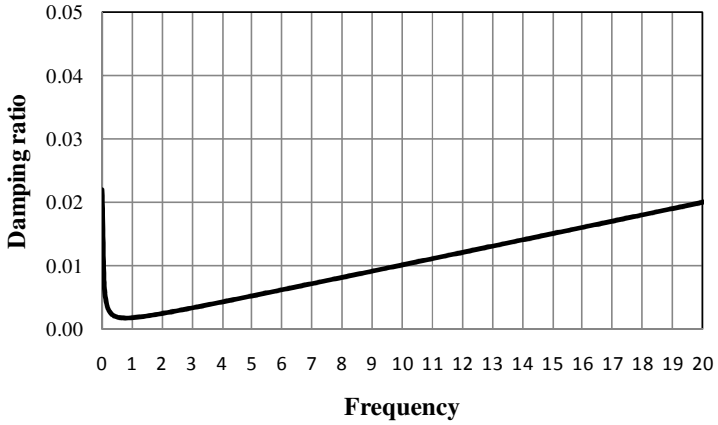

Figure 4.8. Dependence of damping ratio on modal natural frequency for Rayleigh damping

In this study, nonlinear linear time history analyses were conducted for the bridge structures investigated. Material nonlinearities were not considered in the analysis, similar to studies by various other researchers in the area.

4.8. Design Load Combinations, Limit States, and Design Capacities of Structural Components

4.8.1. Design Load Combinations and Limit States

The bridges modeled and analyzed in this study were subjected to code-compliant combinations of several types of design loads, including dead load, live load, temperature effect, wind load, and earthquake actions.

The dead load acting on the bridge models included the self weight of the structural components, the calculation of which is based on the specified value for the unit weight of

steel. Non-structural components, connections, and diaphragm beams in the transverse direction of the bridge deck are not included in the analysis model for the sake of simplicity. However, to consider the weight of the components not included in the model, additional (superimposed) dead loads were applied, mainly on the deck elements of the model.

Live load effects were determined by considering each possible combination of number of loaded lanes multiplied by a corresponding multiple factor to account for the probability of simultaneous lane occupancy. AASHTO-LRFD specifications on design traffic loads were used for live load analysis, as described in a previous section. Temperature effects were imposed on all components of the bridge model, as uniform temperature changes in longitudinal directions of the members and temperature gradients in their transverse directions. Aerostatic wind loads were applied on the stiffening girder (deck) in the form of combinations of drag forces, lift forces, and pitch moments. Equivalent static loads, which simulate dynamic wind effects, are also applied on the towers in each transverse direction. Earthquake actions are analyzed via application of the response spectrum analysis and the direct integration linear time history analysis methods described in the previous section.

In the analysis, the load effects were factored and superimposed according to AASHO-LRFD 2007, Section 3, Article 3.4 limit states. The AASHTO load factors and combinations used for the different limit states selected is shown in Table 4.4. In addition, load factors for permanent loads are presented in Table 4.5, where it is specified that the permanent load factor for the dead load of structural components and nonstructural attachments (γ_p) can be in the range of value 0.90 and 1.25. In this study, this value was taken as 1.0 in the load combinations, in order to attain the initial equilibrium condition of the bridge more realistically. The AASHTO-LRFD limit states used for design assessment of the bridges analyzed in this study were selected as:

- STRENGTH I: Basic load combination relating to the normal vehicular use of the bridge without wind loading.

- STRENGTH III: Load combination relating to the bridge exposed to wind velocities exceeding 90 km/hr.

- STRENGTH V: Load combination relating to the normal vehicular use of the bridge use of the bridge with wind of 90 km/hr. velocity.

- EXTREME EVENT: Load combination including earthquake actions.

- SERVICE I: Load combination relating to the normal operational use of the bridge with a 90km/hr. Wind and all loads taken at their nominal values.

Table 4.4. Selected load combination limit states and load factors in AASHTO- LRFD

Load Combination Limit States	DC	LL	WS	TU	TG	EQ
STRENGTH I	γ_p	1.75	-	0.50	0.50	-
STRENGTH III	γ_p	-	1.40	0.50	0.50	-
STRENGTH V	γ_p	1.35	0.40	0.50	0.50	-
EXTREME EVENT	γ_p	0.50	-	-	-	1.00
SERVICE I	1.00	1.00	0.30	1.0	0.50	-
DC: dead load of components and attachments LL: live load WS: wind load on structure TU: uniform temperature change TG: temperature gradient EQ: earthquake load						

Table 4.5. Load factors for permanent loads (γ_p) in AASHTO-LRFD

Type of Load, Foundation Type and Method Used to Calculate Downdrag	Load Factor	
	Maximum	Minimum
DC: Component and Attachments	1.25	0.90
DC: Strength IV	1.5	0.9

Accordingly, the load combinations used in this study can be listed as:

- $1.0DL + 1.75LL + 0.50Temp^{(+)}$
- $1.0DL + 1.75LL + 0.50Temp^{(-)}$
- $1.0DL + 1.40Wind_{(x)} + 0.50Temp^{(+)}$
- $1.0DL + 1.40Wind_{(y)} + 0.50Temp^{(-)}$
- $1.0DL + 1.40Wind_{(x)} + 0.50Temp^{(-)}$
- $1.0DL + 1.40Wind_{(y)} + 0.50Temp^{(+)}$
- $1.0DL + 1.35LL + 0.40Wind_{(x)} + 0.50Temp^{(+)}$
- $1.0DL + 1.35LL + 0.40Wind_{(x)} + 0.50Temp^{(-)}$
- $1.0DL + 1.35LL + 0.40Wind_{(y)} + 0.50Temp^{(+)}$
- $1.0DL + 1.35LL + 0.40Wind_{(y)} + 0.50Temp^{(-)}$
- $1.0DL + 0.50LL + 1.0EQ_{(x)} + 0.30EQ_{(y)}$
- $1.0DL + 0.50LL + 1.0EQ_{(y)} + 0.30EQ_{(x)}$
- $1.0DL + 1.0LL + 1.0Wind_{(x)} + 0.50Temp^{(+)}$
- $1.0DL + 1.0LL + 1.0Wind_{(x)} + 0.50Temp^{(-)}$
- $1.0DL + 1.0LL + 1.0Wind_{(y)} + 0.50Temp^{(+)}$
- $1.0DL + 1.0LL + 1.0Wind_{(y)} + 0.50Temp^{(-)}$

4.8.2. Design Capacities of Structural Components

Envelopes of the structural analysis results for the selected AASHTO-LRFD load limit states were compared with code-compliant member capacities, for strength-based design assessment of the bridges investigated in this study. AASHTO-LRFD specifications on calculation of member capacities and resistance factors are outlined in the following subsections.

4.8.2.1. Compressive Resistance. According to AASHTO LRFD Section 6, Article 6.9.2.1, the factored resistance of components in compression, P_r, is calculated as:

$$P_r = \phi_c P_n \tag{4.20}$$

where, ϕ_c = resistance factor for compression ($\phi_c = 0.90$)

P_n = nominal compressive resistance, as calculated below:

$$\text{If} \quad \lambda \le 2.25, \quad P_n = 0.66^{\lambda} F_y A_s \tag{4.21}$$

$$\text{If} \quad \lambda > 2.25, \quad P_n = \frac{0.88 F_y A_s}{\lambda} \tag{4.22}$$

in which, $\lambda = \left(\frac{Kl}{r_s \pi} \right)^2 \frac{F_y}{E}$ (AASHTO LRFD, Article 6.9.4.1)

λ : normalized column slenderness factor

F_y : specified minimum yield strength (MPa)

E : modulus of elasticity (MPa)

l : unbraced length (mm)

r_s : radius of gyration about the plane of buckling (mm)

K : effective length factor

A_s : gross cross sectional (mm^2)

4.8.2.2. Combined Axial Compression and Flexure. According to AASHTO LRFD, Article 6.9.2.2, the axial compressive load, P_u, and concurrent moments, M_{ux} and M_{uy}, acting on components, calculated for the factored loadings by elastic analytical procedures needs to satisfy the following relationship:

$$\text{If} \quad \frac{P_u}{P_r} < 0.2, \qquad \frac{P_u}{2.0 P_r} + \left(\frac{M_{ux}}{M_{rx}} + \frac{M_{uy}}{M_{ry}} \right) \le 1.0 \tag{4.23}$$

$$\text{If} \quad \frac{P_u}{P_r} \ge 0.2, \qquad \frac{P_u}{P_r} + \frac{8.0}{9.0} \left(\frac{M_{ux}}{M_{rx}} + \frac{M_{uy}}{M_{ry}} \right) \le 1.0 \tag{4.24}$$

where, P_r : factored compressive resistance as specified previously

M_{ux} : factored flexural moment about the x-axis on cross sections determined by analysis under factored loads (N.mm).

M_{uy} : factored flexural moment about the y-axis on cross sections determined by analysis under factored loads (N.mm).

M_{rx} : factored flexural resistance about the x-axis, taken equal to ϕ_f times the nominal flexural resistance (M_{nx}) about the x-axis (N.mm).

M_{ry} : factored flexural resistance about the x-axis, taken equal to ϕ_f times the nominal flexural resistance (M_{ny}) about the x-axis (N.mm).

ϕ_f : resistance factor for flexure (ϕ_f =1.0).

The nominal flexural resistance (M_n) for box shaped members will be taken as (AASHTO LRFD, Article 6.12.2.2.2):

$$M_n = F_y S \left[1 - \frac{0.064 F_y S l}{AE} \left(\frac{\sum \left(\frac{b}{t} \right)}{I_y} \right)^{0.5} \right] \tag{4.25}$$

where, S : section modulus about the flexural axis (mm^3)

A : area enclosed within the centerlines of the plates comprising the box. (mm^2)

l : unbraced length (mm)

I_y : moment of inertia about an axis perpendicular to the axis of bending (mm^4)

b : clear distance between plates (mm)

t : thickness of plates (mm)

4.8.2.3. Tensile Resistance. According to AASHTO LRFD, Article 6.8.2.1, the factored tensile resistance of a component is calculated as:

$$P_r = \phi_y P_{ny} = \phi_y F_y A_g \tag{4.26}$$

where, P_{ny} : nominal tensile resistance for yielding in gross section (N)

F_y : specified minimum yield strength (MPa)

A_g : gross cross sectional area of the member (mm^2)

ϕ_y : resistance factor for yielding of tension members. ($\phi_y = 0.95$)

4.8.2.4. Combined Tension and Flexure. According to AASHTO LRFD, Article 6.8.2.3, the axial tension, P_u, and concurrent moments, M_{ux} and M_{uy}, calculated on a member for the factored loadings by elastic analytical procedures need to satisfy the following relationship:

$$\text{If} \quad \frac{P_u}{P_r} < 0.2, \qquad \frac{P_u}{2.0P_r} + \left(\frac{M_{ux}}{M_{rx}} + \frac{M_{uy}}{M_{ry}}\right) \le 1.0 \tag{4.27}$$

$$\text{If} \quad \frac{P_u}{P_r} \ge 0.2, \qquad \frac{P_u}{P_r} + \frac{8.0}{9.0}\left(\frac{M_{ux}}{M_{rx}} + \frac{M_{uy}}{M_{ry}}\right) \le 1.0 \tag{4.28}$$

where, P_r : factored tensile resistance as specified previously

M_{ux} : factored flexural moment about the x-axis on cross sections determined by analysis under factored loads (N.mm).

M_{uy} : factored flexural moment about the y-axis on cross sections

M_{rx} : factored flexural resistance about the x-axis, taken equal to ϕ_f times the nominal flexural resistance (M_{nx}) about the x-axis (N.mm).

M_{ry} : factored flexural resistance about the y-axis, taken equal to ϕ_f times the nominal flexural resistance (M_{ny}) about the y-axis (N.mm).

ϕ_f : resistance factor for flexure (ϕ_f =1.0).

5. PRELIMINARY CASE STUDY: THE BOSPHORUS BRIDGE

5.1. Overview

As a preliminary case study, a three-dimensional structural model of the Bosphorus Bridge in Istanbul was created, and the model was used for conducting the static and dynamic analysis procedures described in Chapter 4. The types of analyses conducted on the Bosphorus Bridge model include geometrically-nonlinear static analysis under dead load and determination of the initial equilibrium configuration, moving load analysis under vehicular loads, analysis for temperature effects, analysis under aerostatic wind forces, and analysis for dynamic earthquake actions.

This chapter presents details of the structural modeling and analysis methodologies and load calculations, as well as the results of the static and dynamic analyses conducted for the Bosphorus Bridge. Results of the analyses were evaluated and the internal forces developing in critical structural members and displacements at critical locations under different load combinations were compared with the analysis results reported in the design calculations of the bridge, for evaluating the validity of the structural model created, as well as the validity of the load assignments and the analysis procedures used. The natural frequencies calculated for the bridge were also compared with previous free vibration analysis studies on the bridge.

For creating the structural model of the Bosphorus Bridge, information on the bridge geometry, structural component dimensions, section properties, material properties of the bridge were obtained from the design documents and drawings prepared by Freeman Fox & Partners (1968).

The structural model created considered only the main structural components of the bridge, including the main span stiffening girder (deck), the suspension cables, the hangers, the bridge towers, and the tower cross-beams. In the model, the hangers of the bridge were assumed vertical, instead of the actual inclined configuration, since the aim of the

preliminary case study was not to predict the response of the actual bridge with all its construction details, but to provide a reference analysis case for the proposed combined cable stayed suspension (CSS) hybrid bridge described in Chapter 6 of this thesis. Approach viaducts of the Bosphorus Bridge were also not considered in the structural model.

5.2. Description of the Bridge

The Bosphorus Bridge spans across the Bosphorus strait, which divides the European and Asian mainlands of the city of Istanbul. The bridge connects the Ortaköy and Beylerbeyi suburbs, and is a located on a densely-used intercontinental highway. At the time it was constructed in 1973, the Bosphorus Bridge ranked as having the 4th longest span among suspension bridges worldwide, and the one with the longest span outside the United States. At present, it has the 16th longest span among suspension bridges in the world. The bridge was designed by Freeman Fox and Partners, who were also responsible for the design of the Severn Bridge and the Humber Bridge, and who were reputed for their use of aerodynamic streamlined decks in long-span suspension bridge designs.

The Bosphorus Bridge was designed as a steel suspension bridge, having a main span length of 1074 meters, while the two side spans measure 231 meters and 255 meters, as shown in Figure 5.1. (Brown *et al*., 1976). The bridge incorporates 3 traffic lanes in each direction. A minimum clearance of 64 meters above the water level permits passage of the highest ocean going vessels. The piers of the suspension towers, which project 165 meters above the sea level, were constructed on dry land. In addition to providing a safe vessel overhead, this configuration considerably reduced the construction cost of pier foundations. The side spans of the bridge deck were designed as approach viaducts, where the deck segments along the side spans are supported by piers instead of using a suspension system. The side-span cables were designed as straight cables, with catenary action under self weight only, and the ends of the suspension cables were earth-anchored. In the design drawings of the bridge, the sag of main suspension cable is denoted as 93 meters, and the horizontal distance between hanger connections along the main span is specified as 17.9 meters.

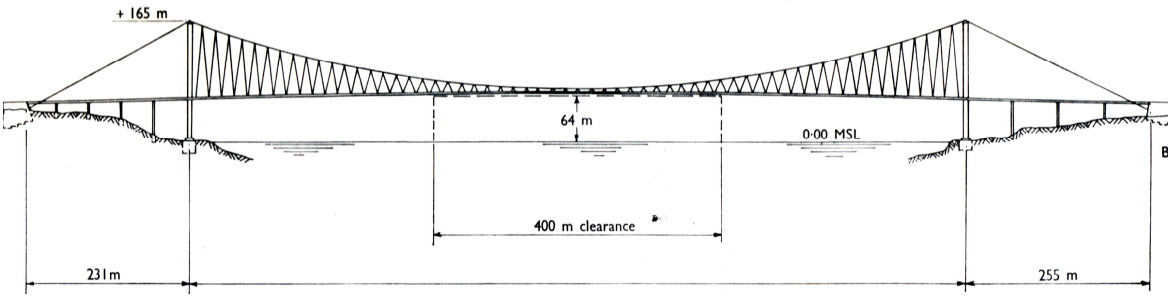

Figure 5.1. General configuration of the Bosphorus Bridge (Brown *et al*., 1976)

The main structural frame components of the bridge, including the box section stiffening girder for the deck and the box sections for the bridge towers and tower cross beams, were fabricated from high yield stress steel (with a yield stress of 354 MPa) or mild steel (with a yield stress of 252 MPa), with other mechanical properties similar to steel grade BS4360. The suspension cables and hangers were manufactured from high strength steel wires with an ultimate tensile stress of 1570 MPa. Geometrical properties of the deck stiffening girder, the bridge towers, the suspension cables, and the hangers are described briefly in the following paragraphs.

The box-type stiffening girder, constituting the deck of the bridge, is similar to that used in the Severn Bridge constructed in the United Kingdom in 1966. The girder forms a platform to transfer vertical loads to the hangers, and it has to have significant torsional stiffness for contributing to the overall aerodynamic stability of the deck. The box section involves an orthotropic top deck consisting of a 12 mm steel plate stiffened longitudinally with closed trapezoidal ribs that are spaced approximately 0.61 meters on center. As opposed to torsionally-flexible open ribs, this system provides a better transverse distribution of wheel loads, leading to reduced deformations in the deck plate. The bottom plate of the box section is a 9 mm plate with the longitudinal stiffener ribs spaced at 0.61 meters on center. The geometry of the box section is streamlined, with sharp edged wind noses on the sides to divide the air flow, and side plates with a modest inclination relative to the direction of the wind, for aerodynamic stability. The streamlined box section of the Bosphorus Bridge deck is illustrated in Figure 5.2.

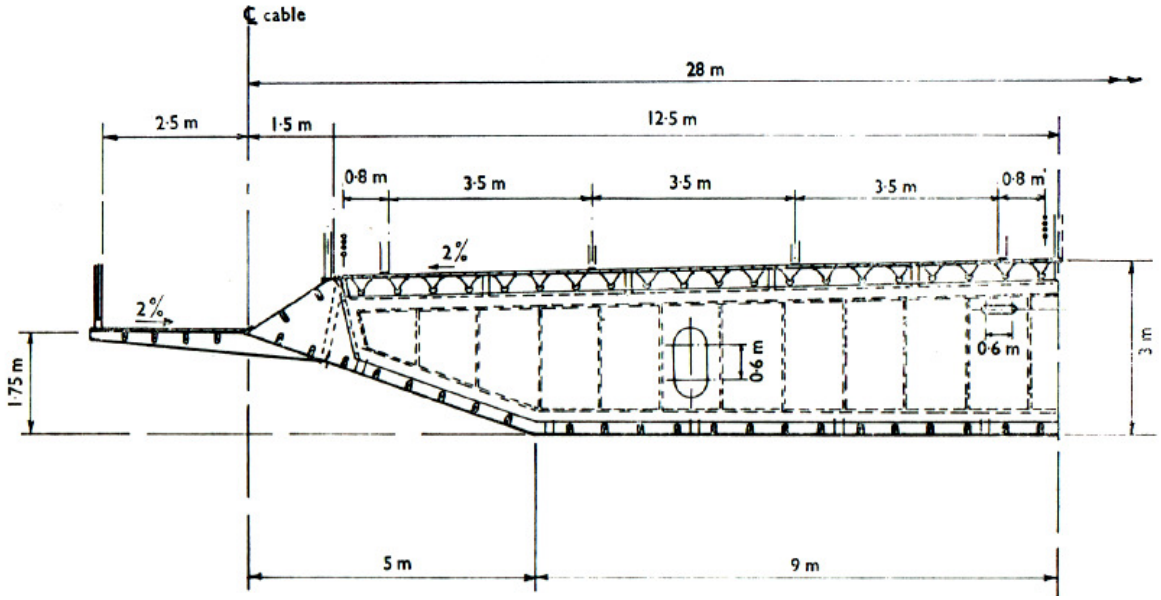

Figure 5.2. Streamlined cross section of the bridge deck (Brown *et al*., 1976)

The configuration of the towers follows the design details used by Freeman Fox and Partners for the Severn Bridge, but adjustments were made to suit the increased span and carriageway widths. Each tower leg is a rectangular box section 7 meters wide in the longitudinal direction of the bridge, and in the transverse direction tapers from 3 meters at the top to 5.2 meters at the bottom, as shown in Figure 5.3. The tower legs are stiffened longitudinally with L-shaped open ribs and incorporate diaphragm plates spaced 19.5 meters on center. Tower legs are connected in the transverse direction with three horizontal cross beams, which also have rectangular box sections. The plate thickness used for the tower leg sections varies from 35 mm at the base to 22 mm at the top of each tower. The general layout of the tower is shown in Figure 5.3.

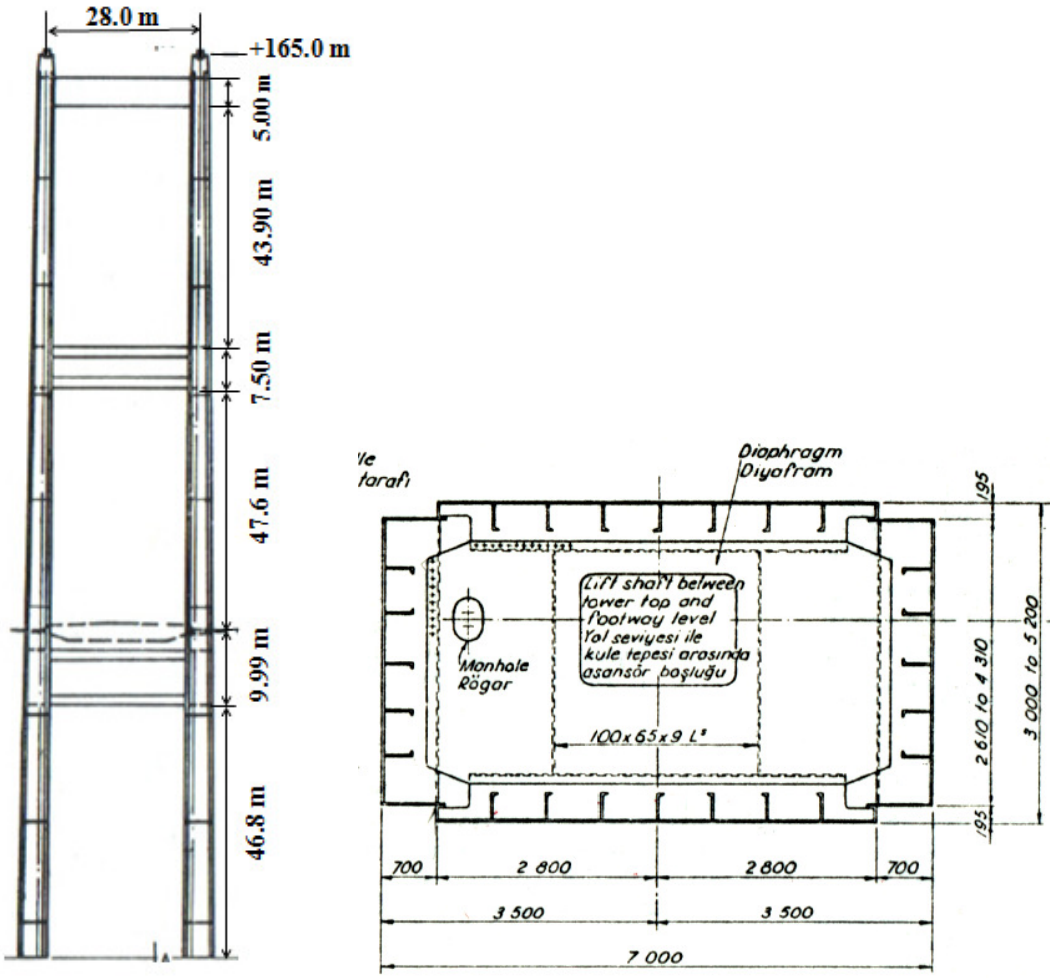

Figure 5.3. Bridge tower layout and bridge tower leg cross section at the base (Brown *et al*., 1976)

In the Bosphorus Bridge, the main span suspension cables consist of 19 strands, each containing 548 wires that are 5 mm in diameter. Side span suspension cables have 4 strands (each containing 192 wires) more than the main span cables. Suspension cables are of parallel-wire type and were formed by spinning. Configuration of the uncompacted suspension cables is shown in the Figure 5.4. The hanger cables are constructed of single spiral wire strands, and have a nominal diameter of 58 mm.

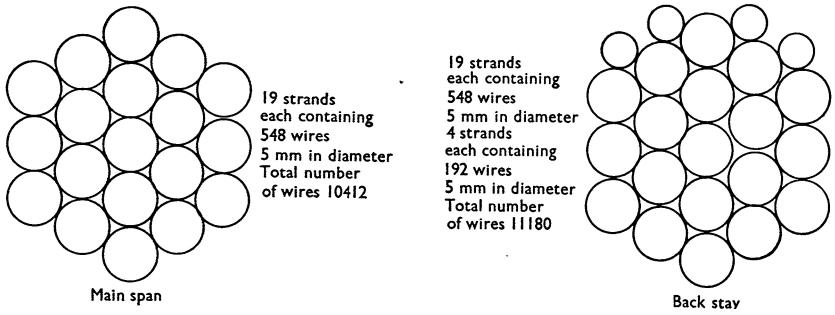

Figure 5.4. Configuration of of uncompacted suspension cables (Brown *et al.*, 1976)

5.3. Design Loading Conditions

The major types of loading considered in the analysis and design of the Bosphorus Bridge include dead load, superimposed dead load, traffic load, wind load, temperature effects, and earthquake loading. The design prioritiy for the bridge was for it to be lightweight structure, as well as an aerodynamic system to counter the large wind loads that suspension bridges are typically subjected to.

The total design dead load on the suspended structure, including weight of the deck, cable weights and the superimposed dead loads (all permanent loading due to weight of nonstructural components) was calculated as 147 kN/m in the design documents. The live load calculation is based on B.S.153, Part 3A (1954), and consists of equivalent uniformly distributed loads (E.U.D.L), knife edge loads (K.E.), and 45 units of the special "H.B." type vehicle. The number of lanes to be loaded and the length loading were chosen to create the maximum live load effects on the structural components.

The bridge site is not exposed to particularly high winds, and the available statistics had not indicated maximum wind speeds in excess of 35m/sec; however, the bridge was designed for a maximum wind speed of 45 m/sec at the level of the deck. The wind speed at the tower tops was extrapolated as 51 m/sec. The variation of wind speed with height was obtained from B.S.153 Part 3A. Temperature effects were considered in a range of ±28ºC. The bridge was designed for a peak ground acceleration of 0.125g, and basic horizontal and vertical seismic coefficients of 0.1 and 0.05 respectively, with modification factors corresponding to the predominant mode of vibration of each structural element

based on the recommendations given in the document “Specifications for Earthquake-Resistant Design of the Bosphorus Bridge”.

5.4. Structural Modeling

Within the scope of this preliminary case study, a three-dimensional structural model of the Bosphorus Bridge in Istanbul was created using the commercial structural analysis software SAP2000, and the model was used for conducting the static and dynamic analysis procedures described in Chapter 4. Information on the structural model is presented in the following subsections.

5.4.1. Material Properties

The material properties used in modeling of the main structural components of the Bosphorus Bridge, including the suspension cables, hangers, deck girder, towers, and tower cross beams are listed in Table 5.1. The modulus of elasticity values used in the model are based on the values reported in the design documents.

Table 5.1. Material properties

Structural Component	Yield Stress (MPa)	Modulus of Elasticity (MPa)	Unit Weight (kN/m^3)	Poisson’s Ratio
Suspension Cable	1570	$1.961x10^5$	76.97	0.3
Hanger		$1.618x10^5$		
Deck Girder	354	$2.059x10^5$		
Towers and Cross Beams		$2.00x10^5$		

5.4.2. Main Structural Components

In the structural model of the Bosphorus Bridge, the bridge towers, the tower cross beams and bridge deck were all represented by frame elements, whereas the suspension cables and hangers were represented by cable elements. The tower legs were assumed to be restrained against translation and rotation at the foundations. The hangers of the bridge were assumed vertical, instead of the actual inclined configuration, meaning that less

number of hangers was used in the model. However, the cross-sectional areas of the hanger elements were modified to create an approximately equal vertical stiffness contribution. A parabolic geometry was used for the elevation of the deck, based on the original vertical curve radius specified for the deck in the design drawings of the bridge. As such, the elevation difference between the deck mid-span and tower connections is 6.50 meters and the deck provides a 65 meter high clearance above the sea level across a width of 400 m. The size of the global model has 328 joints, 330 frame elements and 360 degrees of freedom. Illustrations of the structural model of the bridge are presented in Figures 5.5 to 5.7.

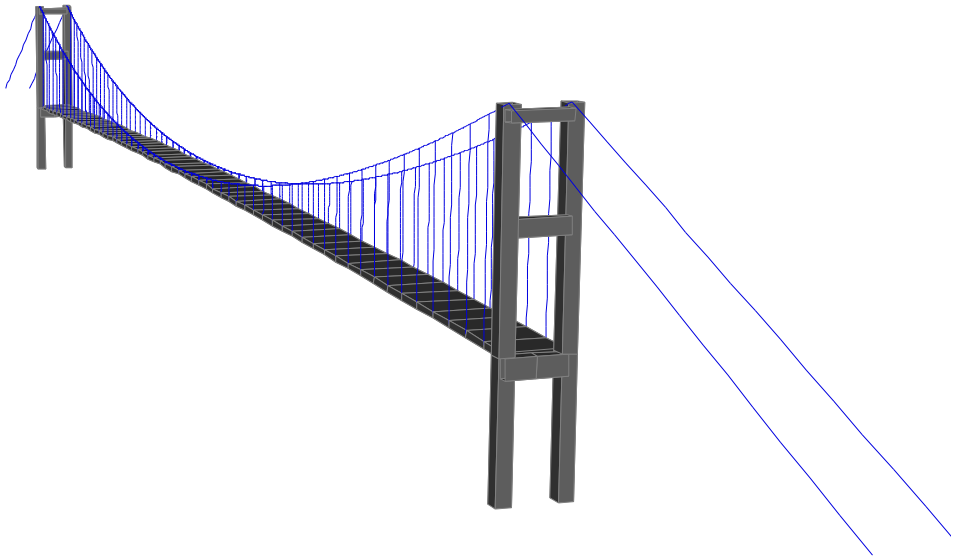

Figure 5.5. Three dimensional view of the structural model

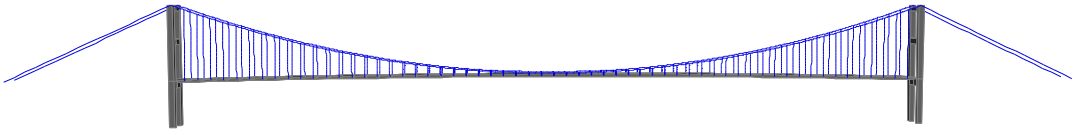

Figure 5.6. Two- dimensional view in *xz* plane

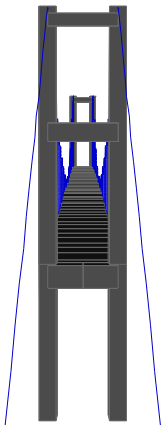

Figure 5.7. Two- dimensional view in yz plane

In the model, the taper on the tower leg cross-sections was ignored, and the tower leg cross sections were defined as square box sections with 7 m x 7 m outside dimensions and an average plate thickness of 3 mm. The three tower cross beams, which providing portal bracing action on the towers, were also defined as rectangular box sections with 3 mm plate thickness. The cross sectional properties of the tower legs and cross beams were calibrated, using the section modification factors in SAP2000, so that they are consistent with the values reported in the design documents of the bridge (Table 5.2).

Table 5.2. Cross sectional properties of the tower legs and tower cross beams

Section	Dimensions (m)	Area (m^2)	Torsional Constant, J (m^4)	Moment of inertia, I_{3-3} (m^4)	Moment of inertia, I_{2-2} (m^4)
Tower leg	7x7x0.03	0.8364	10.158	6.7723	6.7723
Tower upper cross beam	5x5x0.03	0.5964	3.6829	2.4554	2.4554
Tower middle cross beam	7.5x5x0.03	0.7464	6.6479	6.2442	3.3817
Tower lower cross beam	9.5x5x0.03	0.8664	9.2044	10.9323	4.1227

The suspended deck of the bridge was also defined as an equivalent rectangular box section. In order to account for its actual geometric configuration, as well as the stiffening effect of the trapezoidal ribs, appropriate section modifiers were used to calibrate the geometric properties of the deck cross section, so that they are consistent with the values

reported in the design documents of the bridge. The cross sectional properties of the suspended deck elements used in the structural model are listed in Table 5.3.

Table 5.3. Cross sectional properties of the deck

Section	Cross sectional area (m^2)	Torsional Constant, J (m^4) (polar moment of inertia)	Moment of inertia, I_{3-3} (m^4) (about transverse deck axis)	Moment of inertia, I_{2-2} (m^4) (about vertical deck axis)
Deck	0.851	3.35	1.238	63.61

The suspension cables and hangers in the structural model were defined using the cable element definition in SAP2000. Therefore, the cable elements in the model follow the stiffness formulation described in Section for 2.7. for catenary cable elements. The cross sectional properties of the suspension and hanger cable elements used in the structural model are listed in Table 5.4.

Table 5.4. Cross sectional areas of the cable elements

Cable	Diameter (m)	Area (m^2)
Suspension	0.53	0.221
Hanger	0.087	0.006

5.4.3. Connection Constraints and Releases

Consistently with numerous modeling studies in the literature on suspension bridges, the hanger cables in the structural model were connected to the deck at nodes located on the side boundaries of the deck cross section. These nodes were constrained to the longitudinal axis of the deck using the rigid body constraint conditions defined in SAP2000.

The deck was also connected to the lower cross beams of each tower, by again defining rigid body constraints between the mid-span node of each cross beam and the end node of the deck element. However, moment releases (about longitudinal, transverse, and vertical deck axis) were assigned to the end nodes of the deck at the cross beam

connections, so that the deck cannot transfer bending or torsional moments to the cross beams of the towers.

5.5. Structural Analysis Cases

The structural model of the Bosphorus Bridge was used for conducting the static and dynamic analysis procedures described in Chapter 4. The types of analyses performed using the bridge model include:

(i) Geometrically-nonlinear static analysis under dead load and determination of the initial equilibrium configuration,
(ii) Moving load analysis under vehicular loads,
(iii) Analysis for temperature effects,
(iv) Analysis under aerostatic wind forces,
(v) Analysis for dynamic earthquake effects, including:
- Free vibration (frequency) analysis,
- Nonlinear dynamic time history analysis,
- Linear response spectrum analysis.

The following subsections present the details of the analysis cases conducted, as well as comparison of the analysis results (under different load combinations) with selected results reported in the design calculations of the bridge.

5.5.1. Geometrically-Nonlinear Static Analysis under Dead Load

A set of geometrically-nonlinear static analyses were first conducted on the bridge model under self-weight induced and superimposed dead loads only. The objective of this initial nonlinear analysis was to achieve the initial (deformed) equilibrium configuration of the bridge under dead loads and cable pre-tensioning effects; that is, to determine the prestressed state of the structural components that will, together with the dead loads, will produce a deformed geometry that will be close to the intended geometrical configuration of the bridge. Reaching the initial equilibrium configuration of the bridge is essential in obtaining the stiffness properties of the cable elements for further analyses.

The total design dead load on the suspended structure, including weight of the deck, cable weights and the superimposed dead loads (all permanent loading due to weight of nonstructural components) was reported as 147 kN/m in the design documents of the bridge. In the structural model, the self weight of the suspension cables, hangers, and the deck were already considered in the analysis via the unit weight of the materials listed in Table 5.1. A superimposed dead load of only 25 kN/m was applied on the deck for considering the weight of the roadway surfacing, the parapets, the crash barriers, and other nonstructural components.

The initial (deformed) equilibrium configuration under dead loads was reached via adjusting the initial strain (prestrain) values in suspension cables and hangers, through a trial-and-error procedure. After performing an initial nonlinear analysis under dead load only (without any prestraining of the cables), the vertical deflection of the deck was obtained as -8.56 meters in the midspan. To reach the initial equilibrium configuration of the deck, that is to minimize the deck deflections and therefore the bending moments, prestrain values of -0.00275, -0.0027, and -0.00265 were selected as suitable values to be imposed on the side-span suspension cables, the main-span suspension cables, and the hangers, respectively. It is important to indicate that the prestrain values applied on the cables are not the actual mechanical (stress-compatible) strains in the cable elements, but rather the required change in the cable lengths (per unit length), which will allow the deformed geometry of the bridge deck under dead loads to resemble the intended geometrical configuration.

Significant results of the dead load analysis case are listed in Table 5.5. The values in the table indicate that while prestraining of the cable elements does not considerably increase the tension forces in the cables and therefore the axial load on the bridge piers, it significantly reduces the deflections and therefore the bending moments in the bridge deck and towers. Figure 5.8 illustrates the distribution of the bending moments in the bridge deck before and after prestraining of the cables.

Table 5.5. Dead load analysis case results

	Before pre-tensioning (dead load only)	After pre-tensioning (dead load and prestrains)
Maximum vertical displacement of the deck (at the midspan)	-8.56 m	0.10 m
Maximum tension in the main span suspension cables	108 636 kN	119 514 kN
Maximum bending moment in the deck about transverse axis	20 379 kN.m	-4268 kN.m
Axial load in the tower leg	-95 846 kN	-102 418 kN
Maximum bending moment in the tower leg	95 274 kN.m	6130 kN.m

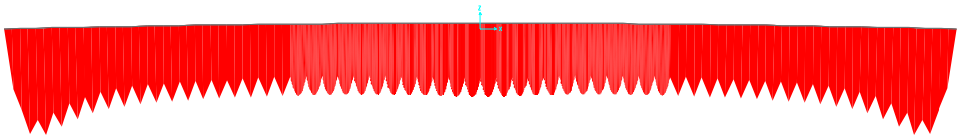

(i) Before pre-tensioning

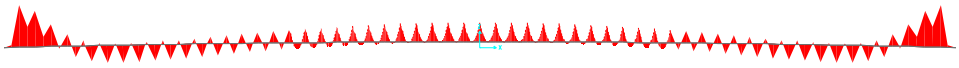

(ii) After pre-tensioning

Figure 5.8. Bending moment distributions in the bridge deck

After the initial equilibrium state of the bridge was reached at the end of the geometrically-nonlinear analysis under combined prestrain and dead load effects, the bridge model has attained its overall stiffness for further linear on nonlinear analysis under superimposed loads and dynamic actions.

5.5.2. Moving Load Analysis

For analysis of the bridge under vehicular live loads, the traffic live load specifications of the AAHTO-LRFD code described in Section 4.2 were used in the structural model. The “Bridge Analysis” tools in the SAP2000 program were used to determine the response of the bridge to the moving vehicle loads, as described in Section

4.3. Three traffic lanes, each with a 3.6 meter width, were defined in each direction of the bridge deck. The moving load analysis considered all possible permutations for the AASHTO-LRFD vehicle classes assigned, and provided the maximum and minimum displacements and internal forces, resulting from multiple and moving lane loads acting on the bridge deck. Significant results of the dead load analysis case are listed in Table 5.6.

Table 5.6. Moving live load analysis case results

	Under moving live load
Maximum vertical displacement of the deck (at the midspan)	-3.26 m
Maximum tension in the main span suspension cables	26 585 kN
Maximum bending moment in the deck about transverse axis	3620 kN.m
Axial load on the tower leg	20 150 kN
Maximum bending moment on the tower leg	23 956 kN.m

In 1973, just before the Bosphorus Bridge was opened for traffic, two lanes of the south carriageway and the center section of the north carriageway were loaded with a typical mixture of trucks, which were reported to create an average distributed load of 15.4 kN/m across the main span (Brown *et al*., 1976), and deflections of the bridge deck were measured (Fig. 5.9). In order to compare the results of the present structural model with the measured values, the same amount of distributed load was applied the model as a second type of live load case. The deflections obtained from the model are compared with the measured deflections in Table 5.7. Results of the analysis and the reported measurements are in agreement with each other, validating the stiffness properties of the model created.

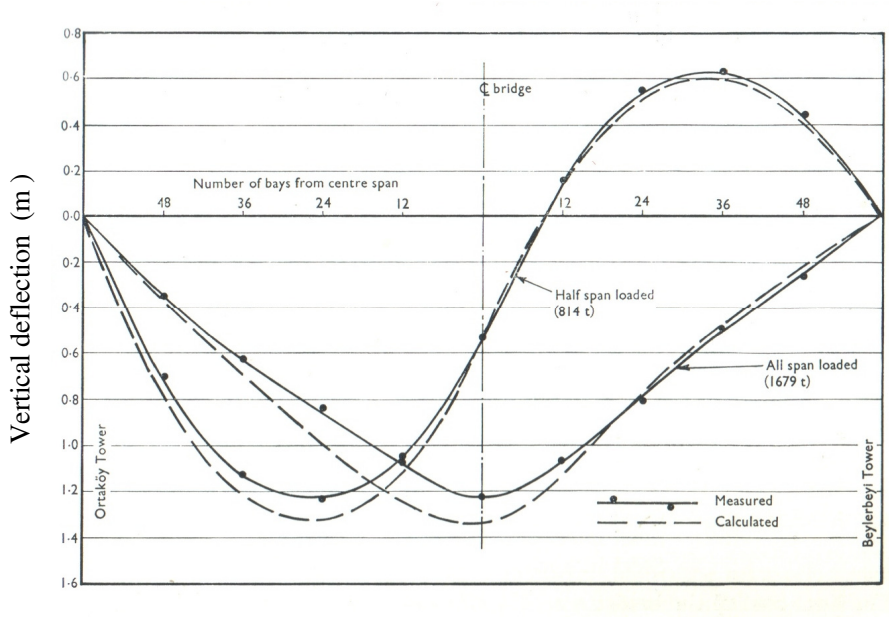

Figure 5.9. Deflection measurements for the Bosphorus Bridge (Brown *et al.*, 1976)

Table 5.7. Comparison of calculated and measured live load deflections of the deck

Deck Deflection	Analysis result	Measured deflection
Deflection at midspan (m)	-1.05	-1.25
Deflection at quarter-span (m)	-0.74	-0.76

5.5.3. Analysis under Temperature Effects

For analysis under temperature effects, a uniform temperature change of ± 30º was imposed on the bridge deck and towers, as well as the tower cross beams and cable elements. Additionally, temperature gradients were considered in the two transverse directions for the deck, tower, and tower cross beams elements, as described in Chapter 4.

Significant results of the temperature load analysis case are listed in Table 5.8, for the uniform temperature change and the transverse temperature gradient conditions. For the uniform temperature change applied on all components, the maximum deflection and bending moment in the deck develops at the connection with the longest hanger. For the temperature gradient in the transverse direction of the deck (temperature gradient 3), the

maximum deflection of the deck occurs at the midspan, where the maximum bending moment also develops.

Table 5.8. Temperature load analysis case results

Deck	Deflection at midspan (m)	Deflection at the longest hanger connection (m)	Bending moment at midspan (kN.m)	Bending moment at the longest hanger connection (kN.m)
Uniform temperature change	0.166	-0.180	280	-3757
Temperature gradient 2	-0.033	0.045	29 832	11315
Temperature gradient 3	-0.694	-0.065	129 011	6017

5.5.4. Wind Load Analysis

For analysis under aerostatic wind forces, the equivalent static wind loads acting on the bridge towers were calculated according to the ACI 307 specifications (ref) described in Sections 4.5 and 4.6. The formulations for the determination of the design wind moment M_z, the dynamic wind load w_{dz}, and the gust factor G_o were provided in Section 4.6. Since calculation of the gust factor (G_o) is based on the first fundamental period of vibration of the towers in the wind directions, the periods of vibration of the entire bridge, corresponding to the first swaying vibration mode of the towers, were first calculated using a free-vibration analysis, as 0.87 sec and 2.17 sec in the longitudinal and transverse directions of the bridge, respectively. The calculated wind load profiles in acting on the bridge tower legs in the longitudinal transverse bridge directions are illustrated in Figures 5.10 and 5.11.

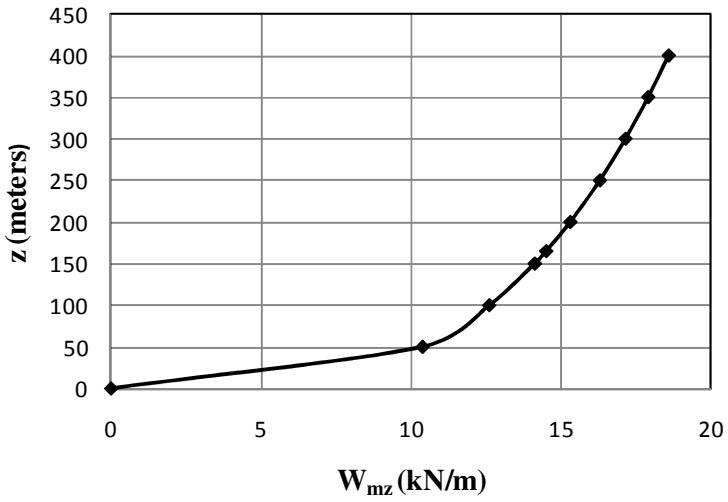

(i) Mean load profile

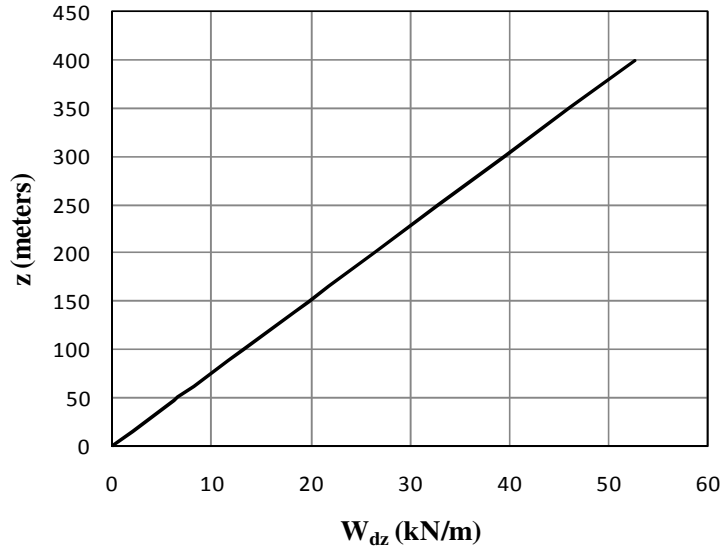

(ii) Dynamic load profile

Figure 5.10. Wind load profiles on the bridge tower legs in the longitudinal bridge direction

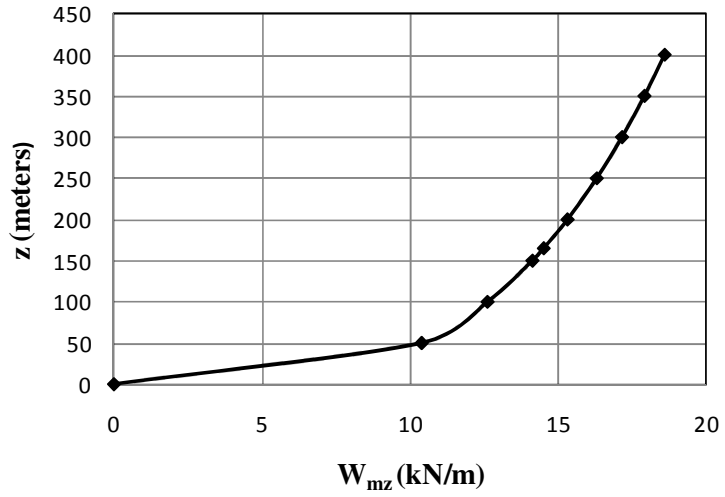

(i) Mean load profile

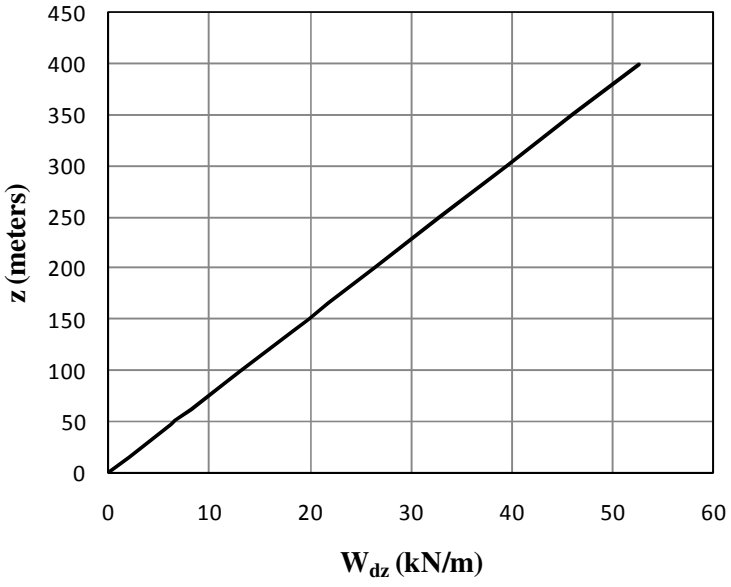

(ii) Dynamic load profile

Figure 5.11. Wind load profiles on the bridge tower legs in the transverse bridge direction

The aerostatic wind forces acting per unit length of the bridge deck were calculated using the drag force, lift force and pitch moment formulations described in Chapter 4, Section 4.5. The aerostatic coefficients (C_y, C_z and C_m) used in the calculations for the case of horizontal (0°) wind incidence are listed in Table 5.9. Since the Bosphorus Bridge has a streamlined deck cross section like Messina Strait Bridge and the Normandie Bridge, the aerostatic coefficient values used in the analysis were taken as comparable values to those reported in Table 4.3 for the two bridges.

Table 5.9. Aerostatic coefficients used for calculating wind loads on the deck

C_y	C_z	C_m
0.07	-0.24	0.015

The aerostatic drag force, lift force and pitch moment acting per unit length of the deck were calculated accordingly, for the case of horizontal (α=0°) wind incidence. The values used in the analysis and are listed in Table 5.10.

Table 5.10. Aerostatic wind loads acting on the deck

Drag force, $F_y(\alpha)$	2.55 kN/m
Lift force, $F_z(\alpha)$	81.97 kN/m
Pitch moment $M(\alpha)$	145.97 kN.m/m

Wind load analyses of the bridge model were conducted under the wind loads acting on the deck and the towers, calculated as described above. Displacements obtained at the end of the analyses at critical locations of the bridge are presented in Tables 5.11 to 5.13.

Table 5.11 lists the deck midspan displacements under the wind loads applied on the deck. The values reveal how the predominant direction of the displacement is related to either the drag (transverse load), the lift (vertical load), or the moment (torque) component of the wind load. Displacements under the combined effect of the wind load components are also given in the table. The displacements at the quarter-span of the deck are listed in Table 5.12.

Table 5.11. Deck midspan displacements under wind loads on deck

	Wind load case on deck	Transverse deflection (m)	Vertical deflection (m)	Twist angle (rad)
Deck midspan	Wind drag	**1.0991**	0.0000	0.0011
	Wind lift	0.0000	**1.1107**	0.0000
	Wind moment	0.0334	0.0000	**0.0122**
	Combined	1.1325	1.1107	0.0134

Table 5.12. Deck quarter-span displacements under wind loads on deck

Deck quarter-span	Wind load case on deck	Transverse deflection (m)	Vertical deflection (m)	Twist angle (rad)
	Wind drag	**0.8116**	0.0000	0.0010
	Wind lift	0.0000	**0.8112**	0.0000
	Wind moment	0.0257	0.0000	**0.0102**
	Combined	0.8373	0.8112	0.0112

Table 5.13 shows the displacements calculated at the top of the towers under the wind loads applied on the towers. The results indicate that the tower displacements are significantly higher in the transverse direction of the bridge, since the top of the towers are restrained by the suspension cables in the longitudinal bridge direction.

Table 5.13. Tower displacements under wind loads on towers

Tower top	Wind load case on tower	Deflection in longitudinal bridge direction (m)	Deflection in transverse bridge direction (m)
	Longitudinal bridge direction	**0.0118**	0.0000
	Transverse bridge direction	0.0015	**0.1058**

Other significant results of the wind load analysis case, under combined wind loads acting on both the deck and towers of the bridge, are listed in Table 5.14.

Table 5.14. Wind load analysis case results

	Under combined wind load (acting on both deck and towers)
Maximum vertical displacement of the deck (at the midspan)	1.12 m
Maximum tension in the main span suspension cables	10 980 kN
Maximum bending moment in the deck about transverse axis	10 124 kN.m
Maximum bending moment in the deck about vertical axis	4800 kN.m
Axial load on the tower leg	24 000 kN

Table 5.14. Wind load analysis case results (cont'd.)

	Under combined wind load (acting on both deck and towers)
Maximum bending moment on the tower leg in longitudinal bridge direction	36 760 kN.m
Maximum bending moment on the tower leg in transverse bridge direction	80 150 kN.m

5.5.5. Free Vibration (Modal) Analysis

Prior to commencing the dynamic analysis of the structural model under dynamic earthquake actions, a free vibration analysis (described in Section 4.7.1) was performed for determining the vibration characteristics of the structure. The free vibration analysis was conducted using the modal analysis case defined in the program SAP2000, in order to calculate the natural frequencies, mode shapes, and mass participation factors (effective modal mass values) of the model, associated with the first 200 modes of vibration of the structure. The cyclic frequency values calculated first 10 modes of vibration of the bridge are listed in Table 5.15, together with the results of previous analytical studies on the Bosphorus Bridge by Tezcan et al. (1974), Brownjohn et al. (1989), Koşar (2003), and Erdik et al. (1989). A good agreement is observed between the calculated frequency values and the results of previous studies.

Table 5.15. Calculated modal cyclic frequencies of the bridge

Vibration Mode	Calculated frequency (Hz)	Frequency by Tezcan et al. (Hz)	Frequency by Brownjohn et al. (Hz)	Frequency by Koşar (Hz)	Frequency by Erdik et al. (Hz)
1	0.068	0.064	0.073	0.068	0.072
2	0.108	0.117	0.126	0.125	0.144
3	0.153	0.146	0.165	0.189	0.202
4	0.157	0.173	0.180	0.222	0.225
5	0.193	0.216	0.218	0.273	0.323
6	0.211	0.221	0.225	0.277	0.340
7	0.248	0.285	0.278	0.293	0.365
8	0.281	0.291	0.284	0.293	0.385
9	0.294	0.295	0.294	0.297	-
10	0.296	0.316	0.301	0.303	-

The mode shapes obtained for the first six modes of vibration of the bridge are shown in Figures 5.12 to 5.17.

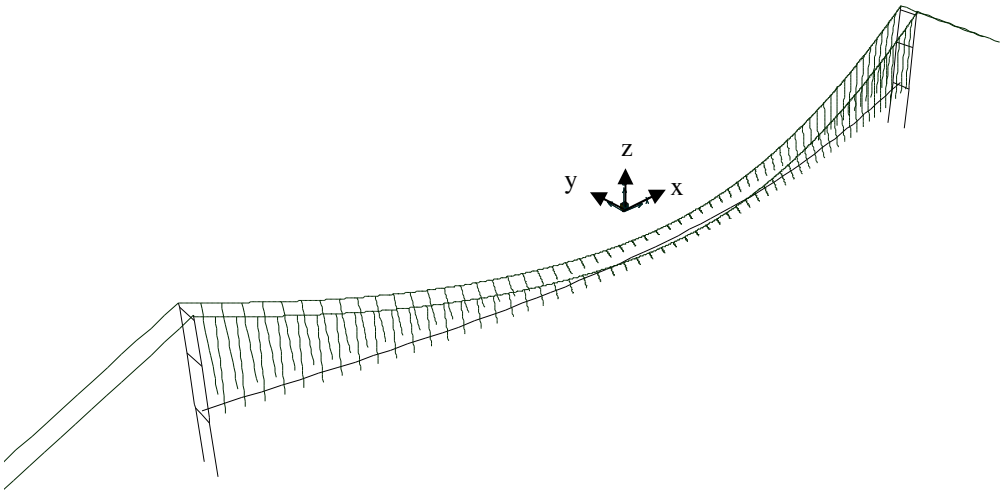

Figure 5.12. Mode shape for the first mode of vibration (T=14.71 sec)

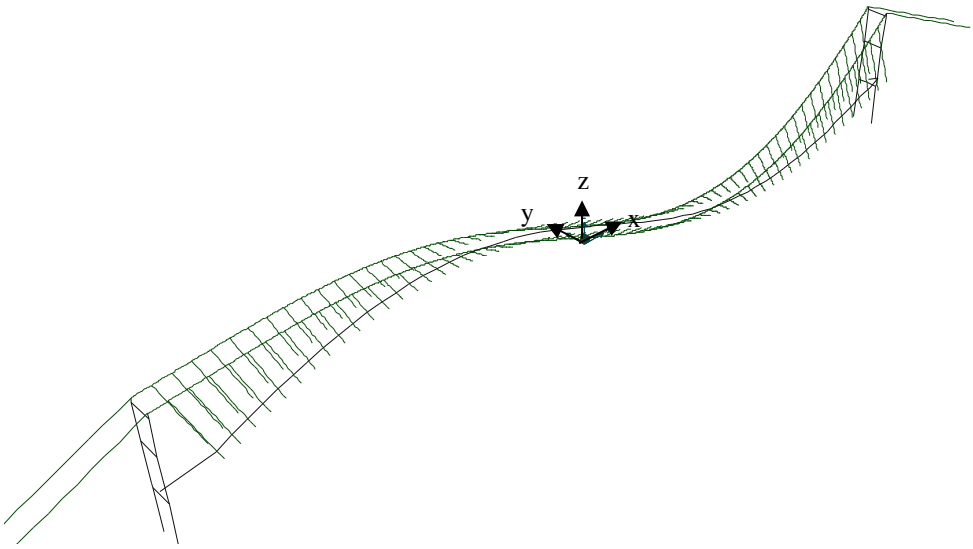

Figure 5.13. Mode shape for the second mode of vibration (T=9.28 sec)

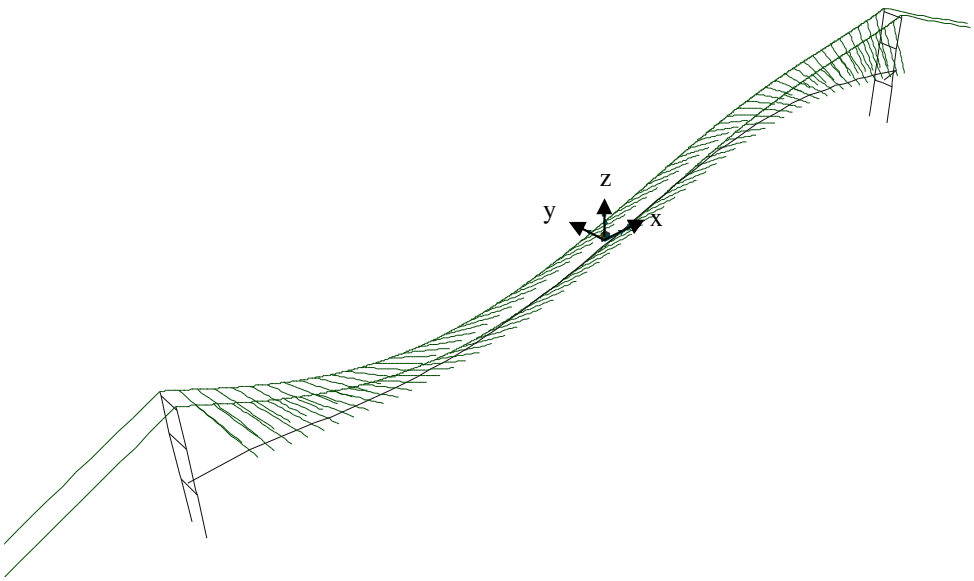

Figure 5.14. Mode shape for the third mode of vibration (T=6.53 sec)

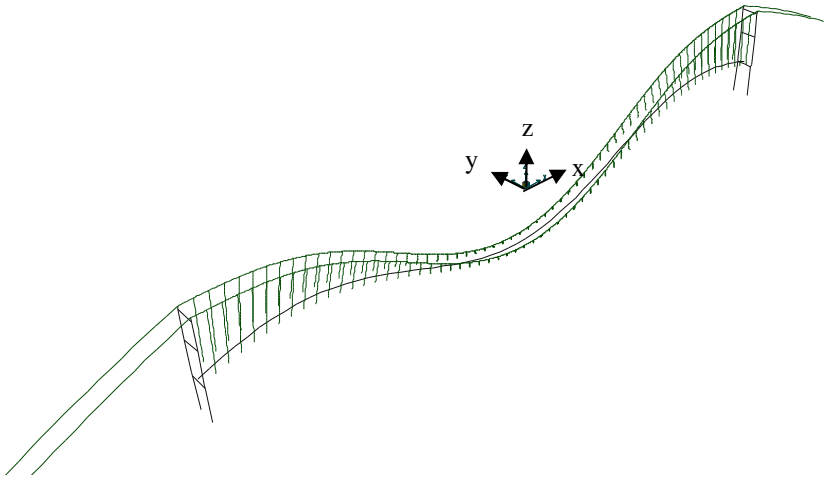

Figure 5.15. Mode shape for the fourth mode of vibration (T=6.37 sec)

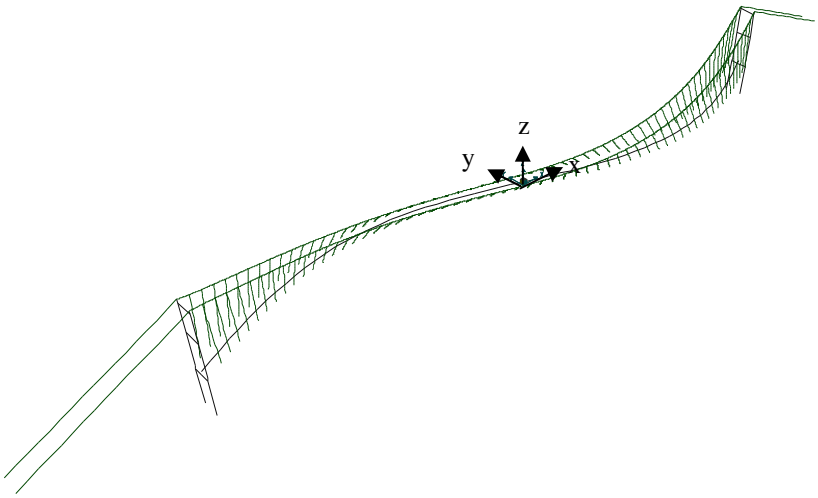

Figure 5.16. Mode shape for the fifth mode of vibration (T=5.18 sec)

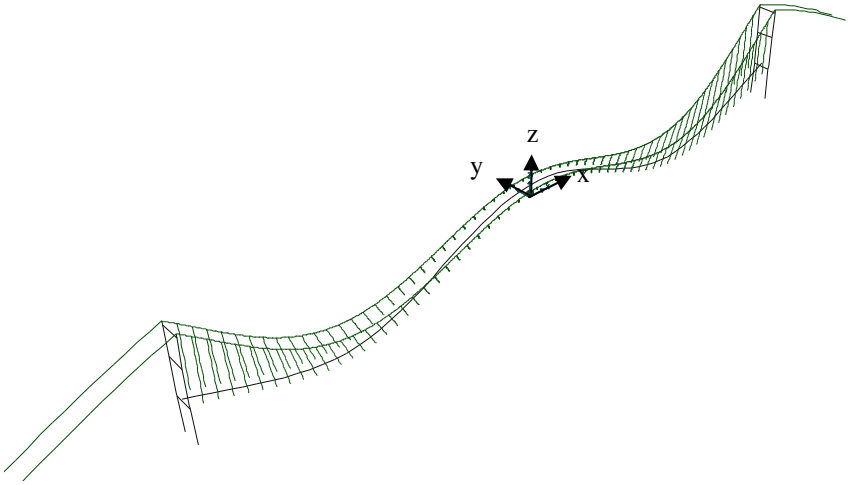

Figure 5.17. Mode shape for the sixth mode of vibration (T=4.74 sec)

The first 19 modes of vibration with significant modal mass participation factors (normalized effective modal masses) are listed in Table 5.16, along with their dominant direction of motion and respective modal mass participation ratio (MPR). The selected modes in the table are those with a significant MPR value in any single direction. In the table, U_X, U_Y, and U_Z represent motion in longitudinal bridge direction, transverse bridge direction, and vertical direction, respectively, and R_x represents rotation about the longitudinal direction of the bridge, which may be interpreted as a twisting rotation on the deck.

The MPR values provide a measure of how important a particular mode of vibration is for the overall response of the bridge to acceleration-induced loads in each global direction, and help ensure that a significant and required number of vibration modes are included in the earthquake response analysis of the structure. The sum of the MPR values for all of the 200 modes considered in the analysis are listed at the bottom of Table 5.16, and cumulative MPR values are plotted with respect to the vibration mode number in Figure 5.18. The cumulative percentages indicate that the accumulated mass participation ratio for the first 200 modes of vibration is almost 100% in longitudinal and transverse translational directions of the bridge, as well as in the rotational direction about the longitudinal bridge axis. On the other hand, the accumulated mass participation ratio for is only 74% in the vertical direction, indicating that more modes of vibration need to be considered in the dynamic analysis of the structure under vertical accelerations. Analysis of the bridge under vertical ground accelerations is beyond the scope of this case study; therefore, 200 modes were found to sufficient for analyzing the bridge under horizontal earthquake accelerations.

Table 5.16. Vibration modes with the highest 19 mass participation ratios

No.	Mode	Period	Mode shape description	Mass Participation Ratios (%)			
				U_X	U_Y	U_Z	R_X
1	1	14.71	U_Y (deck transverse)	1.60E-11	**61.83**	7.00E-11	**4.6528**
2	2	9.28	U_X+U_Z	**23.072**	3.00E-11	3.90E-09	8.00E-12
3	3	6.53	U_X	**33.8306**	2.00E-12	3.10E-07	2.00E-11
4	4	6.37	U_Z (deck vertical)	9.10E-07	3.00E-11	**17.3806**	7.00E-14
5	6	4.74	U_Z	6.60E-09	4.00E-11	**45.901**	8.00E-11
6	10	3.38	U_Y (deck torsional)	1.10E-12	**2.6334**	1.90E-11	**20.202**
7	12	3.08	U_Z	3.50E-10	7.00E-12	**5.3428**	1.00E-10
8	13	2.59	U_Y	1.40E-13	**12.056**	4.80E-11	**9.0095**
9	19	2.05	U_Z (tower sway)	7.60E-11	4.00E-10	**1.6828**	1.00E-08
10	20	2.01	U_Y	6.80E-12	**0.2856**	4.60E-10	**10.287**
11	22	1.77	U_Y	1.10E-11	**13.286**	7.60E-11	**31.977**
12	26	1.46	U_Z+U_Y	1.10E-11	**3.0971**	3.30E-10	**8.5422**
13	27	1.4	U_Z	2.00E-11	2.00E-09	**0.8568**	3.00E-09
14	35	1.08	U_Z	2.00E-11	3.00E-11	**0.5305**	4.00E-14
15	39	0.97	U_X	**29.9035**	3.00E-14	8.20E-13	3.00E-13
16	43	0.94	U_Y	1.30E-13	0.249	1.60E-14	4.00E-05
17	44	0.87	U_Y	3.40E-12	**1.1573**	8.70E-13	**2.5214**
18	54	0.71	U_X	**10.7137**	7.00E-13	7.20E-11	5.00E-11
19	66	0.55	U_Y	8.30E-11	**2.6439**	5.00E-12	**3.7478**
SUM (over all 200 modes considered)				99.9	99.9	73.9	98.7

Note: U_X: longitudinal motion, U_Y: transverse motion, U_Z: vertical motion,
R_X: rotations about the longitudinal bridge axis.

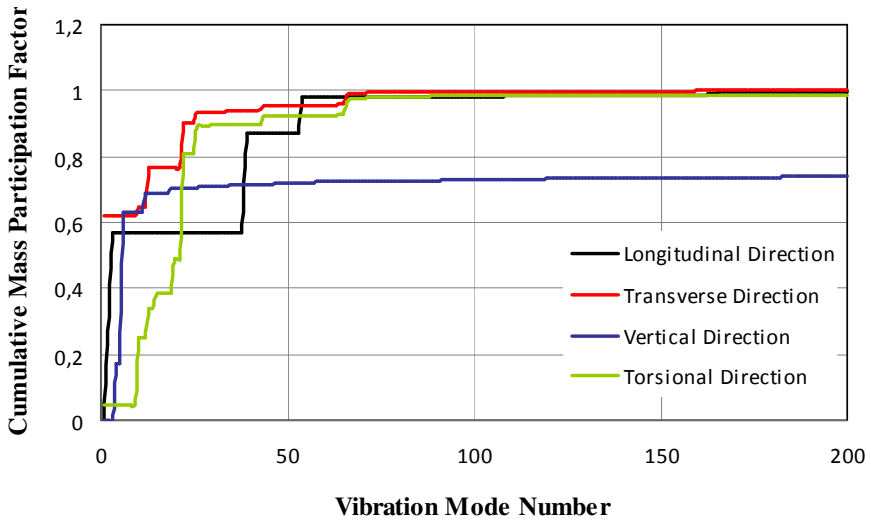

Figure 5.18. Increase in cumulative mass participation factor with the number of modes

5.5.6. Time–History Response Analysis of Earthquake Effects

As a first method for determining the response of the bridge to dynamic earthquake actions, a set of geometrically-nonlinear dynamic time-history analyses were conducted by applying a strong ground acceleration record on the bridge model. This was done not only to be able to observe the nonlinear dynamic behavior of the bridge under a particular and real ground motion time history, but also to be able to compare the results of the nonlinear time-history analysis with the results of response spectrum (modal superposition) analysis method. The results of the nonlinear time history analysis were obtained in terms of both displacement time histories at critical locations of the bridge, and internal force time histories at critical sections on the bridge deck and the bridge towers.

The North-South component of the horizontal ground acceleration time history recorded at the Imperial Valley Irrigation District substation in El Centro, California, during the May 19, 1940 Imperial Valley earthquake was used in the nonlinear time history analysis of the bridge model. The El Centro ground acceleration record has also been used extensively in previous earthquake engineering studies. The May 19, 1940 earthquake was recorded as the strongest earthquake to hit Imperial Valley, California. The moment magnitude of the earthquake was estimated to be M_W = 6.95, and the peak ground acceleration recorded at the El Centro station in the North-South direction was 0.32g. The

El Centro ground acceleration record was downloaded from the PEER NGA (2005) strong motion database, and is shown in Figure 5.19. In this study, El-Centro ground acceleration record was selected as an illustrative example in order to be able to execute the dynamic seismic response of the long span bridges.

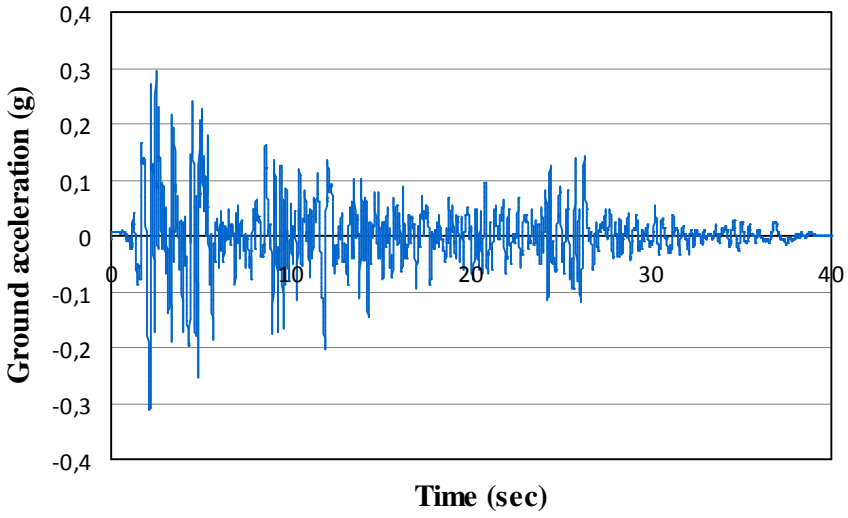

Figure 5.19. El Centro North-South ground acceleration time history recorded during the 1940 Imperial Valley earthquake

In the nonlinear time-history analysis, the earthquake excitation was applied as inertial loading on the entire structural model of the bridge. The El Centro acceleration record was applied in both the longitudinal and the transverse directions of the bridge. Vertical ground accelerations were not considered in the analysis. Geometrical nonlinearity in the cable elements of the model was considered in the analysis, as well as P-Delta and large displacement effects. Mass and stiffness proportional Rayleigh damping was used to assign the damping properties of the model, by specifying critical damping ratio values of 2% corresponding to natural period values of 14.7 sec and 0.2 sec. Variation of the damping ratio values used in the structural model with the natural cyclic frequencies of the model is plotted in Fig. 5.20.

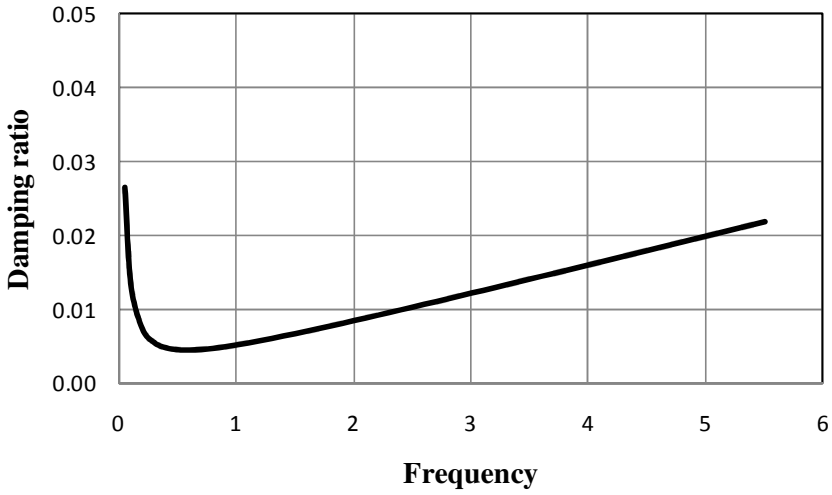

Figure 5.20. Variation of the damping ratio with natural cyclic frequency in the structural model

The results of the nonlinear time history analysis provided displacement time histories at critical locations on the bridge and time histories of internal forces (shear forces, bending moments, axial force, torque) at critical sections on the bridge deck and the bridge towers. Maximum values were used in evaluation of the bridge response and comparison with response spectrum analysis results. The displacement time histories calculated at the midspan of the bridge deck and the top of the bridge towers in longitudinal and transverse directions of the bridge, are presented in Figures 5.21 to 5.24, for illustration purposes.

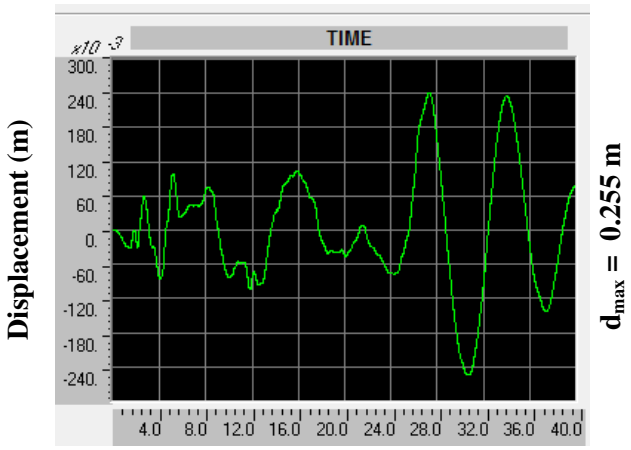

Figure 5.21. Nonlinear time-history analysis results: deck midspan displacement in longitudinal bridge direction

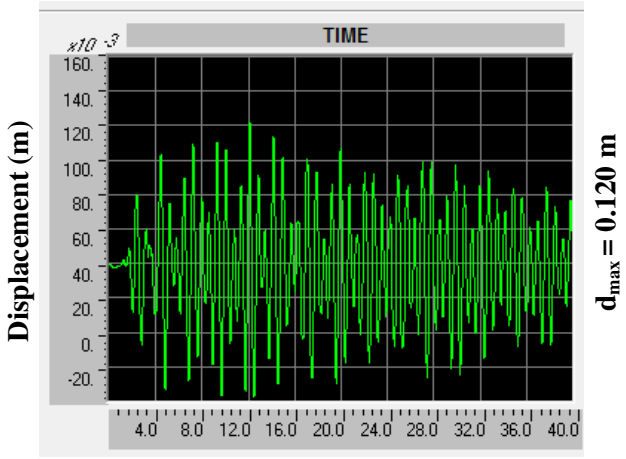

Figure 5.22. Nonlinear time-history analysis results: tower top displacement in longitudinal bridge direction

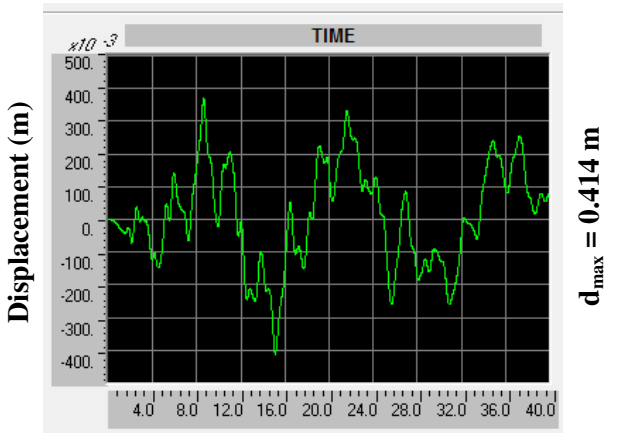

Figure 5.23. Nonlinear time history analysis results: deck midspan displacement in transverse bridge direction

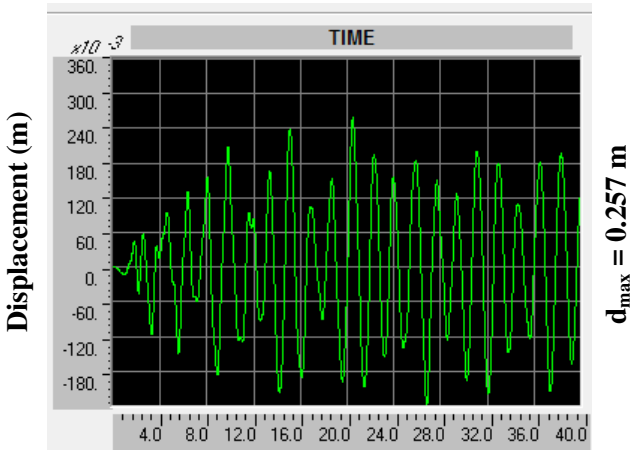

Figure 5.24. Nonlinear time history analysis results: tower top displacement in transverse bridge direction

5.5.7. Earthquake Response Spectrum Analysis

As a second method for determining the response of the bridge to dynamic earthquake actions, a set of response spectrum analyses were also conducted in the longitudinal and transverse directions of the bridge, to be able to compare the results of the nonlinear time-history analysis with the results of response spectrum analysis. The results of the response analysis were obtained in terms of both maximum displacement at critical locations of the bridge, and maximum internal forces at critical sections on the bridge deck and the bridge towers.

For the analysis, response spectrum (spectral pseudo-acceleration versus natural period) functions were applied on the structural model, separately in the longitudinal and transverse directions of the bridge. The complete quadratic combination (CQC) method of modal superposition was used, to consider the statistical coupling between closely-spaced vibration modes in the response of the structure, as described in Section 4.7.2. A critical damping ratio value of 2% was assigned to all modes of vibration. The response spectrum functions applied on the model in the longitudinal and transverse bridge directions were generated for the El Centro ground acceleration time history data described in the previous section. This was done to be able to directly compare the results of the nonlinear time history analysis with the results of the linear response spectrum analysis, for the same ground excitation. The spectral pseudo acceleration response spectrum for the El Centro ground acceleration record and 2% critical damping ratio, which was used in the analysis, is illustrated in Figure 5.25.

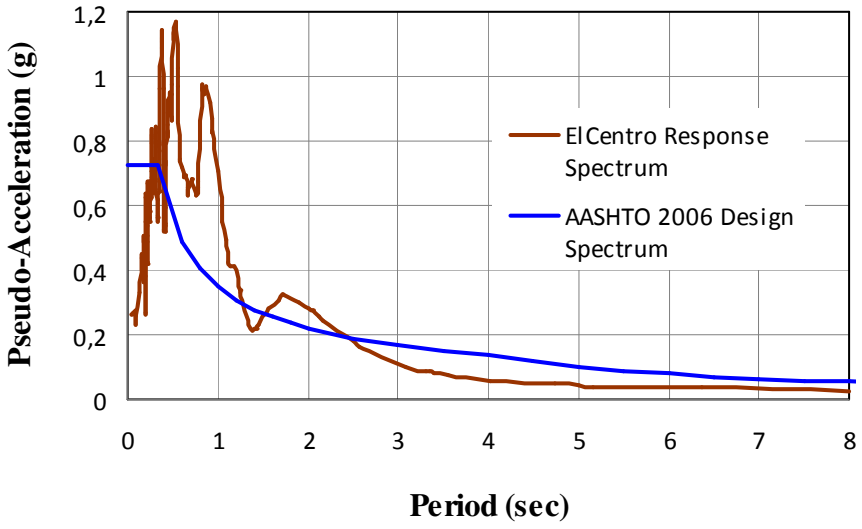

Figure 5.25. Pseudo acceleration response spectrum for the El Centro ground motion record (for 2% damping) and the AASHTO 2006 design spectrum

The AASHTO 2006 design response spectrum function, which is readily available in SAP2000, was also used as an alternative response spectrum analysis procedure. The required coefficients to generate the AASHTO design spectrum were selected according to relevant specifications of the AASHTO-LRFD 2007 code. These coefficients include the acceleration coefficient *A*, which represents the peak ground acceleration expected at the site in terms of *g*, depending on the seismic zone (AASHTO-LRFD Section 3, Article 3.10.4), and the site coefficient *S*, which is related to the soil profile type at the site.

The acceleration coefficients and site coefficients defined in AASHTO-LRFD 2007 are listed in Tables 5.17 and 5.18. For the present analysis, an acceleration coefficient of 0.29g was selected (AASHTO-LRFD Section 3, Article 3.10.4), which is comparable with the 0.32g peak ground acceleration value of the El Centro ground motion. For the site coefficient, soil profile II was selected, which is defined for stiff cohesive or deep cohesionless soils (stable deposits of sands, gravels, or stiff clays) over the rock, with the soil depth exceeding 60 meters. It is stated in AASHTO-LRFD that in locations where the soil properties are not known in sufficient detail, the site coefficient for soil profile type II shall be used (AASHTO-LRFD Section 3, Article 3.10.5.1). The ASSHTO design spectrum used for the analysis was shown in Figure 5.25.

Table 5.17. Acceleration coefficients defined in AASHTO-LRFD (AASHTO, 2007)

Acceleration Coefficient, A (g)	Seismic Zone
$A \leq 0.09$	1
$0.09 < A \leq 0.19$	2
$0.19 < A \leq 0.29$	3
$0.29 < A$	4

Table 5.18. Site coefficients defined in AASHTO-LRFD (AASHTO, 2007)

Site Coefficient	Soil Profile Type			
	I	II	III	IV
S	1.0	1.2	1.5	2.0

5.5.8. Comparison of Nonlinear Time History and Response Spectrum Analysis Results

The results of the nonlinear time history analysis and the response spectrum analyses are compared in Table 5.19. Values obtained for the maximum displacements at the midspan and quarter-span of the deck, maximum displacements at the top of the towers, maximum bending moments in the deck and the tower legs, and maximum axial forces in the suspension cables are compared in the table.

Table 5.19. Comparison of nonlinear time history and response spectrum analysis results

Response	Direction	El Centro nonlinear time history analysis	El Centro response spectrum analysis	AASHTO response spectrum analysis
Deck mid-span diplacement (m)	longitudinal	0.255	0.287	0.603
	transverse	0.414	0.987	2.85
Deck quarter-span displacement (m)	longitudinal	0.253	0.288	0.605
	transverse	0.300	0.716	2.05

Table 5.19. Comparison of nonlinear time history and response spectrum analysis results (cont'd.)

Response	Direction	El Centro nonlinear time history analysis	El Centro response spectrum analysis	AASHTO response spectrum analysis
Displacement at top of tower (m)	longitudinal	0.080	0.060	0.034
	transverse	0.257	0.187	0.179
Maximum moment in the deck (kN.m)	about transverse deck axis	9715	3790	1770
	about vertical deck axis	286 540	201 030	335 900
Maximum moment in the tower (kN.m)	in longitudinal bridge direction	256 491	257 983	123 910
	in transverse bridge direction	144 830	108 000	95 040
Maximum additional tension in the suspension cable	longitudinal EQ action	10 438	8820	5040
	transverse EQ action	1460	310	630

The comparisons indicate that the results are generally comparable, although the AASHTO response spectrum analysis may provide displacements that are significantly larger than the results of the ground motion time history analysis or ground motion response spectrum analysis. This is expected, since the AASHTO spectrum is a design spectrum, and involves a certain amount of conservatism in predicting the characteristics of a critical design ground motion to be expected at a site. For example, the pseudo-accelerations predicted by the AASHTO spectrum are significantly larger than the El Centro Spectrum in the large period range, which corresponds to the displacement-sensitive region of the response (Figure 5.25) and governs the displacements in the structure. Therefore, it is natural that the AASHTO spectrum significantly overestimates the transverse displacement of the deck and therefore the bending moment in the deck

about the vertical axis, since the natural vibration of the transverse displacement mode of the deck is very large (14.71 sec for vibration mode 1, as indicated in Table 5.16).

Comparing the results of the time history analysis and the response spectrum analysis for the El Centro ground motion, the discrepancies emphasizes that the response spectrum analysis method is only an approximate method, and its applicability for such a suspension bridge system may be questionable. In the case of a complex, three dimensional structures, with numerous closely-spaced modes, such as suspension bridges, great caution should be exercised in employing the response spectrum method. The results of the time history analysis presented in this study are considered much more reliable than the results of the response spectrum analysis.

5.5.9. Load Combinations

In the analysis of the Bosphorus Bridge under combined loading, instead of using the AASHO-LRFD (2007) load factors and limit states described in Section 4.8.1, the load combinations used in the original design calculations of the bridge were considered, to be able to compare the results of the present analysis with the analysis reported in the design documents for different load combinations.

The load combinations selected for the analysis of the bridge, which include dead load, live load, wind load, temperature load, and earthquake actions, are listed in Table 5.20.

Table 5.20. Load combinations used in the analysis of the Bosphorus Bridge

Load Combination	Loading
1	Dead + Live
2(a)	Dead + Live + Transverse Wind +Temperature
2(b)	Dead + Live + Longitudinal Wind + Temperature
4(a)	Dead + Transverse Earthquake + ½ Live + Temperature
4(b)	Dead + Longitudinal Earthquake + ½ Live + Temperature

5.5.10. Comparison of Analysis Results with Design Documents

The internal forces developing in critical structural members, obtained from the analysis results reported in the design calculations of the bridge, where available. This was done for evaluating the validity of the structural model created, as well as the validity of the load assignments and the analysis procedures used.

A comparison of the analysis results and the reported values for the maximum tensile force on the suspension cables is provided in Table 5.21. The comparisons indicate good agreement between the reported values and the results of the present analysis.

Table 5.21. Analysis results and reported values for the maximum tensile force on the suspension cables

Loading type or load combination	Maximum tensile force on the suspension cables (kN)	
	Reported value (RV)	Analysis result (AR)
Dead Load	117 209	119 585
Live Load	18 540	11 970
Temperature	1472	1447
Combination 1	147 590	133 260
Combination 2(a)	128 442	135 770
Combination 2(b)	150 603	150 937
Combination 4(a)	140 322	139 145
Combination 4(b)	138 144	129 855

A comparison of the analysis results and the reported values for the axial force, shear forces, and bending moments at the base of the tower legs is provided in Table 5.22. Again, there is good agreement between the reported values and the results of the present analysis. However, under load combinations 4(a) and 4(b), both of which include earthquake loading, the analysis results for the internal shear forces and bending moments in the direction of the earthquake loading are consistently larger than the reported values. This is consistent because the present nonlinear time history analyses were performed for a

ground motion with a peak ground acceleration of 0.32g, whereas a peak ground acceleration value of only 0.125 g was considered in the design calculations of the bridge.

Table 5.22. Analysis results and reported values for the internal forces at the base of the tower legs

LC	Axial force (kN)		Transverse bending moment (kN.m)		Transverse shear force (kN)		Longitudinal bending moment (kN.m)		Longitudinal shear force (kN)	
	RV	AR	RV	AR	RV	AR	RV	AR	RV	AR
1	125 891	102 407	-	-	-	-	13 577	13 381	58	41
2(a)	95 598	112 628	87 064	119 940	2256	2119	-	-	-	-
2(b)	113 000	107 720	-	-	-	-	82 240	110 000	961	1481
4(a)	104 172	85 740	138 095	202 713	3973	4532	-	-	-	-
4(b)	119 950	100 150	-	-	-	-	135 869	320 283	2845	6420

Note: LC: Load combination
RV: Reported value
AR: Analysis result

Overall, the analysis results obtained using the model created for the Bosphorus bridge model are reasonable and consistent, indicating the validity of the structural modeling methodology adopted and the analysis approaches used.

6. CASE STUDY: A COMBINED CABLE-STAYED SUSPENSION (CSS) HYBRID BRIDGE CROSSING THE IZMIT BAY

6.1. Overview

As a case study, a three-dimensional structural model was created for a proposed combined cable-stayed suspension (CSS) hybrid configuration for a bridge crossing the Izmit Bay in the Marmara region in Turkey, and the model was used for conducting the static and dynamic analysis procedures described in Chapter 4. The types of analyses conducted on the proposed mode for the Izmit Bay Bridge include geometrically-nonlinear static analysis under dead load and determination of the initial equilibrium configuration, moving load analysis under vehicular loads, analysis for temperature effects, analysis under aerostatic wind forces, and analysis for dynamic earthquake actions.

This chapter presents details of the structural modeling and analysis methodologies and load calculations, as well as the results of the static and dynamic analyses conducted for the proposed Izmit Bay Bridge configuration. Results of the analyses were evaluated and the internal forces developing in critical structural members and displacements at critical locations under different load combinations were determined. Sources of geometric nonlinearity, including the cable sags, large deflections, and P-Delta effects, were incorporated in the structural model of the bridge. The model was calibrated geometrically to maintain its proposed configuration when subjected to dead loads. Modal analyses were performed to determine the vibration characteristics of the bridge model.

Code-compliant live loads, wind loads, and temperature changes were then imposed on the model. For earthquake response assessment, the response spectrum analysis and time-history analysis methods were both used. Bridge displacements and internal forces in the structural members as a result of the applied forces and earthquake effects were calculated in accordance with the load combinations specified by AASHTO-LRFD (2007). Member capacities and deformations were checked per the ASSHTO-LRFD specifications

for assessment of the bridge performance considering both strength and serviceability limit states.

6.2. Description of the Izmit Bay Bridge Configuration

The proposed bridge will cross the Izmit Bay on a straight alignment, joining Kaba Burun on the north side and Dil Burnu on the south. The clear distance across the bay between the north and south shores is approximately 2850 meters in the direction of the bridge alignment. According to the published hydrographic map of the Izmit Bay shown in Figure 6.1, the maximum water depth along the bridge alignment varies from 2.5 meters to 11.6 meters near the south end of the crossing. The water depth along the north half of the crossing varies between 18 meters and 42 meters. Whereas a steep seabed profile exists near the north shore, there is a shallow underwater shelf near the peninsula on the south shore. The geographic layout envisioned for the Izmit Bay bridge is shown on the hydrographic map shown in Figure 6.1 and topographic map shown in Figure 6.2.

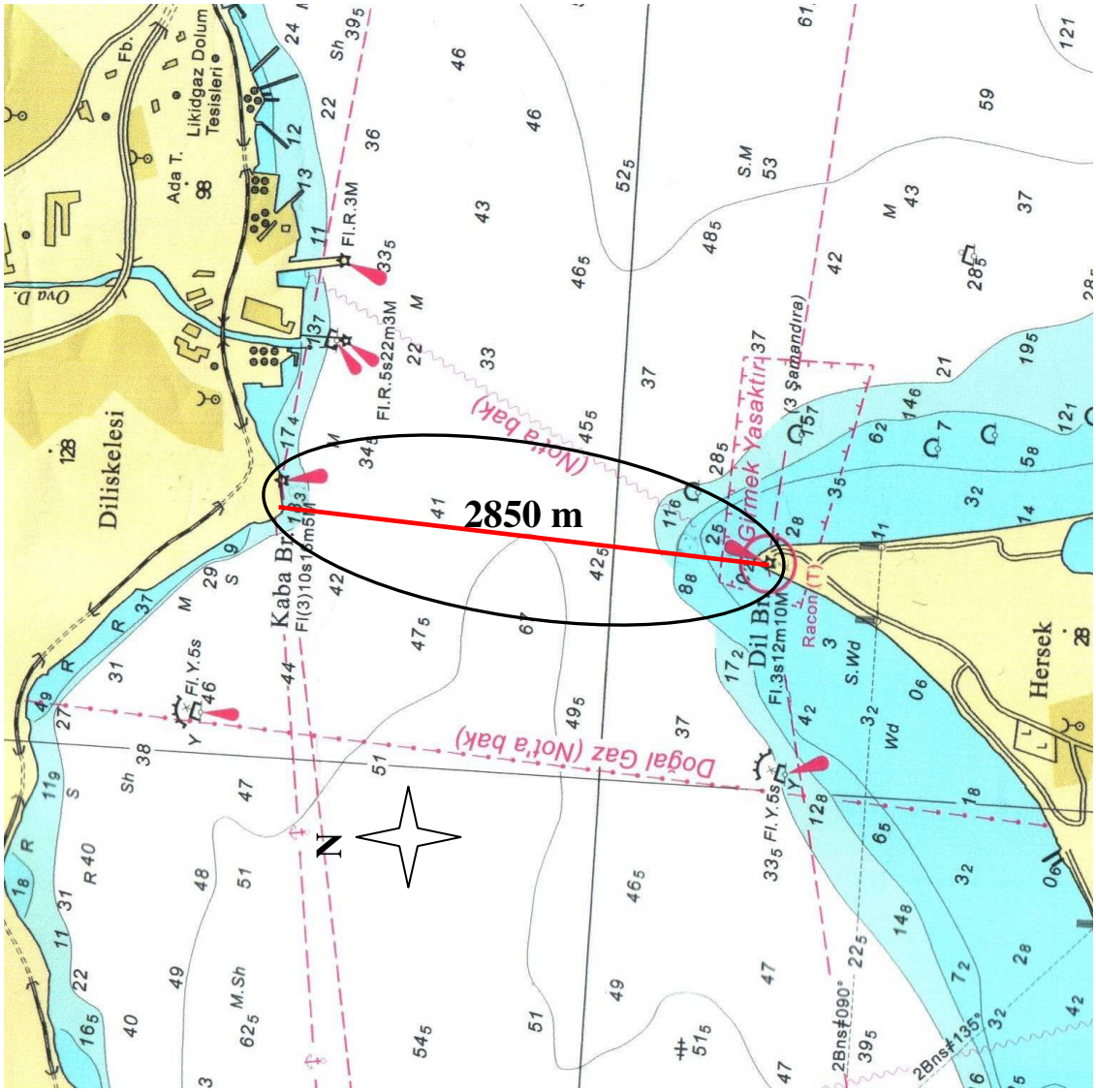

Figure 6.1. Hydrographic layout of the Izmit Bay Bridge location (TN-ONHO, 2009)

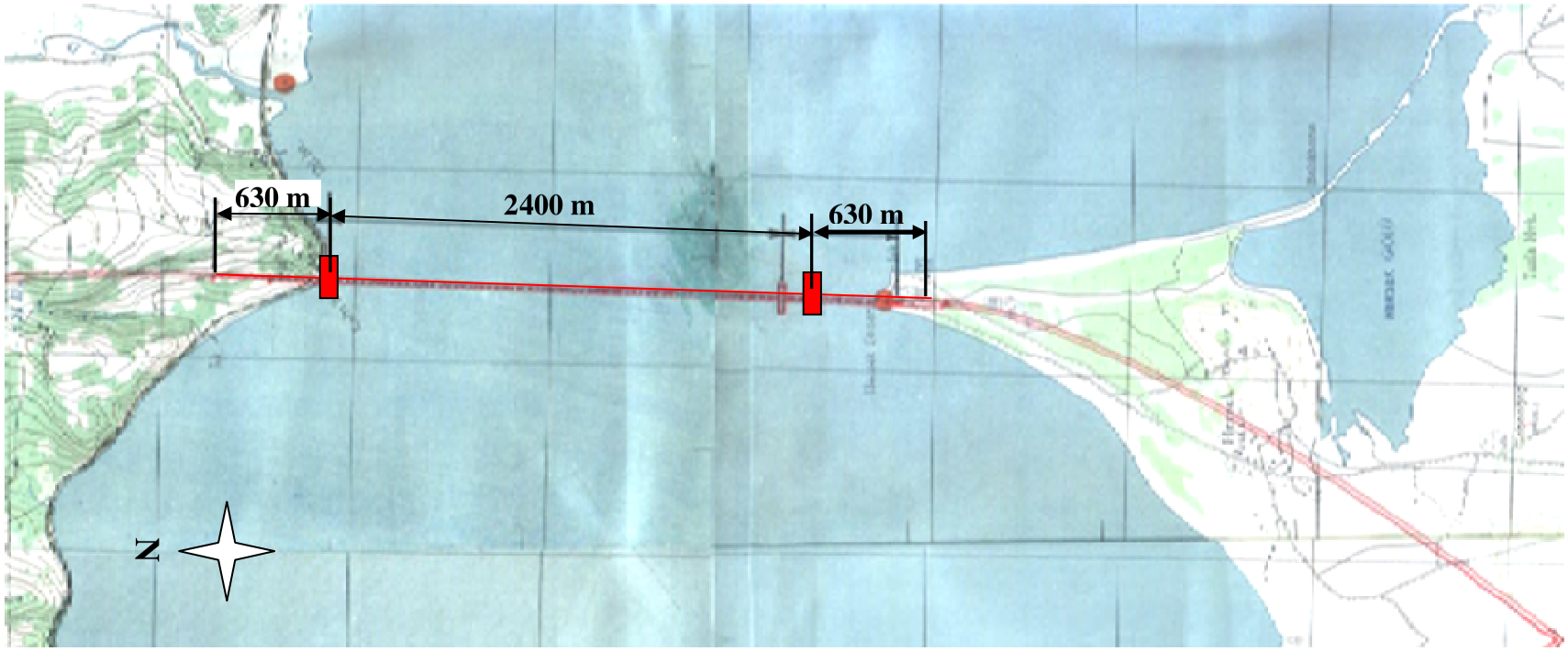

Figure 6.2. Topographic layout of the Izmit Bay Bridge location (GCM, 2009)

The Izmit Bay Bridge is envisioned as a steel combined cable-stayed and suspension (CSS) hybrid bridge, having a main span length of 2400 meters with 630 meter long cable stayed segments, and a 1140 meter long suspension segment along the centre (Figure 6.3). The two side spans are also cable stayed, and each measure 630 meters. The bridge incorporates 4 traffic lanes in each direction, each with a 3.6 meter width. A minimum clearance of 70 meters above the water level is provided. The H-shaped towers of the bridge, with slight tapering between the tower legs (44 meter width between tower legs at the base tapering to 33 meter width at top), project 395 meters above the sea level. The north tower of the bridge is constructed on dry land near the shore line; where as the south tower is constructed in shallow water 300 meters from the shore, in a region where the water depth is approximately 3 m. This was found to be optimum configuration for limiting the main span length and keeping the construction cost of the tower foundations at a minimum. The sag of suspension cable is 320 meters at the deck midspan, and the horizontal distance between the cable stay connections on the deck is 35 meters, whereas the horizontal distance between the hanger connections on the deck is 16 meters. The stay cables follow a modified fan configuration, and the vertical distance between the cable stay connections on the towers is 3.5 meters. The general configuration of the bridge is shown in Figure 6.3.

The main structural frame components of the bridge, including the box section for the deck and the box sections for the bridge towers and tower cross beams, are considered to be fabricated from high strength steel. The deck is fabricated from AASHTO-M270M Grade HPS 485W steel, with a minimum yield stress of 485 MPa, whereas the tower legs and cross beams are fabricated from AASHTO-M270M Grade 690W steel, with a minimum yield stress of 690 MPa. The suspension cables, stay cables, and hangers are considered to be manufactured from commercial Freyssinet ultra high strength steel wires, with 1860 MPa yield stress. Geometrical properties of the deck stiffening girder, the bridge towers, the suspension cables, and the hangers are described briefly in the following paragraphs.

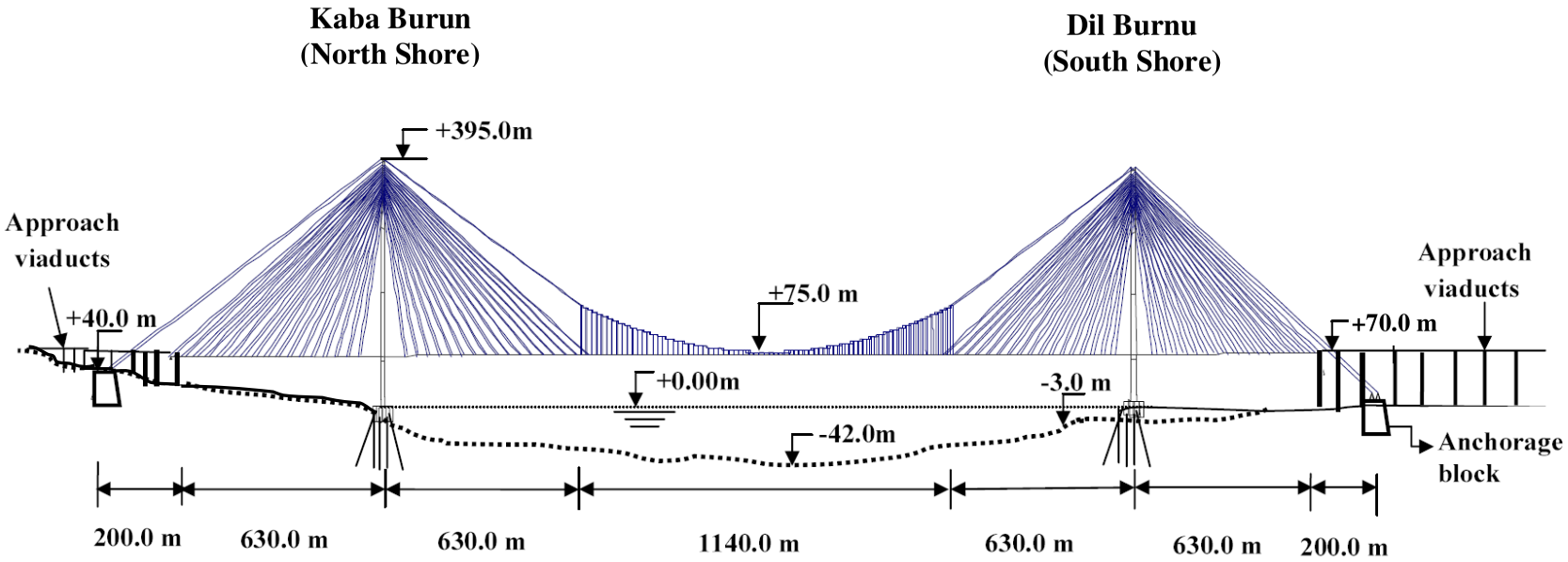

Figure 6.3. General configuration of the Izmit Bay Bridge

The box-type stiffening girder, constituting the deck of the bridge, involves an orthotropic top deck consisting of a 30 mm thick steel plate stiffened longitudinally with closed trapezoidal ribs that are spaced approximately 0.5 meters on center. The trapezoidal ribs are 300 mm deep and 400 mm wide at the base, and have a plate thickness of 12 mm. The bottom plate of the box section is also a 30 mm thick plate with the longitudinal stiffener ribs spaced at 0.50 meters on center. The geometry of the trapezoidal rib section is shown in Figure 6.5. The geometry of the box section is streamlined, with sharp edged wind noses on the sides to divide the air flow, and side plates with a modest inclination relative to the direction of the wind, for aerodynamic stability. The streamlined box section envisioned for the Izmit Bay Bridge deck is illustrated in Figure 6.4.

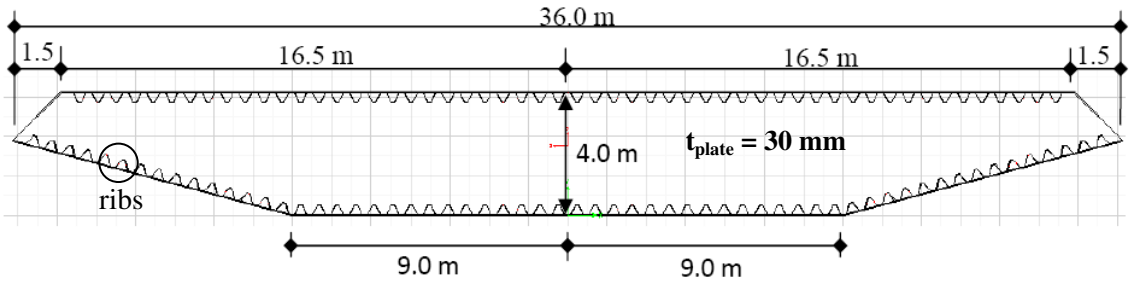

Figure 6.4. Streamlined cross section of the bridge deck

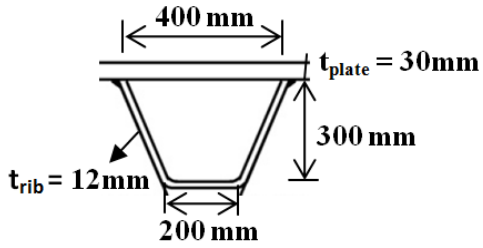

Figure 6.5. Cross section of the trapezoidal rib

Each leg of the bridge tower is a rectangular box section 10 meters wide in the transverse direction of the bridge, and tapers in the longitudinal direction from 12 meters at the bottom to 8 meters at the bottom, as shown in Figure 6.6. The plate thickness of the tower legs is 80 mm. The tower legs are stiffened longitudinally with rectangular open ribs, each 0.5 meter long and 22 mm thick, spaced 0.5 meters on center. The tower legs are connected in the transverse direction with three horizontal cross beams providing portal

bracing, which also have rectangular box sections, with 22 mm plate thickness, as shown in Figure 6.7.

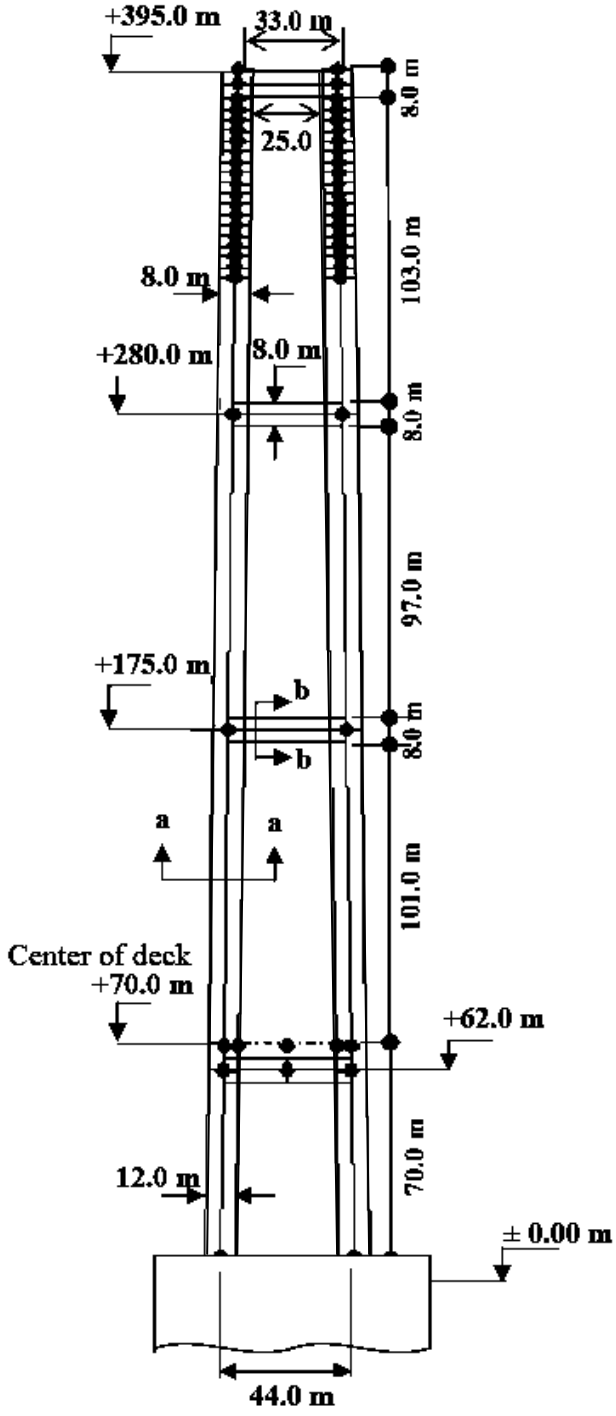

Figure 6.6. General tower layout of the Izmit Bay Bridge

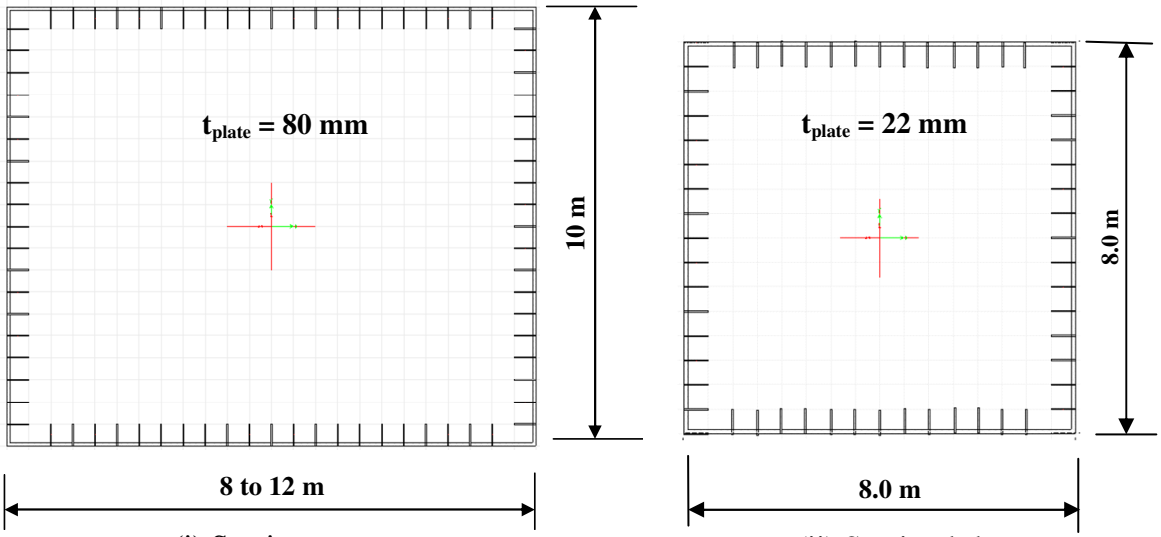

(i) Section a-a (ii) Section b-b

Figure 6.7. Cross section of the tower leg and tower cross beam

The suspension cables and stay cables of the bridge are envisioned as of the parallel-strand type, enclosed in an ultraviolet (UV) resistant high-density polyethylene (HDPE) sleeve of circular cross-section, as described in Section 3.4.3. Nominal diameters of 1.2 meters, 1.3 meters, and 0.15 meters were selected for the main span suspension cables, the side span suspension cables, and the stay cables, respectively. The hanger cables are constructed of spiral wire strands, and have a nominal diameter of 90 mm. Both suspension and stay cables are connected to the towers via pin-connected anchorages. The special anchorages described in Section 3.4.5. are used for connecting the stay cables and hangers to the bridge deck, which would facilitate pretensioning of the cables and allow adjustment of cable lengths (prestraining) during construction, for the cable-stayed or suspension system to reach its intended geometric configuration under dead loads.

6.3. Structural Modeling

Within the scope of this case study, a three-dimensional structural model of the proposed configuration for the Izmit Bay Bridge was created using the commercial structural analysis software SAP2000, and the model was used for conducting the static and dynamic analysis procedures described in Chapter 4. Information on the structural model is presented in the following subsections.

6.3.1. Material Properties

The material properties used in modeling of the main structural components for the Izmit Bay Bridge, including the suspension cables, stay cables, hangers, deck girder, towers, and tower cross beams, are listed in Table 6.1.

Table 6.1. Material properties used in the structural model

Structural Member	Yield Stress (MPa)	Modulus of Elasticity (MPa)	Unit Weight (kN/m^3)	Poisson's Ratio
Suspension/Stay Cables	1860	2.06×10^5	76.97	0.3
Hanger				
Deck Girder	485			
Towers and Cross Beams	690			

6.3.2. Main Structural Components

In the structural model of the bridge, the bridge towers, the tower cross beams and bridge deck were all represented by frame elements, whereas the suspension cables, stay cables, and hangers were represented by cable elements. The tower legs were assumed to be restrained against translation and rotation at the foundations. 729 joints, 724 frame elements and 900 degrees of freedom are existed in the global model. Illustrations of the structural model of the bridge are presented in Figures 6.8 to 6.10.

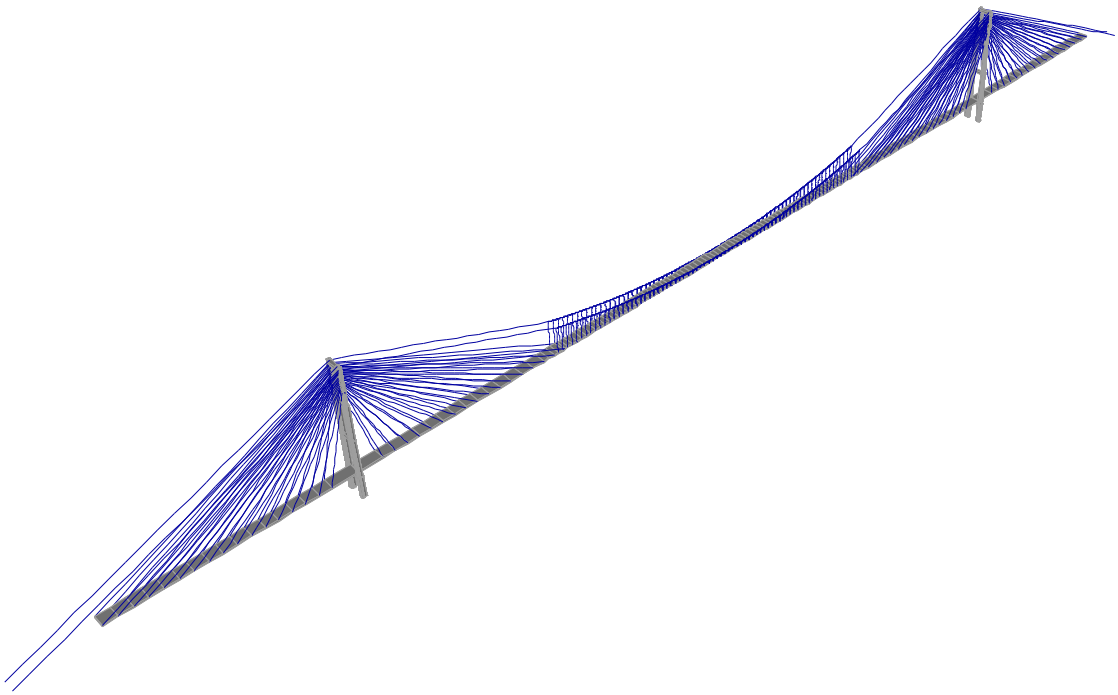

Figure 6.8. Three dimensional view of the structural model for the Izmit Bay Bridge

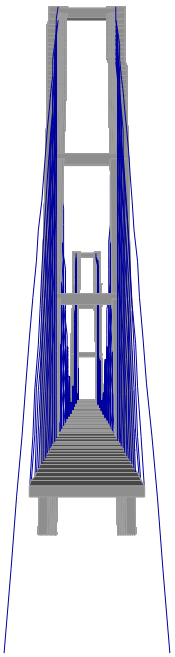

Figure 6.9. Two dimensional view of the structural model

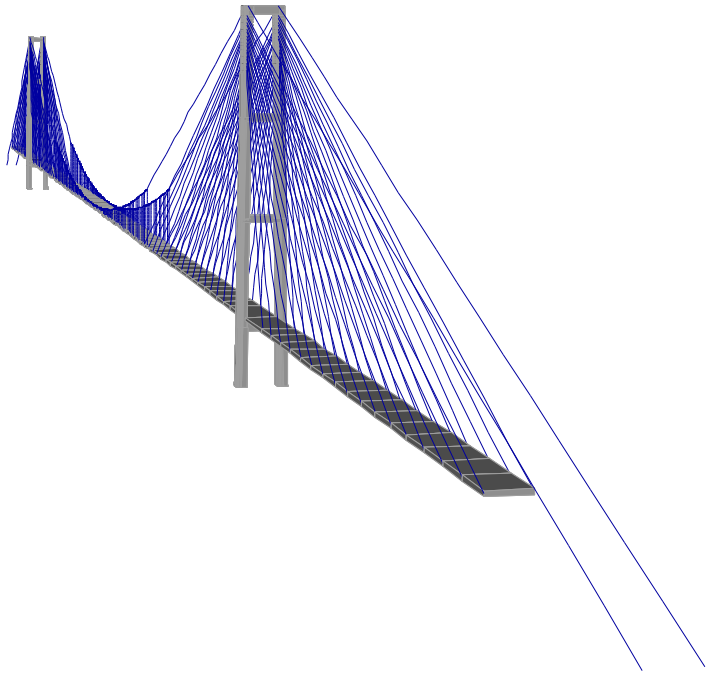

Figure 6.10. Perspective view of the structural model

In the model, cross sections of the tower legs and the tower cross beams were defined as rectangular and square box sections, considering the contribution of the stiffener ribs on the cross-sectional properties. The cross sectional properties of the tower leg and cross beams were calculated using the "section designer" tool of the software SAP2000, and are listed in Table 6.2.

Table 6.2. Cross sectional properties of the tower legs and tower cross beams

Section	Dimensions (meter)	Area (m^2)	Torsional Constant, J (m^4)	Moment of inertia, I_{3-3} (m^4)	Moment of inertia, I_{2-2} (m^4)
Tower leg upper segment	8x10x0.08	3.54	57.11	53.40	38.04
Tower leg middle segments	10x10x0.08	3.85	80.27	61.64	61.68
Tower leg lower segment	12x10x0.08	4.37	105.66	73.5	97.02
Tower cross beams	8x8x0.022	0.7021	11.17	7.45	7.45

The cross-sectional properties of the suspended deck of the bridge were also determined using the "section designer" tool, considering the contribution of the trapezoidal stiffener ribs. The cross sectional properties of the deck elements used in the structural model are listed in Table 6.3.

Table 6.3. Cross sectional properties of the deck

Section Properties	**Values**	**Units**
Cross-sectional area	3.2742	m^2
Torsional constant	71.56	m^4
Moment of Inertia about 3-3 axis	9.53	m^4
Moment of Inertia about 2-2 axis	352.76	m^4
Shear area in 2 direction	2.73	m^2
Shear area in 3 direction	290.90	m^2
Section modulus about 3-3 axis	5.26	m^3
Section modulus about 2-2 axis	29.451	m^3
Plastic modulus about 3-3 axis	5.42	m^3
Plastic modulus about 2-2 axis	19.51	m^3
Radius of Gyration about 3-3 axis	1.71	m
Radius of Gyration about 2-2 axis	10.38	m

The suspension cables, stay cables, and hangers in the structural model were defined using the cable element definition in SAP2000. Therefore, the cable elements in the model follow the stiffness formulation described in Section for 2.7. for catenary cable elements. The cross sectional properties of the suspension and hanger cable elements used in the structural model are listed in Table 6.4.

Table 6.4. Cross sectional properties of the cable elements

	Diameter (m)	Area (m2)
Center span main cable	1.20	1.1310
Side span main cable	1.30	1.3273
Hanger	0.09	0.0064
Stay cable	0.15	0.0177

6.3.3. Connection Constraints and Releases

The stay cables and hangers in the structural model were connected to the deck at nodes located on the side boundaries of the deck cross section. These nodes were

constrained to the longitudinal axis of the deck using the rigid body constraint conditions defined in SAP2000. The deck was also connected to the lower cross beams of each tower, by again defining rigid body constraints between the mid-span node of each cross beam and the end node of the deck element. However, moment releases (about longitudinal, transverse, and vertical deck axis) were assigned to the end nodes of the deck at the cross beam connections, so that the deck cannot transfer bending or torsional moments to the cross beams of the towers.

6.4. Structural Analysis Cases

The structural model of the Bosphorus Bridge was used for conducting the static and dynamic analysis procedures described in Chapter 4. The types of analyses performed using the bridge model include:

(i) Geometrically-nonlinear static analysis under dead load and determination of the initial equilibrium configuration,
(ii) Moving load analysis under vehicular loads,
(iii) Analysis for temperature effects,
(iv) Analysis under aerostatic wind forces,
(v) Analysis for dynamic earthquake effects, including:
- Free vibration (frequency) analysis,
- Nonlinear dynamic time history analysis,
- Linear response spectrum analysis.

The following subsections present the details of the analysis cases conducted, as well as evaluation of the analysis results for performance assessment of the proposed bridge configuration, considering both strength and serviceability limit states.

6.4.1. Geometrically-Nonlinear Static Analysis under Dead Load

A set of geometrically-nonlinear static analyses were first conducted on the bridge model under self-weight induced and superimposed dead loads only. The objective of this initial nonlinear analysis was to achieve the initial (deformed) equilibrium configuration of

the bridge under dead loads and cable pre-tensioning effects; that is, to determine the prestressed state of the structural components that will, together with the dead loads, will produce a deformed geometry that will be close to the intended geometrical configuration of the bridge.

In the structural model, the self weight of the suspension cables, hangers, and the deck were considered in the analysis via the unit weight of the materials listed in Table 6.1. A superimposed dead load of 52 kN/m was applied on the deck for considering the weight of the roadway surfacing, the parapets, the crash barriers, and other nonstructural components.

The initial (deformed) equilibrium configuration under dead loads was reached via adjusting the initial strain (prestrain) values in suspension cables and hangers, through a trial-and-error procedure. After performing an initial nonlinear analysis under dead load only (without any prestraining of the cables), the vertical deflections of the deck was obtained as -15.48 meters, -2.25 meters, -2.37 meters in the midspan, quarter span and side span respectively.. To reach the initial equilibrium configuration of the deck, that is to minimize the deck deflections and therefore the bending moments, prestrain values of -0.00420, -0.00240, and -0.00220 were selected as suitable values to be imposed on the main span suspension cables and hangers, the main-span stay cables, the side-span stay cables, respectively. It is important to indicate that the prestrain values applied on the cables are not the actual mechanical (stress-compatible) strains in the cable elements, but rather the required change in the cable lengths (per unit length), which will allow the deformed geometry of the bridge deck under dead loads to resemble the intended geometrical configuration.

Significant results of the dead load analysis case are listed in Table 6.5. The values in the table indicate that while prestraining of the cable elements does not considerably increase the tension forces in the cables and therefore the axial load on the bridge piers, it significantly reduces the deflections and therefore the bending moments in the bridge deck and towers. Figure 6.11 illustrates the distribution of the bending moments in the bridge deck before and after prestraining of the cables.

Table 6.5. Dead load analysis case results

	Before pre-tensioning (dead load only)	After pre-tensioning (dead load and prestrains)
Maximum vertical displacement of the deck (at the midspan)	-15.48 m	-0.92 m
Maximum tension in the main span suspension cables	544 240 kN	557 808 kN
Maximum bending moment in the deck about transverse axis	-974 354 kN.m	-527 406 kN.m
Axial load in the tower leg	-810 997 kN	-823 074 kN
Maximum bending moment in the tower leg	-148 234 kN.m	-103 635 kN.m

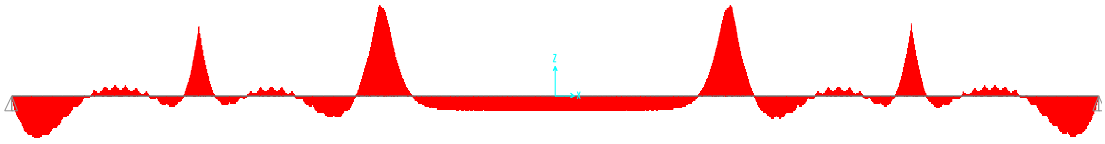

(i) Before pre-tensioning

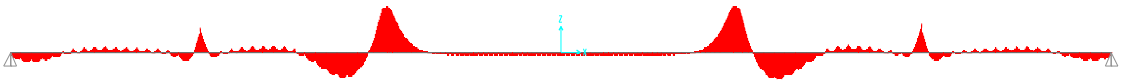

(ii) After pre-tensioning

Figure 6.11. Bending moment distributions in the bridge deck

After the initial equilibrium state of the bridge was reached at the end of the geometrically-nonlinear analysis under combined prestrain and dead load effects, the bridge model has attained its overall stiffness for further linear on nonlinear analysis under superimposed loads and dynamic actions.

6.4.2. Moving Load Analysis

For analysis of the bridge under vehicular live loads, the traffic live load specifications of the AAHTO-LRFD code described in Section 4.2 were used in the structural model. The “Bridge Analysis” tools in the SAP2000 program were used to determine the response of the bridge to the moving vehicle loads, as described in Section

4.3. Four traffic lanes, each with a 3.6 meter width, were defined in each direction of the bridge deck. The moving load analysis considered all possible permutations for the AASHTO-LRFD vehicle classes assigned, and provided the maximum and minimum displacements and internal forces, resulting from multiple and moving lane loads acting on the bridge deck. Significant results of the dead load analysis case are listed in Table 6.6.

Table 6.6. Moving live load analysis case results

	Under moving live load
Maximum vertical displacement of the deck (at the midspan)	-2.95 m
Maximum tension in the main span suspension cables	597 096 kN
Maximum bending moment in the deck about transverse axis	301 644kN.m
Axial load on the tower leg	883 100 kN
Maximum bending moment on the tower leg	124 432 kN.m

6.4.3. Analysis under Temperature Effects

For analysis under temperature effects, a uniform temperature change of ± 30º was imposed on the bridge deck and towers, as well as the tower cross beams and cable elements. Additionally, temperature gradients were considered in the two transverse directions for the deck, tower, and tower cross beams elements, as described in Section 4.4.

Significant results of the temperature load analysis case are listed in Table 6.7, for the uniform temperature change and the transverse temperature gradient conditions. For the uniform temperature change applied on all components, the maximum deflection and bending moment in the deck develops at the connection with the longest hanger. For the temperature gradient in the transverse direction of the deck (temperature gradient 3), the maximum deflection of the deck occurs at the midspan, where the maximum bending moment also develops.

Table 6.7. Temperature load analysis case results

Deck	Deflection at midspan (m)	Deflection at the longest hanger connection (m)	Bending moment at midspan (kN.m)	Bending moment at the longest hanger connection (kN.m)
Uniform temperature change	0.317	0.257	-701	-2267
Temperature gradient 2	-0.028	-0.024	172 248	171 418
Temperature gradient 3	-0.073	-0.276	587 034	582 067

6.4.4. Wind Load Analysis

For analysis under aerostatic wind forces, the equivalent static wind loads acting on the bridge towers were calculated according to the ACI 307 specifications described in Sections 4.5 and 4.6. The formulations for the determination of the design wind moment M_z, the dynamic wind load w_{dz}, and the gust factor G_o were provided in Section 4.6. Since calculation of the gust factor (G_o) is based on the first fundamental period of vibration of the towers in the wind directions, the periods of vibration of the entire bridge, corresponding to the first swaying vibration mode of the towers, were first calculated using a free-vibration analysis, as 5.26 sec and 11.02 sec in the longitudinal and transverse directions of the bridge, respectively. The calculated wind load profiles in acting on the bridge tower legs in the longitudinal transverse bridge directions are illustrated in Figures 6.12 and 6.13.

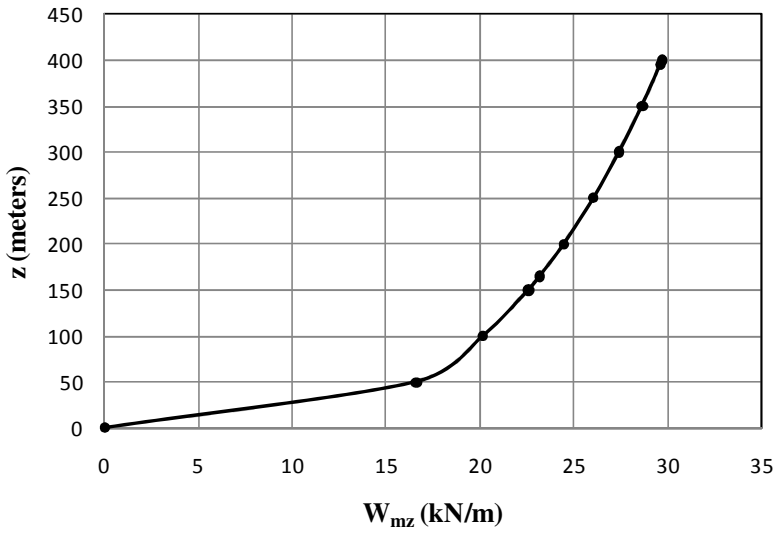

(i) Mean load profile

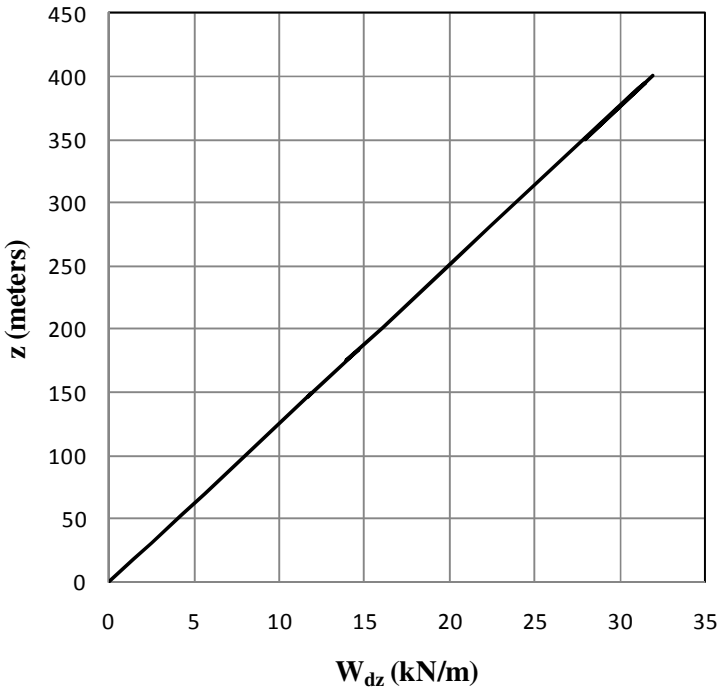

(ii) Dynamic load profile

Figure 6.12. Wind load profiles on the bridge tower legs in the longitudinal bridge direction

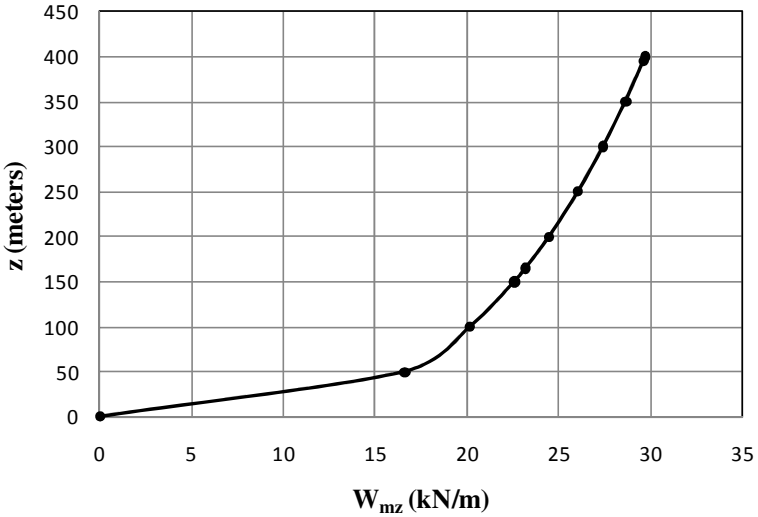

(i) Mean load profile

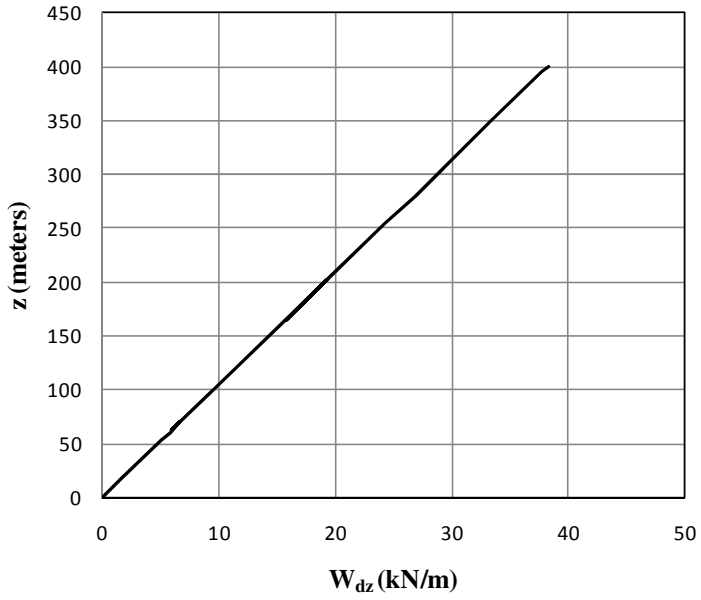

(ii) Dynamic load profile

Figure 6.13. Wind load profiles on the bridge tower legs in the transverse bridge direction

The aerostatic wind forces acting per unit length of the bridge deck were calculated using the drag force, lift force and pitch moment formulations described in Chapter 4, Section 4.5. The aerostatic coefficients (C_y, C_z and C_m) used in the calculations for the case of horizontal (0°) wind incidence are listed in Table 6.8. Since the bridge has a streamlined deck cross section like Messina Strait Bridge and the Normandie Bridge, the aerostatic

coefficient values used in the analysis were taken as comparable values to those reported in Table 4.3 for the two bridges.

Table 6.8. Aerostatic coefficients used for calculating wind loads on the deck

C_y	C_z	C_m
0.07	-0.24	0.015

The aerostatic drag force, lift force and pitch moment acting per unit length of the deck were calculated accordingly, for the case of horizontal (α=0°) wind incidence. The values used in the analysis and are listed in Table 6.9.

Table 6.9. Aerostatic wind loads acting on the deck

Drag force, $F_y(\alpha)$	3.43 kN/m
Lift force, $F_z(\alpha)$	52.96 kN/m
Pitch moment $M(\alpha)$	60.31 kN.m/m

Wind load analyses of the bridge model were conducted under the wind loads acting on the deck and the towers, calculated as described above. Displacements obtained at the end of the analyses at critical locations of the bridge are presented in Tables 6.10 to 6.12.

Table 6.10 lists the deck midspan displacements under the wind loads applied on the deck. The values reveal how the predominant direction of the displacement is related to either the drag (transverse load), the lift (vertical load), or the moment (torque) component of the wind load. Displacements under the combined effect of the wind load components are also given in the table. The displacements at the quarter-span of the deck are listed in Table 6.11.

Table 6.10. Deck midspan displacements under wind loads on deck

	Wind load case on deck	Transverse deflection (m)	Vertical deflection (m)	Twist angle (rad)
Deck midspan	Wind drag	**1.759**	0.0000	0.0004
	Wind lift	0.0000	**-2.7305**	0.0000
	Wind moment	0.0229	0.0000	**-0.0037**
	Combined	1.7794	-2.7305	-0.0041

Table 6.11. Deck quarter-span displacements under wind loads on deck

	Wind load case on deck	Transverse deflection (m)	Vertical deflection (m)	Twist angle (rad)
Deck quarter-span	Wind drag	**1.0800**	0.0000	-0.0026
	Wind lift	0.0000	**-1.2650**	0.0000
	Wind moment	0.0190	0.0000	-0.0026
	Combined	**1.2385**	**-1.2650**	0.0112

Table 6.12 shows the displacements calculated at the top of the towers under the wind loads applied on the towers. The results indicate that the tower displacements are significantly higher in the transverse direction of the bridge, since the top of the towers are restrained by the suspension cables in the longitudinal bridge direction.

Table 6.12. Tower displacements under wind loads on towers

	Wind load case on tower	Deflection in longitudinal bridge direction (m)	Deflection in transverse bridge direction (m)
Tower top	Longitudinal bridge direction	0.0228	0.0000
	Transverse bridge direction	-0.0000	0.9839

Other significant results of the wind load analysis case, under combined wind loads acting on both the deck and towers of the bridge, are listed in Table 6.13.

Table 6.13. Wind load analysis case results

	Under combined wind load (acting on both deck and towers)
Maximum vertical displacement of the deck (at the midspan)	-2.73 m
Maximum tension in the main span suspension cables	47 590 kN
Maximum bending moment in the deck about transverse axis	-281 265 kN.m
Maximum bending moment in the deck about vertical axis	17 188 kN.m
Axial load on the tower leg	22 593 kN

Table 6.13. Wind load analysis case results (cont'd.)

	Under combined wind load (acting on both deck and towers)
Maximum bending moment on the tower leg in longitudinal bridge direction	-818 407 kNm
Maximum bending moment on the tower leg in transverse bridge direction	-286 947 kNm

6.4.5. Free Vibration (Modal) Analysis

Prior to commencing the dynamic analysis of the structural model under dynamic earthquake actions, a free vibration analysis (described in Section 4.7.1) was performed for determining the vibration characteristics of the structure. The free vibration analysis was conducted using the modal analysis case defined in the program SAP2000, in order to calculate the natural frequencies, mode shapes, and mass participation factors (effective modal mass values) of the model, associated with the first 200 modes of vibration of the structure. The cyclic frequency and period values calculated first 10 modes of vibration of the bridge are listed in Table 6.14.

Table 6.14. Calculated periods and cyclic frequencies of the bridge for the first 10 vibration modes

Mode Number	Period (sec)	Frequency (cyc/sec)
1	27.14	0.037
2	12.63	0.079
3	10.60	0.094
4	10.32	0.096
5	10.31	0.097
6	9.97	0.100
7	8.77	0.114
8	8.56	0.117
9	8.19	0.122
10	8.11	0.123

The mode shapes obtained for the first six modes of vibration of the bridge are shown in Figures 6.14 to 6.19.

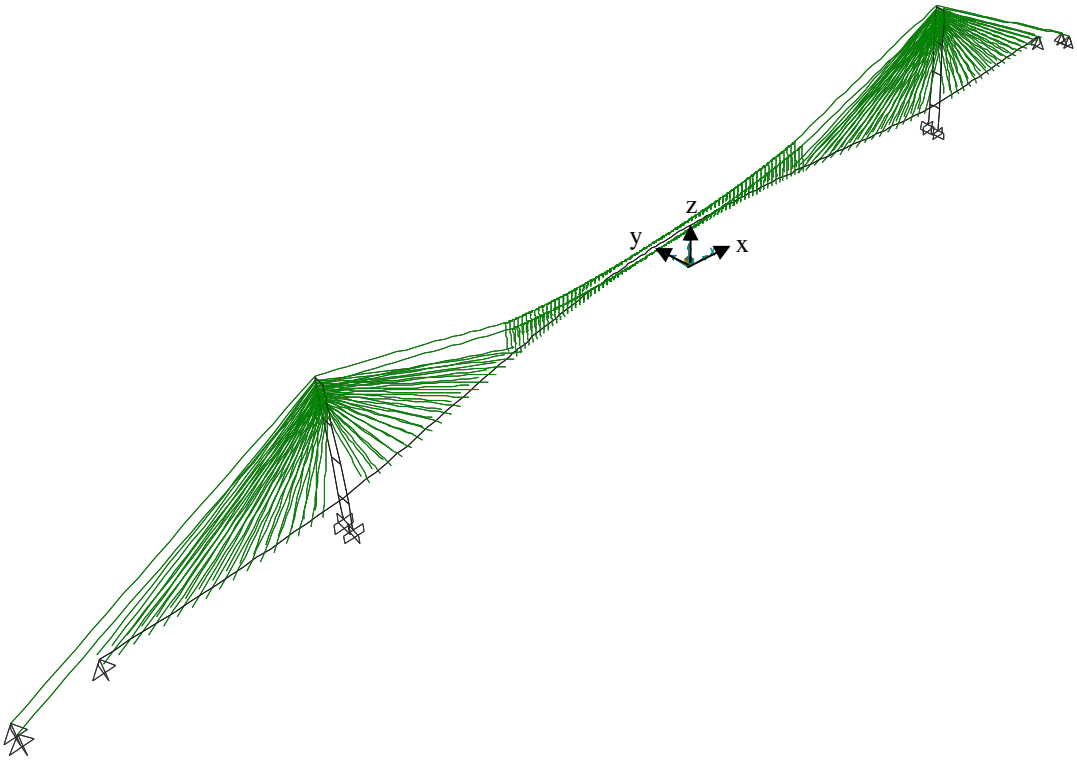

Figure 6.14. Mode shapes for the first mode of vibration (T=27.14 sec)

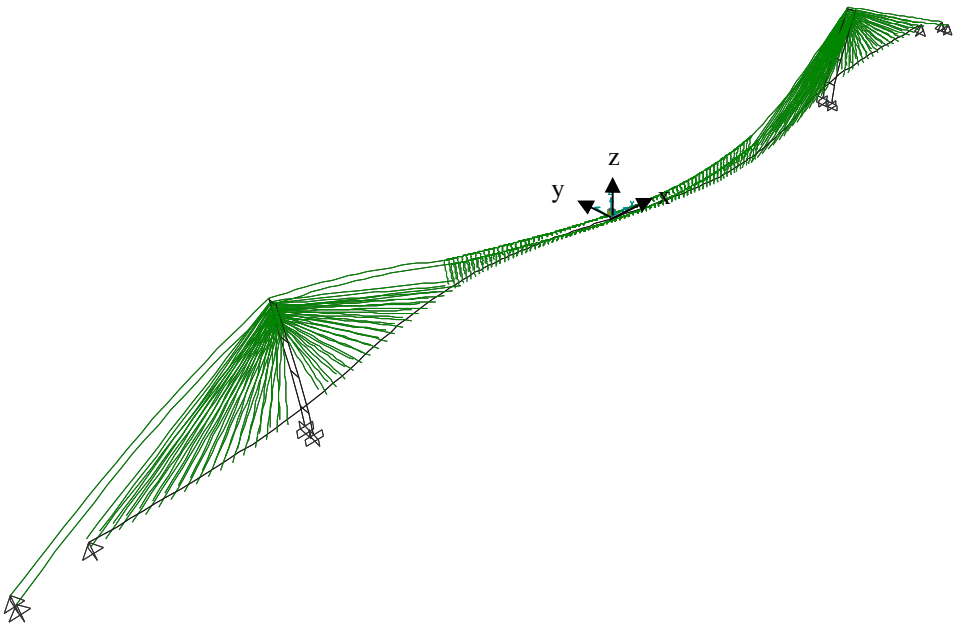

Figure 6.15. Mode shapes for the second mode of vibration (T=12.63 sec)

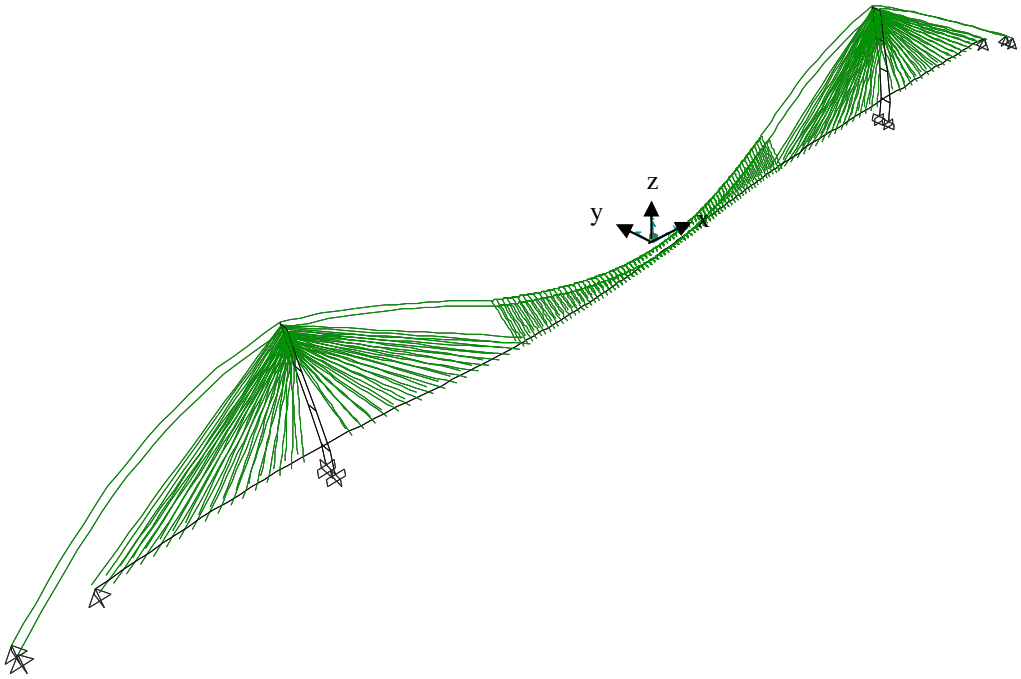

Figure 6.16. Mode shapes for the third mode of vibration (T=10.60 sec)

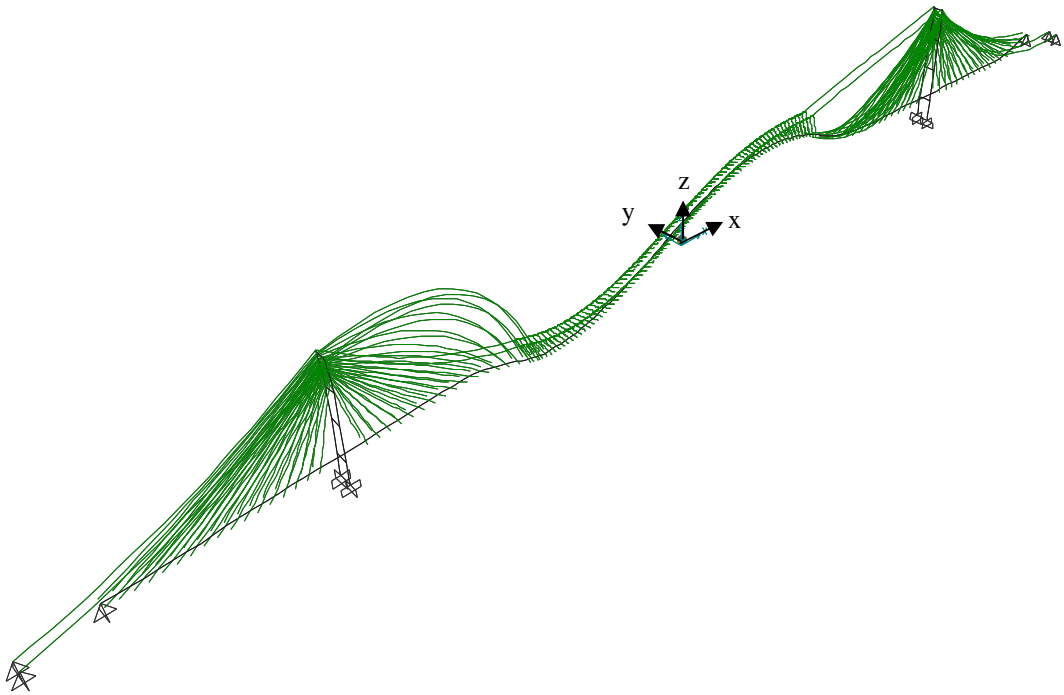

Figure 6.17. Mode shapes for the fourth mode of vibration (T=10.32sec)

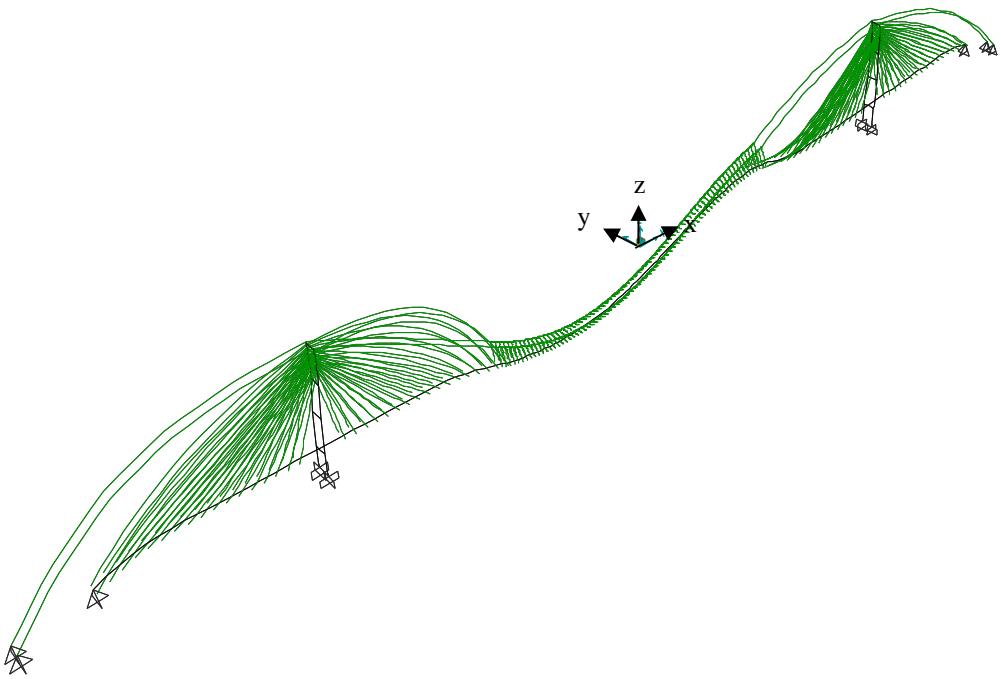

Figure 6.18. Mode shapes for the fifth mode of vibration (T=10.31 sec)

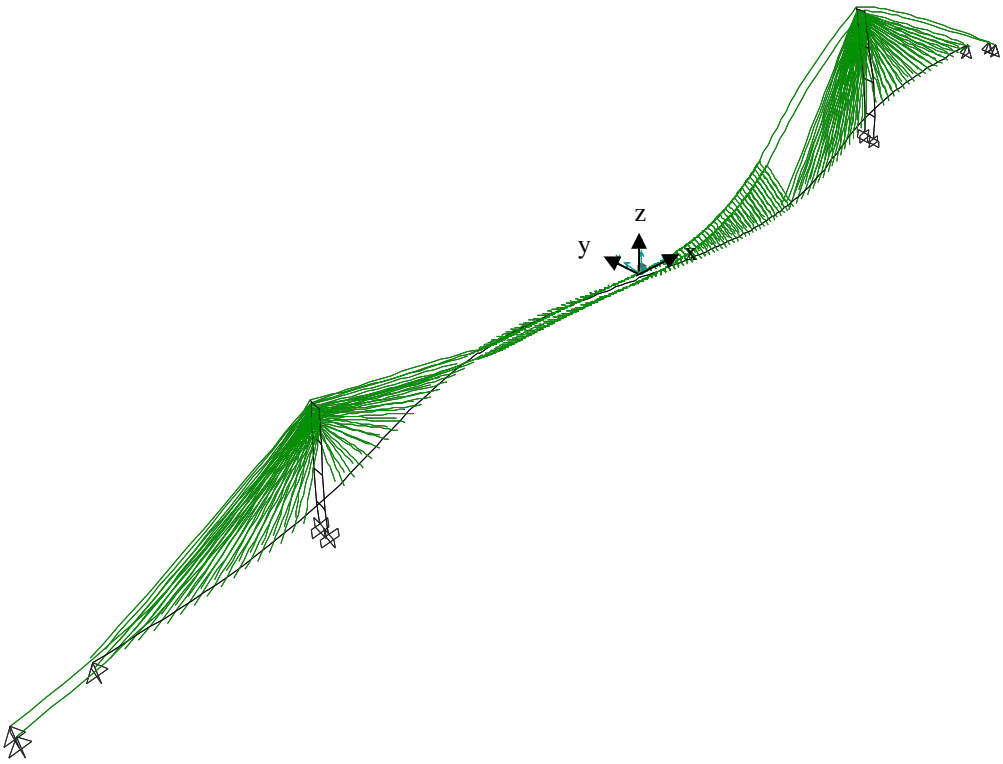

Figure 6.19. Mode shapes for the sixth mode of vibration (T=9.97 sec)

The first 15 modes of vibration with significant modal mass participation factors (normalized effective modal masses) are listed in Table 6.15, along with their dominant direction of motion and respective modal mass participation ratio (MPR). The selected modes in the table are those with a significant MPR value in any single direction. In the table, U_X, U_Y, and U_Z represent motion in longitudinal bridge direction, transverse bridge direction, and vertical direction, respectively, and R_x represents rotation about the longitudinal direction of the bridge, which may be interpreted as a twisting rotation on the deck.

The MPR values provide a measure of how important a particular mode of vibration is for the overall response of the bridge to acceleration-induced loads in each global direction, and help ensure that a significant and required number of vibration modes are included in the earthquake response analysis of the structure. The sum of the MPR values for all of the 200 modes considered in the analysis are listed at the bottom of Table 6.15, and cumulative MPR values are plotted with respect to the vibration mode number in Figure 6.20. The cumulative percentages indicate that the accumulated mass participation ratio for the first 200 modes of vibration is almost 100% in transverse translational directions of the bridge, as well as in the rotational direction about the longitudinal bridge axis. On the other hand, the accumulated mass participation ratio for is only 74% in the vertical direction, indicating that more modes of vibration need to be considered in the dynamic analysis of the structure under vertical accelerations. Analysis of the bridge under vertical ground accelerations is beyond the scope of this case study; therefore, 200 modes were found to sufficient for analyzing the bridge under horizontal earthquake accelerations.

Table 6.15. Vibration modes with the highest 15 mass participation ratios

No.	Mode	Period	Mode shape description	Mass Participation Ratios (%)			
				U_X	U_Y	U_Z	R_X
1	1	27.14	U_Y	1.975E-15	**44.83**	1.958E-14	**7.0032**
2	3	10.59	U_Y	7.221E-13	**21.06**	7.711E-12	**71.14**
3	5	10.31	U_Z	0.2535	1.922E-12	**2.0157**	6.027E-11
4	22	5.46	U_Z	0.1737	2.098E-11	**18.46**	5.845E-13
5	23	5.25	U_X	**10.56**	4.201E-11	0.3878	1.397E-16
6	27	4.84	U_Z	0.0017	1.336E-11	**22.15**	6.825E-12
7	41	3.78	U_Y	5.318E-10	**9.2666**	1.332E-10	0.1226
8	58	2.98	U_Z	0.0004355	2.142E-12	**10.345**	1.268E-12
9	62	2.84	U_X	**2.1073**	4.628E-11	0.0005004	2.475E-12
10	109	1.68	U_X	**37.4311**	1.034E-12	0.0031	1.088E-14
11	113	1.62	U_X	**8.8771**	8.298E-12	0.000001867	1.046E-13
12	115	1.59	U_Z	0.0014	3.908E-11	**4.2646**	9.88E-12
13	116	1.52	U_X	**5.9107**	3.081E-12	0.0001113	6.879E-17
14	121	1.34	U_X	**8.1415**	5.343E-12	0.0001016	5.332E-13
15	178	0.628	U_X	**4.15**	1.714E-13	0.0035	1.598E-11
SUM (over all 200 modes considered)				87.9	99.2	73.6	99.6

Note: U_X: longitudinal motion, U_Y: transverse motion, U_Z: vertical motion,
R_X, R_Y, R_Z: rotations about the longitudinal, transverse, and vertical bridge axes

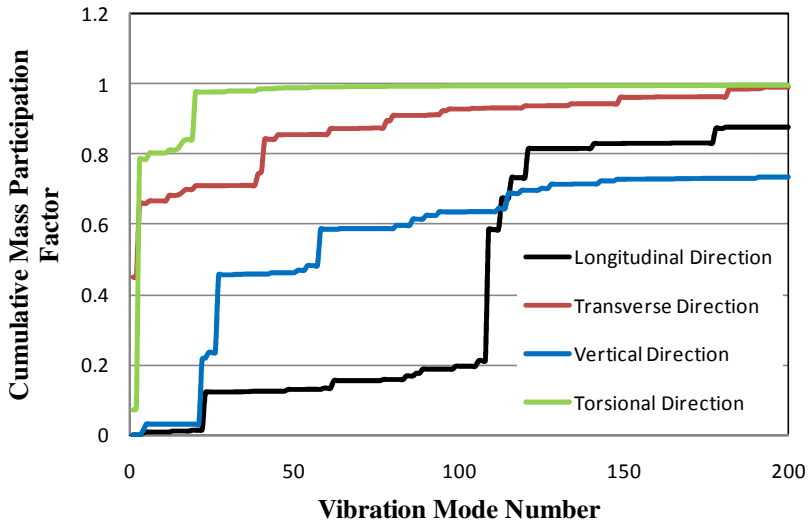

Figure 6.20. Increase in cumulative mass participation factor with the number of vibration modes

6.4.6. Time–History Response Analysis of Earthquake Effects

As a first method for determining the response of the bridge to dynamic earthquake actions, a set of geometrically-nonlinear dynamic time-history analyses were conducted by applying a strong ground acceleration record on the bridge model. This was done not only to be able to observe the nonlinear dynamic behavior of the bridge under a particular and real ground motion time history, but also to be able to compare the results of the nonlinear time-history analysis with the results of response spectrum (modal superposition) analysis method. The results of the nonlinear time history analysis were obtained in terms of both displacement time histories at critical locations of the bridge, and internal force time histories at critical sections on the bridge deck and the bridge towers.

The North-South horizontal ground acceleration time history recorded at the Imperial Valley Irrigation District substation in El Centro, California, during the May 19, 1940 Imperial Valley earthquake (described in Section 5.5.6) was used in the nonlinear time history analysis of the bridge model. The peak ground acceleration recorded at the El Centro station in the North-South direction was 0.32g. The ground acceleration record was applied nonconcurrently in both the longitudinal and transverse directions of the bridge. In this study, El-Centro ground acceleration record was selected as an illustrative example in order to be able to execute the dynamic seismic response of the long span bridges. A particular site-specific ground motion data should have been used in order to obtain more realistic results compatible with the soil conditions under the tower foundations. No soil report was available about the soil conditions for the vicinity of the tower foundation, at the time of this study. Therefore, neither the predominant period of the soil, nor the amplification characteristics were determined. However, after all these pertinent soil data become available, a more site-specific ground motion record must be used, for the nonlinear time history analyses.

In the nonlinear time-history analysis, the earthquake excitation was applied as inertial loading on the entire structural model of the bridge. Geometrical nonlinearity in the cable elements of the model was considered in the analysis, as well as P-Delta and large displacement effects. Mass and stiffness proportional Rayleigh damping was used to assign the damping properties of the model, by specifying critical damping ratio values of 2%

corresponding to natural period values of 30.0 sec and 0.5 sec. Variation of the damping ratio values used in the structural model with the natural cyclic frequencies of the model is plotted in Fig. 6.21.

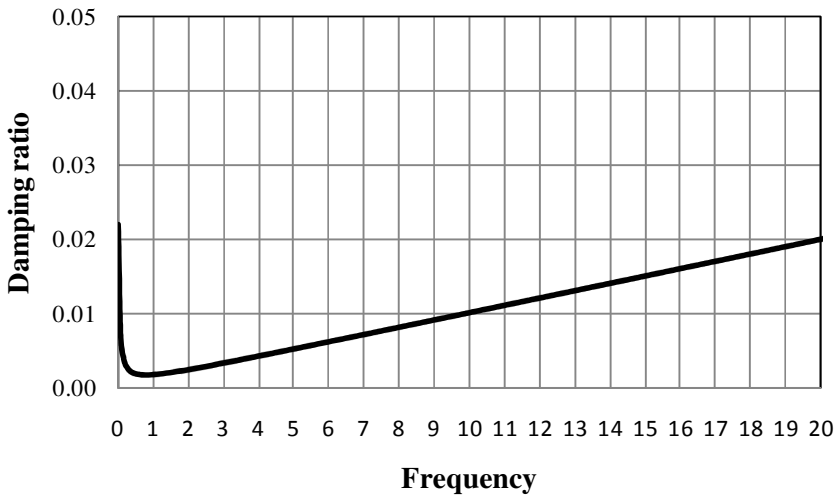

Figure 6.21. Variation of the damping ratio with natural cyclic frequency in the structural model

The results of the nonlinear time history analysis provided displacement time histories at critical locations on the bridge and time histories of internal forces (shear forces, bending moments, axial force, torque) at critical sections on the bridge deck and the bridge towers. Maximum values were used in evaluation of the bridge response and comparison with response spectrum analysis results. The displacement time histories calculated at the midspan of the bridge deck and the top of the bridge towers in longitudinal and transverse directions of the bridge, are presented in in Figures 6.22 to 6.25, for illustration purposes.

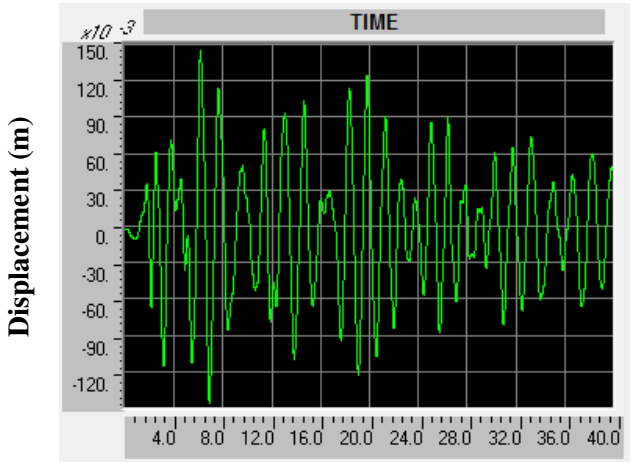

Figure 6.22. Nonlinear time-history analysis results: deck midspan displacement in longitudinal bridge direction

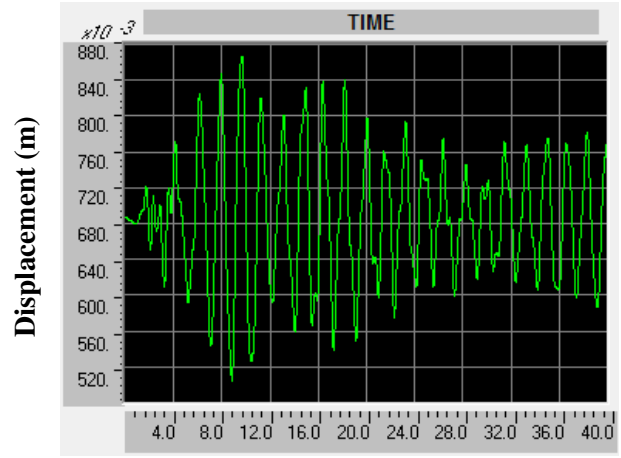

Figure 6.23. Nonlinear time-history analysis results: tower top displacement in longitudinal bridge direction

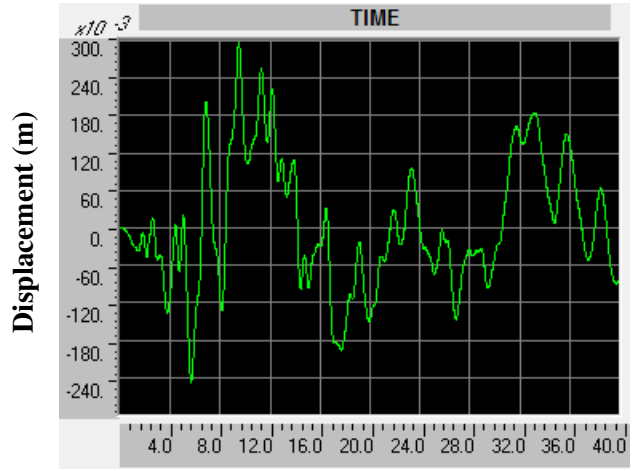

Figure 6.24. Nonlinear time history analysis results: deck midspan displacement in transverse bridge direction

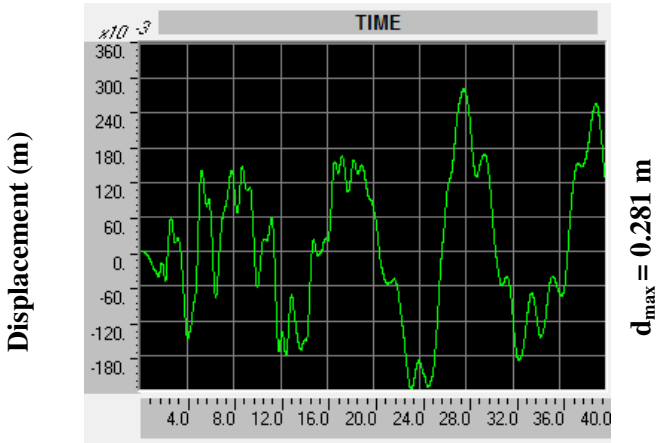

Figure 6.25. Nonlinear time history analysis results: tower top displacement in transverse bridge direction

6.4.7. Earthquake Response Spectrum Analysis

As a second method for determining the response of the bridge to dynamic earthquake actions, a set of response spectrum analyses were also conducted in the longitudinal and transverse directions of the bridge, to be able to compare the results of the nonlinear time-history analysis with the results of response spectrum analysis. The results of the response analysis were obtained in terms of both maximum displacement at critical locations of the bridge, and maximum internal forces at critical sections on the bridge deck and the bridge towers.

For the analysis, response spectrum (spectral pseudo-acceleration versus natural period) functions were applied on the structural model, separately in the longitudinal and transverse directions of the bridge. A response spectrum analysis was not conducted in the vertical direction. The complete quadratic combination (CQC) method of modal superposition was used, to consider the statistical coupling between closely-spaced vibration modes in the response of the structure, as described in Section 4.7.2. A critical damping ratio value of 2% was assigned to all modes of vibration. The response spectrum functions applied on the model in the longitudinal and transverse bridge directions were generated for the El Centro ground acceleration time history data described in the previous section. This was done to be able to directly compare the results of the nonlinear time history analysis with the results of the linear response spectrum analysis, for the same

ground excitation. The spectral pseudo acceleration response spectrum for the El Centro ground acceleration record and 2% critical damping ratio, which was used in the analysis.

The AASHTO 2006 design response spectrum function, which is readily available in SAP2000, was also used as an alternative response spectrum analysis procedure. The required coefficients to generate the AASHTO design spectrum were selected according to relevant specifications of the AASHTO-LRFD 2007 code. For the present analysis, an acceleration coefficient of 0.29g was selected, which is comparable with the 0.32g peak ground acceleration value of the El Centro ground motion. For the site coefficient, soil profile II was selected, which is defined for stiff cohesive or deep cohesionless soils (stable deposits of sands, gravels, or stiff clays) over the rock, with the soil depth exceeding 60 meters. It is stated in AASHTO-LRFD that in locations where the soil properties are not known in sufficient detail, the site coefficient for soil profile type II shall be used.

6.4.8. Comparison of Nonlinear Time History and Response Spectrum Analysis Results

The results of the nonlinear time history analysis and the response spectrum analyses are compared in Table 6.16. Values obtained for the maximum displacements at the midspan and quarter-span of the deck, maximum displacements at the top of the towers, maximum bending moments in the deck and the tower legs, and maximum axial forces in the suspension cables are compared in the table.

Table 6.16. Comparison of nonlinear time history and response spectrum analysis results

Response	Direction	El Centro nonlinear time history analysis	El Centro response spectrum analysis	AASHTO response spectrum analysis
Suspension deck mid-span diplacement (m)	longitudinal	0.145	0.0976	0.1085
	transverse	0.290	0.27	10.12
Deck quarter-span displacement (m)	longitudinal	0.186	0.084	0.094
	transverse	0.258	0.189	6.33

Table 6.16. Comparison of nonlinear time history and response spectrum analysis results (cont'd.)

Response	Direction	El Centro nonlinear time history analysis	El Centro response spectrum analysis	AASHTO response spectrum analysis
Maximum displacement in deck side span (m)	longitudinal	0.027	0.0096	0.011
	transverse	0.169	0.100	0.35146
Displacement at top of tower (m)	longitudinal	0.867	0.124	0.141
	transverse	0.281	0.242	1.927
Maximum moment in the suspension deck segment (kN.m)	about transverse deck axis	75628	23630	24180
	about vertical deck axis	842 441	620 490	1 466 707
Maximum moment in the cable stayed deck segment (kN.m)	about transverse deck axis	85 407	57 560	62 230
	about vertical deck axis	529 852	620 490	884 860
Maximum moment in the tower (kN.m)	in longitudinal bridge direction	641 747	958 930	761 285
	in transverse bridge direction	108 204	4440	3170

The comparisons indicate that the results are generally comparable, although the AASHTO response spectrum analysis may provide displacements that are significantly larger than the results of the ground motion time history analysis or ground motion response spectrum analysis. This is expected, since the AASHTO spectrum is a design spectrum, and involves a certain amount of conservatism in predicting the characteristics of a critical design ground motion to be expected at a site. For example, the pseudo-accelerations predicted by the AASHTO spectrum are significantly larger than the El

Centro Spectrum in the large period range, which corresponds to the displacement-sensitive region of the response and governs the displacements in the structure. Therefore, it is natural that the AASHTO spectrum significantly overestimates the transverse displacement of the deck and therefore the bending moment in the deck about the vertical axis, since the natural vibration of the transverse displacement mode of the deck is very large (27.14 sec for vibration mode 1, as indicated in Table 6.15).

Comparing the results of the time history analysis and the response spectrum analysis for the El Centro ground motion, the discrepancies emphasize that the response spectrum analysis method is only an approximate method, and its applicability for such a suspension bridge system may be questionable. In the case of a complex, three dimensional structures, with numerous closely-spaced modes, such as suspension bridges, great caution should be exercised in employing the response spectrum method. The results of the time history analysis presented in this study are considered much more reliable than the results of the response spectrum analysis.

6.5. Design Load Combinations and Limit States

In the analysis of the proposed configuration for the Izmit Bay Bridge under combined loading, the AASHO-LRFD (2007) load factors and limit states described in Section 4.8.1 were used. The load combinations selected for the analysis of the bridge, which include dead load, live load, wind load, temperature load, and earthquake actions, are listed in Table 6.17.

Table 6.17. Design load combinations used in the analysis of the Izmit Bay Bridge

AASHTO Load Combination Limit State	Load Combination
STRENGTH I	$1.0DL + 1.75LL + 0.50Temp^{(+)}$ $1.0DL + 1.75LL + 0.50Temp^{(-)}$
STRENGTH III	$1.0DL + 1.40Wind_{(x)} + 0.50Temp^{(+)}$ $1.0DL + 1.40Wind_{(y)} + 0.50Temp^{(-)}$ $1.0DL + 1.40Wind_{(x)} + 0.50Temp^{(-)}$ $1.0DL + 1.40Wind_{(y)} + 0.50Temp^{(+)}$

Table 6.17. Design load combinations used in the analysis of the Izmit Bay Bridge (cont'd.)

AASHTO Load Combination Limit State	Load Combination
STRENGTH V	$1.0DL + 1.35LL + 0.40Wind_{(x)} + 0.50Temp^{(+)}$ $1.0DL + 1.35LL + 0.40Wind_{(x)} + 0.50Temp^{(-)}$ $1.0DL + 1.35LL + 0.40Wind_{(y)} + 0.50Temp^{(+)}$ $1.0DL + 1.35LL + 0.40Wind_{(y)} + 0.50Temp^{(-)}$
EXTREME EVENT	$1.0DL + 0.50LL + 1.0EQ_{(x)} + 0.30EQ_{(y)}$ $1.0DL + 0.50LL + 1.0EQ_{(y)} + 0.30EQ_{(x)}$
SERVICE I	$1.0DL + 1.0LL + 1.0Wind_{(x)} + 0.50Temp^{(+)}$ $1.0DL + 1.0LL + 1.0Wind_{(x)} + 0.50Temp^{(-)}$ $1.0DL + 1.0LL + 1.0Wind_{(y)} + 0.50Temp^{(+)}$ $1.0DL + 1.0LL + 1.0Wind_{(y)} + 0.50Temp^{(-)}$

The analysis results obtained for internal forces at critical sections of the bridge, corresponding to the "envelope" of the strength and extreme event limit state load combinations, are listed in Table 6.18. The envelope values in the table were compared with member design capacities, according to specifications of the ASSHTO-LRFD 2007 code, as described in the next section.

Table 6.18. Envelope internal force resultant values at critical sections

Section	Envelope value	Axial force (kN)	Shear force (kN)	Transv. shear force (kN)	Torque (kN.m)	Bending moment (kN.m)	Transv. bending moment (kN.m)
Deck in suspension segment	Min.	**-40 372**	-9653	-5653	-25 010	-740 328	**-596 620**
	Max.	**219 572**	-4379	4607	16 338	**780 449**	-25 043
Deck in cable-stayed segment of center span (North)	Min.	**-62 369**	16 935	-8367	-20 549	-677 272	**-669 938**
	Max.	**194 404**	27 122	6816	21 500	**716 702**	-283 811
Deck in cable-stayed segment of center span (South)	Min.	**-50 134**	-27 036	-6096	-24 567	**-681 177**	**-927 370**
	Max.	**209 271**	-15 902	7425	24 887	664 226	-429 771

Table 6.18. Envelope internal force resultant values at critical sections (cont'd.)

Section	Envelope value	Axial force (kN)	Shear force (kN)	Transv. shear force (kN)	Torque (kN.m)	Bending moment (kN.m)	Transv. bending moment (kN.m)
Deck side span (North)	Min.	**-41 605**	-9615	-7919	-8492	**-546 407**	-13 725
	Max.	**221 917**	-4642	6519	6351	515 935	**322 620**
Deck side span (South)	Min.	**-256 307**	-1149	-9841	-34 322	**-832 677**	16 847
	Max.	**11 685**	1239	7280	34 863	415 559	**205 715**
Tower leg (at base)	Min.	**-1 143 445**	-14 050	-4550	-178 762	**-1 135 009**	**-1 074 285**
	Max.	**-886 355**	16 565	18 607	112 979	260 163	608 594
Suspension cable	Min.	570 446	0				
	Max.	**809 726**	0				
Stay cable	Min.	6722	0				
	Max.	**9316**	0				

6.6. Design Capacity Checks for Bridge Components

Envelopes of the analysis results presented in the previous section for the selected strength and extreme event load combinations were compared with member capacities calculated according to the AASHTO-LRFD specifications described in Section 4.8.2, for strength-based design assessment of the bridge. The design capacity checks were performed for the cable-stayed and suspended segments of the bridge deck under combined axial compression and flexure as well as combined axial tension and flexure; the bridge tower legs under combined axial compression and flexure; and the suspension and stay cables under axial tension.

In calculation of the compressive resistance of the deck and the tower legs, certain assumptions were made related to the unbraced length (l) and the effective length factor (K) values, as described below.

For the tower legs, the buckling mode was assumed to be controlled by buckling in the longitudinal direction of the bridge (about the transverse axis), since the tower cross beams provided portal bracing in the transverse direction. The unbraced length of the tower legs were assumed to be l = 325 meters, which is the distance from the base of each tower leg to the elevation where it is connected to the lowermost stay cable. The effective length factor was taken as K=0.7, corresponding to a fixed boundary at the bottom and a pinned boundary at the top.

For the cable-stayed segments of the bridge deck, considering buckling in the transverse direction of the deck (about the vertical axis), the unbraced length of the deck was assumed to be l = 630 meters, which is the entire length of the cable-stayed deck segment. This value was assumed due to the symmetrical buckling mode of the cable stayed deck segments with respect to the plane of the towers. Each tower plane was therefore assumed to be a fixed boundary, and an effective length factor of K = 2.0 was used for the cable-supported deck segments.

For the suspension segments of the bridge deck, considering buckling in the transverse direction of the deck (about the vertical axis), the unbraced length of the deck was assumed to be l = 1140 meters, which is the entire length of the suspended deck segment, and an effective length factor of K = 1.0 was used, assuming that the suspended deck is pinned at both ends.

For the both the cable stayed and the suspension segments of the bridge deck, considering buckling in the vertical direction of the deck (about the transverse axis), the unbraced length of the cable-stayed and suspension segments were assumed to be the distances between the stay cable connections and the hanger connections, respectively. Therefore, the unbraced length of the cable stayed deck segment was taken as l = 35 meters, whereas the unbraced length of the suspended deck segment was taken as l = 16 meters. An effective length factor of K = 1.0 was used for both cases.

Accordingly, the design capacity checks conducted are described in the following subsections.

6.6.1. Cable Stayed Deck Segments under Combined Axial Compression and Flexure

Considering buckling in the transverse direction (about the vertical axis), (AASHTO LRFD 2007, Section 6, Article 6.9.4.1):

$$\lambda = \left(\frac{Kl}{r_s \pi}\right)^2 \frac{F_y}{E} = \left(\frac{2\times(630000)}{(10.38\times10^3)\times\pi}\right)^2 \times \frac{485}{2.06\times10^5} = 3.51 > 2.25 \qquad (6.1)$$

λ : normalized column slenderness factor

F_y : specified minimum yield strength (MPa)

E : modulus of elasticity (MPa)

l : unbraced length (mm)

r_s : radius of gyration about the plane of buckling (mm)

K : effective length factor

A_s : gross cross sectional area (mm^2)

P_n = nominal compressive resistance, as calculated below (AASHTO LRFD 2007, Article 6.9.4.1):

If $\lambda \le 2.25$, $P_n = 0.66^{\lambda} F_y A_s$ (6.2)

If $\lambda > 2.25$, $P_n = \dfrac{0.88 F_y A_s}{\lambda}$ (6.3)

Since $\lambda > 2.25$,

$$P_n = \frac{0.88 F_y A_s}{\lambda} = \frac{0.88\times485\times(3.274\times10^6)}{3.51} = 398103kN \qquad (6.4)$$

According to AASHTO LRFD 2007 Section 6, Article 6.9.2.1, the factored resistance of components in compression, P_r, is calculated as:

$$P_r = \phi_c P_n = 0.90\times398103 = 358293kN \qquad (6.5)$$

where, ϕ_c = resistance factor for compression ($\phi_c = 0.90$)

Considering buckling in the vertical direction (about the transverse deck axis),

$$\lambda = \left(\frac{Kl}{r_s \pi}\right)^2 \frac{F_y}{E} = \left(\frac{2\times(35000)}{(1.71\times10^3)\times\pi}\right)^2 \times \frac{485}{2.06\times10^5} = 0.100 \le 2.25 \tag{6.6}$$

Since $\lambda \le 2.25$;

$$P_n = 0.66^{\lambda} F_y A_s = 0.66^{0.100} \times 485 \times 3.274 \times 10^6 = 1\ 523\ 313 kN \tag{6.7}$$

$$P_r = \phi_c P_n = 0.90 \times 1523313 = 1\ 370\ 982 kN \tag{6.8}$$

Therefore, the design compressive capacity was obtained as $P_r = 358293 kN$.

The axial compression, P_u, and concurrent moments, M_{ux} and M_{uy}, were selected as critical combinations of the envelope values listed in Table 6.18, as P_u = 256307 kN, M_{ux} = 832677 kN.m, and M_{uy} = 322620 kN.m.

The factored flexural resistance values were determined using Equation 6.7 for box shaped members, where the parameters in the equation were defined in Section 4.8.2. Values of M_{rx} = 14280514 kN.m and M_{ry} = 2551066 kN.m were calculated using the equation (AASHTO LRFD 2007, Section 6, Article 6.12.2.2.2).

$$M_n = \phi_f F_y S \left[1 - \frac{0.064 F_y S l}{AE}\left(\frac{\sum\left(\frac{b}{t}\right)}{I_y}\right)^{0.5}\right] \tag{6.9}$$

M_{rx} : factored flexural resistance about the x-axis, taken equal to ϕ_f times the nominal flexural resistance (M_{nx}) about the x-axis (N.mm).

M_{ry} : factored flexural resistance about the x-axis, taken equal to ϕ_f times the nominal flexural resistance (M_{ny}) about the x-axis (N.mm).

ϕ_f : resistance factor for flexure (ϕ_f =1.0).

The design capacity was checked using Equation 6.10, indicating that the design capacity of cable stayed deck segments under combined axial compression and flexure, is adequate (AASHTO LRFD 2007, Section 6, Article 6.9.2.2).

$$\frac{P_u}{P_r}+\frac{8.0}{9.0}\left(\frac{M_{ux}}{M_{rx}}+\frac{M_{uy}}{M_{ry}}\right)=\frac{256307}{358293}+\frac{8.0}{9.0}\left(\frac{832677}{14280514}+\frac{322620}{2551066}\right)=0.88\le 1.0 \qquad (6.10)$$

6.6.2. Suspended Deck Segments under Combined Axial Compression and Flexure

Considering buckling in the transverse direction (about the vertical axis), (AASHTO LRFD 2007, Section 6, Article 6.9.4.1):

$$\lambda=\left(\frac{Kl}{r_s\pi}\right)^2\frac{F_y}{E}=\left(\frac{1\times(1100000)}{(10.38\times10^3)\times\pi}\right)^2\times\frac{485}{2.06\times10^5}=2.67>2.25 \qquad (6.11)$$

Since $\lambda > 2.25$,

$$P_n=\frac{0.88F_yA_s}{\lambda}=\frac{0.88\times485\times(3.274\times10^6)}{2.67}=523350kN \qquad (6.12)$$

According to AASHTO LRFD Section 6, Article 6.9.2.1, the factored resistance of components in compression, P_r, is calculated as:

$$P_r=\phi_cP_n=0.90\times523350=471\,015kN \qquad (6.13)$$

Considering buckling in the vertical direction (about the transverse deck axis), (AASHTO LRFD 2007, Section 6, Article 6.9.4.1)

$$\lambda = \left(\frac{Kl}{r_s \pi}\right)^2 \frac{F_y}{E} = \left(\frac{1\times(16000)}{(1.71\times10^3)\times\pi}\right)^2 \times \frac{485}{2.06\times10^5} = 0.020 \le 2.25 \quad (6.14)$$

$$P_n = 0.66^{\lambda} F_y A_s = 0.66^{0.020} \times 485 \times (3.274\times10^6) = 1574748\ kN \quad (6.15)$$

$$P_r = \phi_c P_n = 0.90\times1574748 = 1417273kN \quad (6.16)$$

Therefore, the design compressive capacity was obtained as $P_r = 1417273kN$.

The axial compression, P_u, and concurrent moments, M_{ux} and M_{uy}, were selected as critical combinations of the envelope values listed in Table 6.18, as P_u = 40372 kN, M_{ux} = 780449 kN.m, and M_{uy} = 596620 kN.m.

The factored flexural resistance values were determined using Equation 6.9, as M_{rx} = 14283178 kN.m and M_{ry} = 2551066 kN.m.

The design capacity was checked using Equation 6.17, indicating that the design capacity of suspended deck segments under combined axial compression and flexure, is adequate (AASHTO LRFD 2007, Section 6, Article 6.9.2.2).

$$\frac{P_u}{2.0P_r} + \left(\frac{M_{ux}}{M_{rx}} + \frac{M_{uy}}{M_{ry}}\right) = \frac{40372}{2\times(1417273)} + \left(\frac{780449}{14\ 283\ 178} + \frac{596620}{2\ 551\ 095}\right) = 0.43 < 1.0 \quad (6.17)$$

6.6.3. Bridge Tower Legs under Combined Axial Compression and Flexure

Considering the buckling mode in the longitudinal direction of the bridge only, (AASHTO LRFD 2007, Section 6, Article 6.9.4.1):

$$\lambda = \left(\frac{Kl}{r_s \pi}\right)^2 \frac{F_y}{E} = \left(\frac{0.7\times325000}{4.0\times10^3\times\pi}\right)^2 \times \frac{690}{2.06\times10^5} = 1.09 < 2.25 \quad (6.18)$$

$$P_n = 0.66^{\lambda} F_y A_s = 0.66^{1.09} \times 690 \times (3.87 \times 10^6) = 1697709\ kN \quad (6.19)$$

According to AASHTO LRFD Section 6, Article 6.9.2.1, the factored resistance of components in compression, P_r, is calculated as:

$$P_r = \phi_c P_n = 0.90 \times 1697709 = 1527940 kN \quad (6.20)$$

The axial compression, P_u, and concurrent moments, M_{ux} and M_{uy}, were selected as critical combinations of the envelope values listed in Table 6.18, as P_u = 1143445 kN, M_{ux} = 1135009 kN.m, and M_{uy} = 1074285 kN.m.

The factored flexural resistance values were determined using Equation 6.9, as $M_{rx} \approx M_{ry}$ = 8475303 kN.m.

The design capacity was checked using Equation 6.21, indicating that the design capacity of the bridge tower legs under combined axial compression and flexure, is adequate (AASHTO LRFD, Section 6, Article 6.9.2.2).

$$\frac{P_u}{P_r} + \frac{8.0}{9.0}\left(\frac{M_{ux}}{M_{rx}} + \frac{M_{uy}}{M_{ry}}\right) = \frac{1143445}{1527940} + \frac{8.0}{9.0}\left(\frac{1135009}{8475303} + \frac{1074285}{8475303}\right) = 0.98 \le 1.0 \quad (6.21)$$

6.6.4. Cable Stayed Deck Segments under Combined Axial Tension and Flexure

The design tensile resistance of the segments was calculated as, (AASHTO LRFD 2007, Section 6, Article 6.8.2.1):

$$P_r = \phi_y P_{ny} = \phi_y F_y A_g = 0.95 \times 485 \times 3.274 \times 10^6 = 1508495 kN \quad (6.22)$$

The axial tension, P_u, and concurrent moments, M_{ux} and M_{uy}, were selected as critical combinations of the envelope values listed in Table 6.18, as P_u = 221918 kN, M_{ux} = 515934 kN.m, and M_{uy} = 322620 kN.m.

The factored flexural resistance values were determined using Equation 6.9, as M_{rx} = 14283178 kN.m and M_{ry} = 2551066 kN.m.

The design capacity was checked using Equation 6.23, indicating that the design capacity of cable stayed deck segments under combined axial tension and flexure, is adequate (AASHTO LRFD 2007, Section 6, Article 6.8.2.3).

$$\frac{P_u}{2.0P_r}+\left(\frac{M_{ux}}{M_{rx}}+\frac{M_{uy}}{M_{ry}}\right)=\frac{221918}{2.0\times(1508495)}+\left(\frac{515934}{14280514}+\frac{322620}{2551066}\right)=0.24<1.0 \quad (6.23)$$

6.6.5. Suspended Deck Segments under Combined Axial Tension and Flexure

The design tensile resistance of the segments was calculated as (AASHTO LRFD 2007, Section 6, Article 6.8.2.1):

$$P_r=\phi_y P_{ny}=\phi_y F_y A_g=0.95\times 485\times 3.274\times 10^6=1508495kN \quad (6.24)$$

The axial tension, P_u, and concurrent moments, M_{ux} and M_{uy}, were selected as critical combinations of the envelope values listed in Table 6.18, as P_u = 219572 kN, M_{ux} = 780449 kN.m, and M_{uy} = 596620 kN.m.

The factored flexural resistance values were determined using Equation 6.9, as M_{rx} = 14283178 kN.m and M_{ry} = 2551066 kN.m.

The design capacity was checked using Equation 6.25, indicating that the design capacity of cable stayed deck segments under combined axial tension and flexure, is adequate (AASHTO LRFD 2007, Section 6, Article 6.8.2.3).

$$\frac{P_u}{2.0P_r}+\left(\frac{M_{ux}}{M_{rx}}+\frac{M_{uy}}{M_{ry}}\right)=\frac{219572}{2.0\times 1508495}+\left(\frac{780449}{14280514}+\frac{596620}{2551066}\right)=0.37<1.0 \quad (6.25)$$

6.6.6. Suspension Cables under Axial Tension

Suspension cable wires cross sectional and material properties were selected from manufacturer's catalogue ASTM A416. Nominal diameter of the cable wire is 15.24mm and tensile strength is specified as 1860 MPa. Suspension cable diameters at main span and side span are 1.2 meter and 1.3 meter respectively.

The design tensile strength of the suspension cables was calculated as (AASHTO LRFD 2007, Section 6, Article 6.8.2.1):

$$P_r = \phi_y P_{ny} = \phi_y F_y A_g = 0.95 \times 1860 \times 1.327 \times 10^6 = 2344809kN \quad (6.26)$$

The axial tension, P_u, was selected as the maximum envelope value listed in Table 6.18, as P_u = 809 726 kN.

The design capacity was checked using Equation 6.26, indicating that the capacity of the suspension cables under axial tension is adequate.

6.6.7. Stay Cables under Axial Tension

Stay cable wires cross sectional and material properties were selected from manufacturer's catalogue ASTM A416. Nominal diameter of the cable wire is 15.24mm and tensile strength is specified as 1860 MPa. Stay cable diameter was selected as 0.15m.

The design tensile strength of the suspension cables was calculated as (AASHTO LRFD 2007, Section 6, Article 6.8.2.1):

$$P_r = \phi_y P_{ny} = \phi_y F_y A_g = 0.95 \times 1860 \times 0.0177 \times 10^6 = 31276kN \quad (6.27)$$

The axial tension, P_u, was selected as the maximum envelope value listed in Table 6.18, as P_u = 9316 kN.

The design capacity was checked using Equation 6.27, indicating that the capacity of the stay cables under axial tension is adequate (AASHTO LRFD 2007, Section 6, Article 6.8.2.1).

6.7. Deflection Calculations for the Serviceability Limit State

The analysis results obtained for displacements and rotations at critical locations of the bridge, corresponding to the service load combination limit state in AASHTO-LRFD, are listed in Table 6.19. The values in the table can be compared with deflection limits, for assessment of the serviceability conditions of the bridge. Although deflection limits for serviceability are not typically enforced in design code specifications, general recommendations can be used for this purpose.

It is recommended in the AASHTO-LRFD 2007, Section 2, Article 2.5.2.6.2 that the deflection at the mid-span of a long-span bridge structure should not exceed 1/300'th of the span length. The midspan deflection of the bridge is approximately 1/600'th of the span length, indicating favorable serviceability conditions.

Table 6.19. Maximum displacements and rotations at critical locations

Location	Loading limit state	Max disp. in long. bridge direction (m)	Max. disp. in transv. bridge direction (m)	Max. disp. in vertical direction (m)	Max. rotation about long. bridge axis (rad)	Max. rotation about transv. bridge axis (rad)	Max. rotation about vertical axis (rad)
Deck midspan	SERVICE	-0.0038	-0.0349	**-3.9298**	-0.00004	0.0003	-0.0001
Deck in cable-stayed segment of main span	SERVICE	-0.1552	0.1347	**-0.9624**	-0.00048	-0.0271	0.00002
Deck side span	SERVICE	0.0262	-0.0673	-0.5543	0.00086	-0.0030	-0.0008
Tower top	SERVICE	0.0023	**1.7657**	-0.8357	0.00049	0.0157	0.0002
Tower-deck connection	SERVICE	-0.0668	0.0016	-0.1532	-0.0000	0.0016	-0.0003

7. SUMMARY AND CONCLUSIONS

7.1. Overview

In this analytical study, a three-dimensional structural model was developed for the analysis and design of a possible combined cable-stayed suspension (CSS) hybrid bridge configuration spanning across the Izmit Bay. Sources of geometric nonlinearity were incorporated in the bridge model. The model was first analyzed under dead loads and pretension effects on the cables, for determination of its initial equilibrium configuration; followed by code-compliant moving live loads, aerostatic wind loads, temperature changes, and dynamic earthquake actions. For earthquake response assessment of the bridge, nonlinear time-history analysis and response spectrum analysis methods were both utilized. Results of the analyses were evaluated, and the internal forces developing in structural components were compared with AASHTO-LRFD member capacities for assessment of the performance of the proposed Izmit Bay bridge configuration, considering both strength and serviceability limit states.

The Bosphorus suspension bridge in Istanbul was also modeled and analyzed within the scope of this work, as a preliminary case study to assess the validity of the modeling and analysis methodologies used.

7.2. Conclusions

The following conclusions can be reached on the basis of the results of this analytical study:

- Reaching the initial equilibrium configuration of a cable supported bridge, via a set of geometrically-nonlinear analysis under dead loads, is essential in obtaining the stiffness properties of the cable elements for further analyses. In order to reach an optimum initial equilibrium configuration, where the deformation of the suspended bridge deck is minimal, a very efficient methodology is to impose

initial shortening effects on the cable elements, through a trial-and-error procedure.

- In determining the earthquake response of a cable-supported bridge, the reliability of the response spectrum analysis method is questionable. For such complex three dimensional systems with numerous closely spaced and coupled modes of vibration, caution should be used in utilizing the response spectrum method, using a code-specified design response spectrum in particular. Conducting nonlinear time history analyses of a cable-supported bridge under multiple ground acceleration records would provide much more reliable earthquake response predictions, compared to the results of a response spectrum analysis.

- The analysis results obtained using the model created for the Bosphorus bridge are consistent with previous experimental and analytical studies conducted on the bridge, as well as the analysis results reported in the design documents; validating the structural modeling approach, loading types, and the analysis methods used in this study.

- The simple design capacity checks performed on the main structural components of the Izmit Bay bridge under both strength and extreme event load limit states, as well as calculated deformations of the bridge under the serviceability load limit state, indicate that the proposed structural configuration of the bridge, the material grades used in the design, and the general cross-sectional attributes selected for the structural components of the bridge are adequate. The combined cable-stayed and suspension configuration of the bridge proposed in this study, is presented as a feasible general layout which can assist in the detailed design of the Izmit Bay Bridge.

APPENDIX A: AASHTO LRFD BRIDGE DESIGN SPECIFICATIONS

The following sample portion of the Specifications Section 6, Article 6.8 and Article 6.9 is an extract from AASHTO LRFD (2007), supplementing the information contained in Chapter 6.

R = radius of curvature (mm)

L = span length for simple spans or for continuous spans, the distance between a simple end support and the permanent load contraflexure point, or the distance between points of permanent load contraflexure (mm)

Camber loss between permanent load contraflexure points adjacent to piers is small and may be neglected.

6.8 TENSION MEMBERS

6.8.1 General

Members and splices subjected to axial tension shall be investigated for:

- Yield on the gross section, e.g., Eq. 6.8.2.1-1, and
- Fracture on the net section, e.g., Eq. 6.8.2.1-2.

The determination of the gross section shall require consideration of all holes larger than those typically used for connectors such as bolts.

The determination of the net section shall require consideration of:

- The gross area from which deductions will be made or reduction factors applied, as appropriate;
- Deductions for all holes in the design cross-section;
- Correction of the bolt hole deductions for the stagger rule specified in Article 6.8.3;
- Application of the reduction factor U specified in Article 6.8.2.2 for members and Article 6.13.5.2 for splice plates and other splicing elements to account for shear lag; and
- Application of the 85-percent maximum area efficiency factor for splice plates and other splicing elements specified in Article 6.13.5.2.

Tension members shall satisfy the slenderness requirements specified in Article 6.8.4 and the fatigue requirements of Article 6.6.1. Block shear strength shall be investigated at end connections as specified in Article 6.13.4.

C6.8.1

Holes typically deducted where determining the gross section include pin holes, access holes and perforations.

The provisions of the AISC (*2005*) may be used to design tapered tension members.

© 2007 by the American Association of State Highway and Transportation Officials.
All rights reserved. Duplication is a violation of applicable law.

6.8.2 Tensile Resistance

6.8.2.1 General

The factored tensile resistance, P_r, shall be taken as the lesser of the values given by Eqs. 1 and 2.

$$P_r = \phi_y P_{ny} = \phi_y F_y A_g \quad (6.8.2.1\text{-}1)$$

$$P_r = \phi_u P_{nu} = \phi_u F_u A_n U \quad (6.8.2.1\text{-}2)$$

where:

P_{ny} = nominal tensile resistance for yielding in gross section (N)

F_y = specified minimum yield strength (MPa)

A_g = gross cross-sectional area of the member (mm^2)

P_{nu} = nominal tensile resistance for fracture in net section (N)

F_u = tensile strength (MPa)

A_n = net area of the member as specified in Article 6.8.3 (mm^2)

U = reduction factor to account for shear lag; 1.0 for components in which force effects are transmitted to all elements, and as specified in Article 6.8.2.2 for other cases

ϕ_y = resistance factor for yielding of tension members as specified in Article 6.5.4.2

ϕ_u = resistance factor for fracture of tension members as specified in Article 6.5.4.2

C6.8.2.1

The reduction factor, U, does not apply when checking yielding on the gross section because yielding tends to equalize the nonuniform tensile stresses caused over the cross-section by shear lag.

Due to strain hardening, a ductile steel loaded in axial tension can resist a force greater than the product of its gross area and its yield strength prior to fracture. However, excessive elongation due to uncontrolled yielding of gross area not only marks the limit of usefulness but can precipitate failure of the structural system of which it is a part. Depending on the ratio of net area to gross area and the mechanical properties of the steel, the component can fracture by failure of the net area at a load smaller than that required to yield the gross area. General yielding of the gross area and fracture of the net area both constitute measures of component strength. The relative values of the resistance factors for yielding and fracture reflect the different reliability indices deemed proper for the two modes.

The part of the component occupied by the net area at fastener holes generally has a negligible length relative to the total length of the member. As a result, the strain hardening is quickly reached and, therefore, yielding of the net area at fastener holes does not constitute a strength limit of practical significance, except perhaps for some builtup members of unusual proportions.

For welded connections, A_n is the gross section less any access holes in the connection region.

6.8.2.2 Reduction Factor, *U*

In the absence of more refined analysis or tests, the reduction factors specified herein may be used to account for shear lag in connections.

The reduction factor, U, for sections subjected to a tension load transmitted directly to each of the cross-sectional elements by bolts or welds may be taken as:

$$U = 1.0$$

For bolted connections, the following values of U may be used:

C6.8.2.2

The provisions of Article 6.8.2.2 are adapted from the commentary to the 1999 AISC LRFD Specification, Article B3, Effective Net Area for Tension Members. Similar simple provisions appear in previous issues of the AISC LRFD Specification prior to 1993, but were replaced in the 1993 edition by a more precise equation for shear-lag effects, Equation B3-3. The 1999 AISC LRFD Commentary suggests that the complication and preciseness of Equation B3-3 is not warranted for design.

© 2007 by the American Association of State Highway and Transportation Officials.
All rights reserved. Duplication is a violation of applicable law.

- For rolled I-shapes with flange widths not less than two-thirds the depth, and structural tees cut from these shapes, provided the connection is to the flanges and has no fewer than three fasteners per line in the direction of stress,

  $U = 0.90$

- For all other members having no fewer than three fasteners per line in the direction of stress,

  $U = 0.85$

- For all members having only two fasteners per line in the direction of stress,

  $U = 0.75$

When a tension load is transmitted by fillet welds to some, but not all, elements of a cross-section, the weld strength shall control.

6.8.2.3 Combined Tension and Flexure

A component subjected to tension and flexure shall satisfy Eqs. 1 or 2.

$$\text{If } \frac{P_u}{P_r} < 0.2, \text{ then}$$

$$\frac{P_u}{2.0\,P_r} + \left(\frac{M_{ux}}{M_{rx}} + \frac{M_{uy}}{M_{ry}}\right) \le 1.0 \qquad (6.8.2.3\text{-}1)$$

$$\text{If } \frac{P_u}{P_r} \ge 0.2, \text{ then}$$

$$\frac{P_u}{P_r} + \frac{8.0}{9.0}\left(\frac{M_{ux}}{M_{rx}} + \frac{M_{uy}}{M_{ry}}\right) \le 1.0 \qquad (6.8.2.3\text{-}2)$$

where:

P_r = factored tensile resistance as specified in Article 6.8.2.1 (N)

M_{rx} = factored flexural resistance about the x-axis taken as ϕ_f times the nominal flexural resistance about the x-axis determined as specified in Article 6.10, 6.11 or 6.12, as applicable (N-mm)

M_{ry} = factored flexural resistance about the y-axis taken as ϕ_f times the nominal flexural resistance about the y-axis determined as specified in Article 6.12, as applicable (N-mm)

C6.8.2.3

Interaction equations in tension and compression members are a design simplification. Such equations involving exponents of 1.0 on the moment ratios are usually conservative. More exact, nonlinear interaction curves are also available and are discussed in Galambos (*1998*). If these interaction equations are used, additional investigation of service limit state stresses is necessary to avoid premature yielding.

For sections where the nominal flexural resistance about the x-axis is expressed in terms of stress, the factored flexural resistance about the x-axis in Eqs. 1 and 2 should be taken as:

$$M_{rx} = \text{the smaller of } \phi_f F_{nc} S_{xc} \text{ and } \phi_f F_{nt} S_{xt} \qquad (C6.8.2.3\text{-}1)$$

where:

F_{nc} = nominal flexural resistance of the compression flange (MPa)

F_{nt} = nominal flexural resistance of the tension flange (MPa)

M_{yc} = yield moment with respect to the compression flange determined as specified in Article D6.2 (N-mm)

M_{yt} = yield moment with respect to the tension flange determined as specified in Article D6.2 (N-mm)

S_{xc} = elastic section modulus about the major axis of the section to the compression flange taken as M_{yc}/F_{yc} (mm^3)

© 2007 by the American Association of State Highway and Transportation Officials.
All rights reserved. Duplication is a violation of applicable law.

M_{ux}, M_{uy} = moments about the x- and y-axes, respectively, resulting from factored loads (N-mm)

P_u = axial force effect resulting from factored loads (N)

ϕ_f = resistance factor for flexure specified in Article 6.5.4.2

The stability of a flange subjected to a net compressive stress due to the tension and flexure shall be investigated for local buckling.

6.8.3 Net Area

The net area, A_n, of an element is the product of the thickness of the element and its smallest net width. The net area, A_n, of a member is the sum of the net areas of each element. The width deducted for all holes; standard, oversize, and slotted; shall be taken as 2 mm greater than the hole size specified in Article 6.13.2.4.2. The net width shall be determined for each chain of holes extending across the member or element along any transverse, diagonal, or zigzag line.

The net width for each chain shall be determined by subtracting from the width of the element the sum of the widths of all holes in the chain and adding the quantity $s^2/4g$ for each space between consecutive holes in the chain, where:

s = pitch of any two consecutive holes (mm)

g = gage of the same two holes (mm)

For angles, the gage for holes in opposite adjacent legs shall be the sum of the gages from the back of the angles less the thickness.

S_{xt} = elastic section modulus about the major axis of the section to the tension flange taken as M_{yt}/F_{yt} (mm^3)

S_{xc} and S_{xt} are defined in this fashion as equivalent values that account for the combined effects of the loads acting on different sections in composite members.

For sections where the nominal flexural resistance about the x-axis is determined according to the provisions of Appendix A6, the factored flexural resistance about the x-axis should be taken as:

$$M_{rx} = \text{the smaller of } \phi_f M_{nc} \text{ and } \phi_f M_{nt} \qquad \text{(C6.8.2.3-2)}$$

where:

M_{nc} = nominal flexural resistance based on the compression flange (N-mm)

M_{nt} = nominal flexural resistance based on the tension flange (N-mm)

For I- and H-shaped sections, the nominal flexural resistance about the y axis is determined according to the provisions of Article 6.12.2.2.1.

C6.8.3

In the metric bolt standard, the hole size for standard holes is 2 mm larger than the bolt diameter for 24 mm and smaller bolts, and 3 mm larger than the bolt diameter for bolts larger than 24 mm in diameter. Thus, a constant width increment of 3.2 mm applied to the bolt diameter will not work. Also, the deduction should be 2 mm and not 1.6 mm (the soft conversion) since metric tapes and rulers are not read to less than 1 mm.

The development of the "$s^2/4g$" rule for estimating the effect of a chain of holes on the tensile resistance of a section is described in McGuire (*1968*). Although it has theoretical shortcomings, it has been used for a long time and has been found to be adequate for ordinary connections.

In designing a tension member, it is conservative and convenient to use the least net width for any chain together with the full tensile force in the member. It is sometimes possible to achieve an acceptable, slightly less conservative design by checking each possible chain with a tensile force obtained by subtracting the force removed by each bolt ahead of that chain, i.e., closer to midlength of the member from the full tensile force in the member. This approach assumes that the full force is transferred equally by all bolts at one end.

© 2007 by the American Association of State Highway and Transportation Officials.
All rights reserved. Duplication is a violation of applicable law.

6.9 COMPRESSION MEMBERS

6.9.1 General

The provisions of this Article shall apply to prismatic noncomposite and composite steel members with at least one plane of symmetry and subjected to either axial compression or combined axial compression and flexure about an axis of symmetry.

Arches shall also satisfy the requirements of Article 6.14.4.

Compression chords of half-through trusses shall also satisfy the requirements of Article 6.14.2.9

C6.9.1

Conventional column design formulas contain allowances for imperfections and eccentricities permissible in normal fabrication and erection. The effect of any significant additional eccentricity should be accounted for in bridge design.

Torsional buckling or flexural-torsional buckling of singly symmetric and unsymmetric compression members and doubly-symmetric compression members with very thin walls should be investigated. Pertinent provisions of AISC (*1999*) can be used to design tapered compression members.

6.9.2 Compressive Resistance

6.9.2.1 Axial Compression

The factored resistance of components in compression, P_r, shall be taken as:

$$P_r = \phi_c P_n \qquad (6.9.2.1\text{-}1)$$

where:

P_n = nominal compressive resistance as specified in Articles 6.9.4 or 6.9.5, as applicable (N)

ϕ_c = resistance factor for compression as specified in Article 6.5.4.2

6.9.2.2 Combined Axial Compression and Flexure

The axial compressive load, P_u, and concurrent moments, M_{ux} and M_{uy}, calculated for the factored loadings by elastic analytical procedures shall satisfy the following relationship:

- If $\frac{P_u}{P_r} < 0.2$, then:

$$\frac{P_u}{2.0P_r} + \left(\frac{M_{ux}}{M_{rx}} + \frac{M_{uy}}{M_{ry}}\right) \le 1.0 \qquad (6.9.2.2\text{-}1)$$

C6.9.2.2

These equations are identical to the provisions in AISC (*2005*). They were selected for use in that Specification after being compared with a number of alternative formulations with the results of refined inelastic analyses of 82 frame sidesway cases (*Kanchanalai, 1977*). P_u, M_{ux}, and M_{uy} are simultaneous axial and flexural forces on cross-sections determined by analysis under factored loads. The maximum calculated moment in the member in each direction including the second order effects, should be considered. Where maxima occur on different cross-sections, each should be checked.

© 2007 by the American Association of State Highway and Transportation Officials.
All rights reserved. Duplication is a violation of applicable law.

- If $\frac{P_u}{P_r} \geq 0.2$, then:

$$\frac{P_u}{P_r} + \frac{8.0}{9.0}\left(\frac{M_{ux}}{M_{rx}} + \frac{M_{uy}}{M_{ry}}\right) \leq 1.0 \qquad (6.9.2.2\text{-}2)$$

where:

P_r = factored compressive resistance as specified in Article 6.9.2.1 (N)

M_{rx} = factored flexural resistance about the x-axis taken equal to ϕ_f times the nominal flexural resistance about the x-axis determined as specified in Article 6.10, 6.11 or 6.12, as applicable (N-mm)

M_{ry} = factored flexural resistance about the y-axis taken equal to ϕ_f times the nominal flexural resistance about the y-axis determined as specified in Article 6.12, as applicable (N-mm)

M_{ux} = factored flexural moment about the x-axis calculated as specified below (N-mm)

M_{uy} = factored flexural moment about the y-axis calculated as specified below (N-mm)

ϕ_f = resistance factor for flexure specified in Article 6.5.4.2

M_{ux} and M_{uy}, moments about axes of symmetry, may be determined by:

- A second-order elastic analysis that accounts for the magnification of moment caused by the factored axial load, or
- The approximate single step adjustment specified in Article 4.5.3.2.2b.

For further information on computing the factored flexural resistances about the x- and y-axes, refer to Article C6.8.2.3.

© 2007 by the American Association of State Highway and Transportation Officials.
All rights reserved. Duplication is a violation of applicable law.

REFERENCES

Abdel-Ghaffar A.M., A.S. Nazmy, 1991, "3-D Nonlinear Seismic Behavior of Cable-Stayed Bridge", *Journal of Structural Engineering*, ASCE, Vol. 117, pp. 3456-3476.

AASHTO LRFD, 2007, *Bridge Design Specifications*, SI Units, American Association of State Highway and Transportation Officials, USA.

AC1-307, 1988, "Standard Practice for the Design and Construction of Castin-Place Reinforced Concrete Chimneys (ACI 307-88) and Commentary (ACt 307R-88)", *American Concrete Institute*, Detroit, MI.

Adeli, H., and J. Zhang, 1995, ''Fully Nonlinear Analysis of Composite Girder Cable-Stayed Bridges'', *Computers and Structures*, Vol. 54, No. 2, pp. 267-277.

Al-Assaf, A., 2006, *Flutter Analysis of Open-Truss Stiffened Suspension Bridges Using Synthesized Aerodynamic Derivatives*, Ph.D. Dissertation, Washington State University, USA.

Amornvivat, P., 1996, *Optimal Designs for Cable-Stayed Bridge*, M.S. Thesis, Massachusetts Institute of Technology, Cambridge, USA.

Baron, F., and M. Venkatesan, 1971, ''Nonlinear Analysis of Cable and Truss Structures", *Journal of the Structural Division*, Vol. 97, No. 2, pp. 679-710, February.

Baron, F. And S.Y. Lien, 1973, "Analytical Studies of a Cable Stayed Girder Bridge", *Computers and Structures*, Vol. 3, No. 3, pp. 443-463.

Bathe, K. J., and S. Bolourchi, 1979, ''Large Displacement Analysis of Three-Dimensional Beam Structures'', *International Journal for Numerical Methods in Engineering*, Vol. 14 , No. 7, pp. 961-986, June.

Bernardo, S., 1998, *Motion Based Design of Cable-Stayed Bridges*, MSc Dissertation, Massachusetts Institute of Technology, Cambridge, USA.

Bessas, G., 2006, *Design Optimization of Cable-Stayed Bridges*, MSc Thesis, Georgios Massachusetts Institute of Technology.

Boonyapinyo, V., H. Yamada, and T. Miyata, 1994, ‘‘Nonlinear Structural Instability of Long-Span Cable-Stayed Bridges under Gravity and Wind Loads’’, *Journal of the Structural Engineering*, Vol. 40A, pp. 295-308, March.

Box, G.E.P., and G.M. Jenkins, G.C.Reinsel, 1994, *Time Series Analysis: Forecasting and Control*, New Jersey: Prentice Hall.

Brown, W.C., F. Parsons and H.S.G. Knox, 1976, *Bosporus Bridge*, William Clowes & Sons, London.

Brownjohn JMW, and A. Dumanoglu , and T. Severn, and A. Blakeborough, 1989, “Ambient Vibration Survey of the Bosporus Suspension Bridge”, *Earthquake Engineering and StructuralDynamics*, Vol. 18, pp. 263-283, July.

CICIND, 1984, “Model Code for Concrete Chimneys Part A: The Shell”, *Comite International Des Chimnees Industrielle*, Zurich.

Chang, S.P. and J.I. Park, 1989, “A Study on the Nonlinear Finite Cable Elements” *Journal of Korean Society of Coastal and Ocean Engineers*, Vol. 1, No. 1, pp. 93-101.

Chang, C.C. and P. Chang, and Q.W. Zhang, 2001, “Ambient Vibration of Long-Span Cable-Stayed Bridge”, *Journal of Bridge Engineering*, ASCE, Vol. 6, No.1, pp. 46-53, January/February.

Commercial Office Space News, 2010, *Brooklyn Bridge Photo*, http://www.office-suites.com/commercialnews/wp-content/uploads/2010/03/brooklyn-bridge.jpg

Como, M., 1985, ‘‘Static Behavior of Long Span Cable-Stayed Bridges’’, *International Journal of Solids and Structures*, Vol. 21, No. 8, pp. 831-832.

Davenport, A. G., 1961, “The Application of Statistical Concepts to the Wind Loading of Structures”, *Institution of Civil Engineers Proceedings,* Vol. 19, pp. 449-472.

Den Hartog, J.P., 1956*, Mechanical Vibrations*, 4th edition, McGraw-Hill, New York.

DIN-1056, 1984, “Solid Construction, Free Standing Stacks; Calculation, and Design”, *Deutsches Institut fur Normung*, Germany.

Erdik. M., and E. Uckan, 1989, “Ambient Vibration Survey of the Bogazici Suspension Bridge”, Report No: 89-5, Department of Earthquake Engineering Kandilli Observatory and Earthquake Research Institute, Bogazici University, Istanbul.

Ernst, H.J., 1965, “Der E-Modul von Seilen unter Berücksichtigung des Durchhängens”, *Bauingenieur*, Vol. 40, pp. 52-55.

Fleming, J. F., 1979, ‘‘Nonlinear Static Analysis of Cable-Stayed Bridge Structures’’, *Computers and Structures,* Vol. 10, No. 4, pp. 621-635, August.

Fleming J.F., and E.A. Egeseli, 1980, “Dynamic Behaviour of a Cable-Stayed Bridge”, *Earthquake Engineering and Structural Dynamics*, Vol. 8, pp. 1-16.

Freeman, F. and Partners, 1968, *Bosporus Bridge Calculations*, Westminster, London.

General Command of Mapping, 2009, *Izmit Bay 1:25000 Topographical Maps*, Ankara, Turkey.

Gimsing, N. J., 1998, *Cable Supported Bridges: Concept and Design.* John Wiley & Sons Ltd., New York.

Hansen. H, 1976, “The Fate of Flat Plate Aerodynamics in the World of Bridge Decks”, *The Theodorsen Colloquium*, Oslo, Norway.

Huang, M., and D. Thambiratnam, N. Perera, 2005, “Vibration Characteristics of Shallow Suspension Bridge with Pre-Tensioned Cables”, *Engineering Structures*, Vol. 27, pp. 1220-1233.

Hurty W. and M. Rubenstein, 1969, *Dynamics of Structures*, Prentice Hall of India, New Delhi.

Ito, M., 1991, “Cable-Stayed Bridges in Japan”, *Cable-Stayed Bridges: Recent Developments and their Future*, Elsevier Science Publishers, New York.

Kanok-Nukulchai, W., and G. Hong, 1993, ‘‘Nonlinear Modelling of Cable-Stayed Bridges’’, *Journal of Constructional. Steel Research*, Vol. 26, No. 2, pp. 249-266.

Karoumi R., 1999, *Response of Cable-Stayed and Suspension Bridges to Moving Vehicles Analysis Methods and Practical Modeling Techniques*, Ph.D. Dissertation, Royal Institute of Technology Department of Structural Engineering.

Kosar U., 2003, *System Identification of Bogazici Suspension Bridge*, M.Sc. Thesis, Department of Earthquake Engineering, Bogazici University, Istanbul, Turkey.

Krishna, P. and S. Arya, and T.P. Agrawal, 1985, ‘‘Effect of Cable Stiffness on Cable-Stayed Bridges’’, *Journal of Structural Engineering*, ASCE, Vol. 111, No. 9, pp. 2008-2020.

Larose, G. and F. Livesey, 1997, “Performance of Streamlined Bridge Decks in Relation to the Aerodynamics of a Flat Plate”, *Journal of Wind Engineering and Industrial Aerodynamics*, Vol. 69-71, pp. 851-860.

Lazar, B. E., M. Troitsky, and M.C. McDouglass, 1972, ‘‘Load Balancing Analysis of Cable-Stayed Bridges’’, *Journal of the Structural Division,* ASCE*,* Vol. 98, No. 8, pp. 1725-1740.

Leonhardt, F., 1987, “Cable Stayed Bridges with Prestressed Concrete”, *PCI Journal*, Vol. 31, pp. 52-80.

Leonhardt F. and Zellner W., 1991, *Past, Present and Future of Cable-Stayed Bridges, Cable Stayed Bridges: Recent Developments and Their Future*, Elsevier Science Publishers, New York.

Liu, W.K., 1981, *Development of Finite Element Procedures for Fluid-Structure Interaction*, Ph.D. Dissertation, California Institute of Technology.

Lutomirska, M., 2009, *Live Load Models for Long Span Bridges*, Ph.D. Dissertation, University of Nebraska**.**

Menon, D. and S. Rao, 1996, “Estimation of Along-Wind Moments in RC Chimneys”, *Engineering Structures,* Vol. 19, No. 1, pp. 71-78.

Midas Civil Analysis Manual, 2008, MIDAS IT Co., Ltd., USA.

Morgenthal,G., 1999, *Cable-Stayed Bridges - Earthquake Response and Passive Control*, MSc Dissertation, Imperial College of Science, Technology and Medicine Civil Engineering Department, UK.

NBCC, 1980, "Supplement to the National Building Code of Canada: Part 4", *National Research Council of Canada,* Ottawa.

Nakai, H., and T. Kitada, R. Ohminami, and T. Nishimura, 1985, ''Elastoplastic and Finite Displacement Analysis of Cable-Stayed Bridges'', *Memoirs of the Faculty of Engineering, Osaka University*, Vol. 26, pp. 251–271 (in English).

Nazmy, A. S., and A.M. Abdel-Ghaffar, 1990a, ''Three-Dimensional Nonlinear Static Analysis of Cable-Stayed Bridges'', *Computers and Structures,* Vol. 34, No. 2, pp. 257–271.

Nazmy, A. S., and Abdel-Ghaffar, A. M., 1990b, ''Nonlinear Earthquake Response Analysis of Long-Span Cable-Stayed Bridges: Applications'', *Earthquake Engineering and Strucural Dynamics,*Vol. 19, No. 1, pp. 63-76.

Ozdemir H., 1979, "A Finite Element Approach for Cable Problem", *International Journal of Solids and Structures*, Vol. 15, pp. 427-437.

PEER Strong Motion Database, 2005, *The Regents of the University of California*, http://peer.berkeley.edu/smcat/search.html

Pinfold, G. M., 1984, *Reinforced Concrete Chimneys and Towers*, Viewpoint Publication, London.

Podolny, W., and J.F. Fleming, 1972, ''History Development of Cable Stayed Bridges'', *Journal of the Structural Division*, ASCE, Vol. 98, No. 9, pp. 2079–2095.

Poser, F. and S. L. Wood., 2002, "Bending Fatigue of Stay Cables"*, Les 60 ans du professeur Manfred A. Hirt, École Polytechnique Fédérale de Lausanne*, Suisse. 59-68.

PTI Publication, 2001, *Recommendations for Stay-Cable Design, Testing and Installation, Post-Tensioning Institute*, Fourth Edition, March.

Ren, W.X., 1997, ‘‘Nonlinear Static and Seismic Behavior of Long Span Cable-Stayed Bridges’’, Res. Rep. No. 2, Department of Civil Engineering, *Nagoya Institute of Technology*, Nagoya, Japan.

Ren, W.X., 1999, “Ultimate Behavior of Long Span Cable-Stayed Bridges”, *Journal of Bridge Engineering*, ASCE, Vol. 4, No.1, pp. 30-37.

Ren, W.X. and Obata, M., 1999, “Elastic-Plastic Seismic Behavior of Long Span Cable Stayed Bridges”, *Journal of Bridge Engineering*, ASCE, Vol. 4, No. 3, pp. 194-203.

Ren W., and X. Peng and Y. Lin, 2005, “Experimental and Analytical Studies on Dynamic Characteristics of a Large Span Cable-Stayed Bridge”, *Engineering Structures*, Vol. 27, pp. 535–548.

Riks, E., 1979, ‘‘An Incremental Approach to the Solution of Snapping and Buckling Problems’’, *International Journal of Solids and Structures*, Vol. 15, pp. 529-551.

Roebling S.W., C.R. Farrar., M.B. Prime and D.W. Shevitz, 1996, *Damage Identification and Health Monitoring of Structural and Mechanical Systems from Changes in their Vibration Characteristics*, Research Report LA-13070-MS, ESA-EA, Los Alamos National Laboratory, New Mexico, USA, May.

SAP 2000 Advanced V.11, 2007, *Structural Analysis Program*, Computers & Structures Inc., University of California, Berkeley, USA.

Scanlan, R., 1988, “On Flutter and Buffeting Mechanisms in Long-Span Bridges”, *Journal of Probabilistic Engineering Mechanics*, Vol. 3, No. 1, pp. 22-27.

Selberg, A. and E. Hjorth-Hansen, 1976, “The Fate of Flat Plate Aerodynamics in the World of Bridge Decks”, *Proceedings of The Theodorsen Colloquium*, Oslo, Norway.

Seif, S. P., and W.H. Dilger, 1990, ‘‘Nonlinear Analysis and Collapse Load of P/C Cable-Stayed Bridges’’, *Journal of Structural Engineering*, ASCE, Vol. 116, No. 3, pp. 829-849.

Shu, H.S. and Y.C. Yang, 2001, "Stability Analysis of Box-Girder Cable-Stayed Bridges", *Journal of Bridge Engineering*, ASCE, Vol. 6, No. 1, pp. 63-68.

Smith, M., 2009, "Critical Analysis of the First Bosporus Bridge", *Proceedings of Bridge Engineering2 Conference2009*, University of Bath, UK.

Son, J., 2008, *Performance of Cable Supported Bridge Decks Subjected to Blast Loads*, Ph.D. Dissertation, University of California, Berkeley.

Tang, M.C., 1971, "Analysis of Cable-Stayed Girder Bridges", *Journal of the Structural Division*, ASCE, Vol. 5, pp. 1481-1496

Tang, M. C., 1976, ''Buckling of Cable-Stayed Girder Bridges'', *Journal of the Structural Division,* ASCE, Vol. 102, No. 9, pp. 1675-1684.

Tang, M.C., 1991, *Cable-Stayed Bridges in North America, Cable-Stayed Bridges: Recent Developments and Their Future*, Elsevier Science Publishers, New York.

Tezcan, S.S., and M.Ipek, J. Petrovski, T. Paskalov and T. Durgunoglu, 1974, *Ambient and Forced Vibration Survey of Istanbul Bogazici Bridge,* Department of Civil Engineering, Bogazici University, Bebek, Istanbul, July.

Turkish Navy Office of Navigation, Hydrography and Oceanography, 2009, *Izmit Bay Hydrographic Map*, Istanbul, Turkey.

Troitsky, M.S., 1988, *Cable-Stayed Bridges*, BSP Professional Books, Boston.

Vejrum, T., 2008, *Danish Engineers behind the World's largest Cable Stayed Bridges: Sutong and Stonecutters Bridge*- COWI A/S, Oslo, Norway.

Virola, J., 2002, "Los Puentes Colgantes de Tramo Ma´s Largo Del Milenio Pasado y Del Presente", *Boletin Tecnico IMME*, Vol. 40, No. 2, pp. 58–68.

Virola, J., 2009, "Long-Span Cable-Supported Bridges: General Review", *The IES Journal Part A: Civil & Structural Engineering*, Vol. 2, No. 4, pp. 304-308.

Wang, W., G. Chen and B. Hartnagel, 2007, "A Real-Time Condition Assessment of the Bill Emerson Cable-Stayed Bridge Using Artificial Neural Networks", *Proceedings of SPIE*, Vol. 6529, April.

Washizu, K., 1982, *Variational Methods in Elasticity and Plasticity*, 3rd Ed., Pergamon, U.K.

Xiao. C, and J.Cheng, 2004, "Advanced Aerostatic Stability Analysis of Suspension Bridges", *Wind and Structures*, Vol.7, No.1, pp.55–70.

Xu., Y.L., and J.M. Ko, Z. Yu, 1997, "Modal Analysis of Tower-Cable System of Tsing-Ma Long Suspension Bridge", *Engineering Structures,* Vol. 19, No. 10, pp. 857-867.

Zhang, X., and B. Sun, 2004a, "Aerodynamic Stability of Cable-Stayed-Suspension Hybrid Bridges", *Journal of Zhejiang University,* Vol. 6A, No. 8, pp. 869-874.

Zhang, X. and B. Sun, 2004b, "Parametric Study on the Aerodynamic Stability of a Long-Span Suspension Bridge", *Journal of Wind Engineering and Industrial Aerodynamics*, Vol. 92, pp. 431-439.